University of Cape Town

Department of Astronomy

Ultra-Diffuse Galaxy Candidates in Stripe 82 Clusters

A dissertation presented in partial fulfillment of the requirements for the degree of MS.c as part of the National Astrophysics and Space Science Programme

Author:

Nazir Ahmed Adam Makda

Supervisors:

Dr Rosalind Skelton

Dr Sarah Blyth

25 September 2019

Plagiarism declaration

I, Nazir Ahmed Adam Makda, know the meaning of plagiarism and declare that all of the work in the dissertation, save for that which is properly acknowledged, is my own.

Abstract

The evolution of galaxies in the cluster environment is a complex process, with many outstanding questions. A wide range of galaxy morphologies, colours, sizes and luminosities are found in clusters, the least studied of which are the faint galaxy populations. Studying the faint end of the galaxy luminosity distribution may provide a valuable insight into the evolution of galaxies in cluster environments. The largest of these faint galaxies are classified as Ultra-Diffuse galaxies (UDGs). UDGs are low surface brightness galaxies with a very low stellar mass component, however they have sizes comparable to the Milky Way. These galaxies are hard to detect and classify as they are very faint. To survive in the cluster environments, where they have been observed, these galaxies must contain significant amounts of dark matter as the strong tidal fields would normally tear diffuse low-mass galaxies apart. The high abundance of UDGs in clusters has only recently been recognized, therefore identifying and measuring their properties is key to understanding how they are formed and continue to exist.

In this thesis, I search for low surface brightness galaxies, spanning from typical dwarf galaxies to UDGs, in 16 low redshift (z<0.15) clusters in the deep IAC Stripe 82 Legacy project data by selecting cluster members based on color-magnitude cuts and modelling their two-dimensional light distributions to obtain sizes and surface brightness values. This is the largest sample of clusters in which anyone has searched for UDGs before in a uniform way. A total of 941 galaxies are identified in the 16 Stripe 82 clusters with surface brightness $\mu_e(g) \gtrsim 24\,\mathrm{mag/arcsec^2}$ and effective radius $r_e \gtrsim 1.5$ kpc; an average of 59 per cluster. Of these, 165 are classified as UDGs following van Dokkum et al. (2015). The larger and fainter galaxies are easily distinguished above non-cluster background distributions. I find that the surface brightness profiles are typically exponential, $n \sim 1$, implying disk morphologies and the axis ratios are evenly spread, $< b/a >= 0.52$. The number of faint galaxies in clusters follows a power-law with respect to the cluster halo mass, $N \propto M^{1.05\pm0.45}$, determined through bootstrap resampling. This shows that the number of UDG candidates increases as the cluster halo mass increases.

Contents

Chapter 1

Introduction

Galaxies are complex systems, comprising of gravitationally bound gas, stars, dust and dark matter (DM). The fraction of each of these components are different in each galaxy. Galaxies all have different formation histories as they form and evolve in different environments. This results in a range of different morphologies. This thesis identifies and analyzes the properties of large, low surface brightness galaxies in clusters. In the following sections I discuss the properties of the different types of galaxies, their formation and evolution. I also cover the effects of different environments on the morphology of galaxies.

1.1 Galaxy Morphology

There are a few galaxies which can be seen with the naked eye, the Large and Small Magellanic Clouds, Andromeda, Triangulum and of course our Milky Way. These galaxies all lie within the local group, less than 10 million light years across. The first catalogue of extended sources, Messier (1781), was published at the end of the 18^{th} century by Charles Messier and presents the first 103 catalogued objects. Messier identified these sources as either nebulae or star clusters, however, since that time they have been observed and classified as open clusters, globular clusters, galaxies, nebulae, planetary nebulae and supernova remnants. At the time of observing and cataloguing these sources they were believed to be in the Milky Way. Many of these sources were only determined to be external to the Milky Way at the beginning of the 20^{th} century. The "Great Debate" occurred in 1920, which attempted to determine whether the Milky Way was the extent of the universe or whether "spiral nebulae" were extragalactic. Distance measurements of M31 (Opik, 1922) and subsequently more spiral galaxies (Hubble, 1926) proved them to be beyond the Milky Way, and thus settled the debate on galaxies outside of the Milky Way. Today, it is estimated that there are over 2×10^{12} galaxies in the universe up to a diameter of 26.15 billion years (Conselice et al., 2016).

1.1.1 Classification

Hubble (1926) recognised common visual features between the different galaxies and classified them based on visual appearance. The Hubble tuning fork classification scheme was born. Figure 1.1 (Hubble Classification, 2016) displays the Hubble tuning fork diagram. Elliptical galaxies are observed to be smooth, featureless ellipsoids and are classified by the degree of elongation. Spiral galaxies appear as flat disks, with spiral arms extending from a central bulge. Spirals are separated into two main groups, those with a bar and those without. They are then classified based on the number, compactness and clarity of the spiral arms. Lenticular galaxies can be considered as featureless disk galaxies, or highly elongated elliptical galaxies with a prominent bulge. In the classification scheme they occupy the region between elliptical and spiral galaxies. Irregular galaxies have no clear common structure. They have unique sets of characteristics which makes them hard to classify.

Several classifications followed the Hubble scheme, with the most notable being that of de Vaucouleurs (1959) which expanded on the Hubble (1926) scheme. The structure within spiral galaxies (bars, rings and arms) was examined more carefully and extended the well-established Hubble tuning fork. The Galaxy Zoo project (Lintott et al., 2008) classified the morphologies of galaxies extracted from the Sloan Digital Sky Survey (SDSS) (York et al., 2000). A total of over 668,000 sources with spectra were classified, 190,000 were categorized as spiral, while 62,000 were catalogued as elliptical.

Elliptical galaxies are also sometimes referred to as 'early type' galaxies while spirals are called 'late-type' galaxies. The formation of galaxies was not understood and Hubble (1926) prematurely named them anticipating ellipticals were newly-formed galaxies which would later develop spiral arms, and spirals were more evolved galaxies. More recently, we have observed that spiral galaxies typically have younger stellar populations than ellipticals, which are the older population of galaxies but may form from the merger of disk galaxies or disk instabilities.

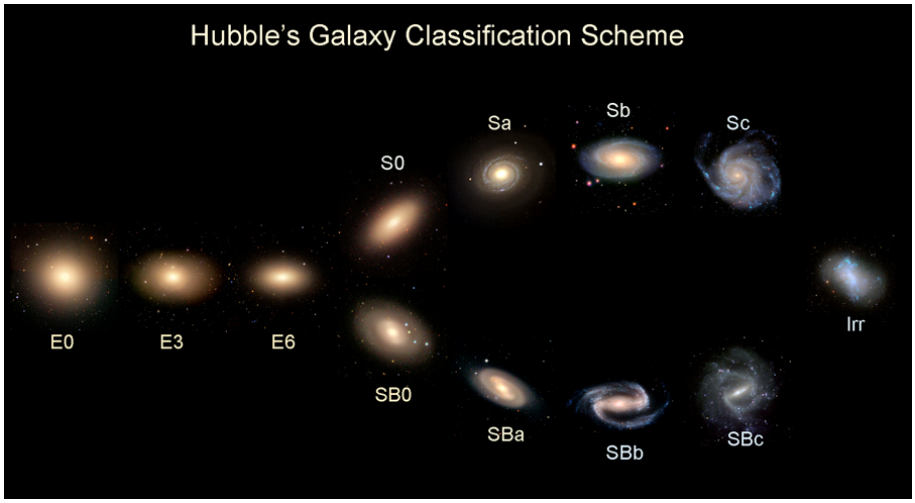

Figure 1.1: The Hubble tuning fork. Elliptical galaxies are shown on the left, from spherical, E0, to spheriodal, E6. Lenticular galaxies are denoted with S0 and SB0, where the B indicates the central bulge is bar shaped. Spiral galaxies are also split into two main categories, spirals and barred spirals. From left to right the spiral arms become more numerous and less tightly wound. The right-most galaxy is classified as irregular, the shape is unique. (Hubble Classification, 2016)

Generally elliptical galaxies have an old stellar population with a very low star formation rate. They also have many globular clusters in their haloes. Globular clusters are typically populations of old stars. They are spherical in shape and gravitationally bound. Supermassive black holes (SMBH) exist in the centres of elliptical galaxies (e.g. Ferrarese & Merritt 2000, Tremaine et al. 2002). DM is non-baryonic matter that is assumed to only interact gravitationally with other matter (e.g. Ratra & Vogeley 2008). Ellipticals are generally found close to the centres of galaxy clusters, where their high DM content preserves the galaxies' structure in the strong tidal fields of the cluster environment (Dressler, 1980).

The DM fractions for elliptical galaxies have been estimated to be between 0.12 (Cappellari et al. 2013 and Barnabè et al. 2011) and 0.6 (Tortora et al. 2009) based on different techniques. Tortora et al. (2009) investigated the central mass-to-light ratios and DM fractions of local elliptical galaxies (Prugniel & Simien, 1996) using population synthesis models. Barnabè et al. (2011) identified 16 early-type lens galaxies utilizing the SLACS survey (Bolton et al., 2006). Constraints determined from the gravitational lensing and stellar kinematics were used to construct dynamical models. Cappellari et al. (2013) used the ATLAS project (Cappellari et al., 2011), selecting 260 early type galaxies from the 2MASS survey (Skrutskie et al., 2006) and determined their properties using stellar dynamical modelling.

Spiral galaxies generally consist of three main components: a central bulge, a disk with spiral arms extending from the bulge, a halo of old stars surround the bulge and disk. Spiral galaxies are most common in the field. In the cluster environment spiral galaxies are generally found in the outer regions with larger spirals found closer to the cluster centre. The main feature of these galaxies is the spiral arms which exist in the disk. The spiral arms are modelled using the density-wave theory (Shu, 1970a,b; Shu et al., 1971; Toomre, 1977) and form as a result of material in the disk traveling through density waves. The material in this region of the disk is compressed, collapse of the gas is initiated and star formation follows. Therefore, spiral arms usually contain a young star population compared to the older star population in the central bulge. Figure 1.1 displays the morphology of spiral galaxies and their classifications. There are two types of spiral galaxies, namely barred and non-barred spirals, which are identified in the image by the SB and S prefixes respectively. In barred spirals the arms usually emerge from the ends of the central bar, winding outward. Figure 1.1 gives an outline of spiral galaxy morphologies, however spirals have a much wider range of possible structures.

Spiral galaxies have been studied to gain an understanding of the internal behaviour of these galaxies and to identify the effects of DM on them. The rotation curves determined from spiral galaxy observations reveal that the orbital velocities remain high as radius increases, (e.g. Rubin et al. 1978, Rubin et al. 1980, etc). This is contrary to the expected curve, which was believed to decrease with radius as the amount of observed matter stops increasing toward the edge of the galaxy. This indicates a large amount of DM in these galaxies, and the increase in the DM fraction as radius increases. Persic et al. (1996) analysed the rotation curves of $\sim$ 1100 spiral galaxies using the 'universal rotation curve' proposed by Rubin et al. (1985). Yegorova & Salucci (2007) found and used a radial Tully-Fisher (Tully & Fisher, 1977) relation to examine the rotation curves of $\sim$ 960 spirals. Both techniques determined that the DM in spiral galaxies follows a scaling relation:

$$\frac{M_{DM}}{M_L} \propto L_B^{-0.7} \quad , \tag{1.1}$$

where M_{DM} is the DM mass; M_L is the mass of luminous matter as observed in the B-band; L_B is the B-band luminosity. Therefore fainter spiral galaxies are more likely to have higher fractions of DM.

Irregular galaxies are observed to be smaller and less luminous than spiral and elliptical galaxies. The structure and morphology of irregular galaxies are quite varied and many subcategories were created to classify the wide spectrum of observed features (Gallagher & Hunter, 1984). These include dwarf galaxies with some structure resembling the spiral arms visible in spiral galaxies. The variation in structure may have several causes, including: interactions with other galaxies; extended interstellar matter and recent star formation (Gallagher & Hunter, 1984). Irregulars account for many of the galaxies which do not fit into the elliptical and spiral classification, therefore, they are found to be very abundant and possibly accounting for between 30% to 50% of all galaxies (e.g. Kraan-Korteweg & Tammann 1979, Tammann 1980). DM in these irregular galaxies is found to be abundant in the larger irregulars and comparatively deficient in the dwarf irregulars (Gallagher et al., 1984). Patterson & Thuan (1996) reach a similar conclusion for dwarf irregulars. The central regions of dwarf irregulars is dominated by the luminous matter and the DM fraction only becomes significant at large radii.

1.1.2 Dwarf and Low Surface Brightness Galaxies

The Hubble classification scheme does not include dwarf and low surface brightness (LSB) galaxies. Typically these galaxies are harder to observe as they tend to be fainter than ellipticals and spirals. Dwarf galaxies are smaller and less luminous than ellipticals and spirals, and may be satellites to more massive galaxies. LSB galaxies have a range of sizes and are typically distinguished by their low surface brightness.

Dwarf galaxies are observed to have a range of different morphologies and sub-classifications: dwarf elliptical, dwarf spheroidal, dwarf spiral, blue compact, ultra compact and irregular. The masses and sizes of the dwarf ellipticals, dwarf spheroidals and dwarf spirals are significantly lower than their Hubble classified counterparts. Generally galaxies similar to the size of the Milky Way have approximately hundreds of billions of stars, whereas dwarf galaxies contain tens of billions of stars. Dwarf galaxies in the Local Group have a range of central surface brightnesses, $\mu_0(V) = 20\,\mathrm{mag/arcsec^2}$ - $30\,\mathrm{mag/arcsec^2}$ (McConnachie, 2012). The dynamical mass of the Local Group dwarfs are reported to range from $M_{dyn} = 2.3 \times 10^5 M_\odot - 5.4 \times 10^8 M_\odot$ (McConnachie, 2012).

LSB galaxies is a classification identifying all galaxies which appear to be diffuse. There are no strict guidelines for a galaxy to be LSB, however a B-band central surface brightness of $\mu_0(B) > 23\,\mathrm{mag/arcsec^2}$ can be considered the maximum brightness limit (Impey & Bothun, 1997). These LSB galaxies have a diverse range of morphologies, from giant gas-rich disks to dwarf spheroidals. Several surveys over the past 70 years contain significant LSB galaxy observations, both inside the cluster environment and in the field (e.g. van den Bergh 1959, Binggeli et al. 1985, O'Neil et al. 1997a). The total masses of LSB galaxies range from $M_T = 2.8 \times 10^{10} M_\odot - 6.9 \times 10^{11} M_\odot$ (van der Hulst et al., 1993).

1.2 Galaxy Formation and Evolution

The Big Bang theory of the formation of the observable universe is the most widely accepted cosmological model currently. The theory describes the processes which took place from the hot and dense early universe to the current large-scale structure. The Λ cold dark matter (ΛCDM) model is the simplest model which describes the Big Bang and content of the universe (Peebles & Ratra, 2003); it is commonly

referred to as the standard cosmological model. The ΛCDM model is built on the cosmological principle that the universe is both homogeneous and isotropic. The ΛCDM universe predominantly consists of dark energy, responsible for the accelerating expansion of the universe and accounted for by cosmological constant Λ in the model. Cold dark matter (CDM), baryonic matter, and radiation make up the remaining components of the universe. CDM is non-baryonic and interaction with other matter is assumed to only occur through gravitation (e.g. Ratra & Vogeley 2008).

In the ΛCDM model, the universe began as an extremely hot and dense singularity that underwent extreme exponential expansion during a phase known as inflation (Liddle & Lyth, 2000). Thereafter, the universe followed the more gradual Hubble expansion. The singularity expanded in the form of a plasma, consisting of photons, protons and electrons. The plasma cooled as it expanded and the first atoms formed. Photons decoupled from matter and were emitted into the universe, observed today as the Cosmic Microwave Background (CMB). The photons were emitted at very short wavelengths and high temperatures (>10 000 K) approximately 372 000 years after the Big Bang (Spergel et al., 2003). The emission of photons in the universe ceased in an epoch known as the 'Dark Ages'. DM began to gravitationally collapse and form halos. Baryonic matter collapsed in these halos and initiated the start of the first radiation sources and star formation. The growth of structures continued under gravitation, forming galaxies and larger structures which trace DM overdensities. The largest gravitationally bound structures in the universe are galaxy clusters (Ratra & Vogeley, 2008). Figure 1.2 displays the timeline of the universe, from singularity approximately 13.7 billion years ago to the present day.

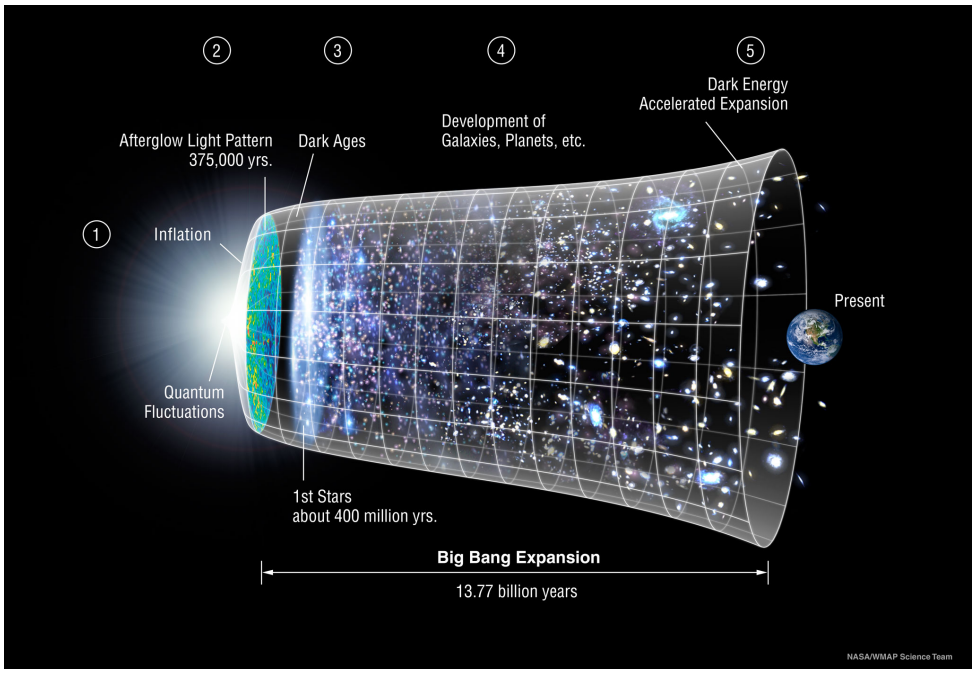

Figure 1.2: Timeline of the universe, from singularity through expansion to present day. The formation of galaxies occurred soon after the first stars were formed (Image Credit: Adaptation of the original NASA WMAP Science Team image, NASA/WMAP 2012).

Galaxy formation follows a hierarchical clustering, 'Bottom-Up' theory (Peebles, 1980). This theory follows a process whereby smaller clumps of matter merge together to form larger clumps and so on. This merging of smaller clumps to form larger clumps is gravitationally driven, and results in the formation of galaxies. In the same manner many galaxies would then form a galaxy cluster. At each stage in the hierarchical clustering larger clumps of matter form from the mergers of smaller clumps and subsequently collapse. The substructure of these smaller clumps is lost due to relaxation effects and result in bound masses with a self-similar distribution (Press & Schechter, 1974). These clumps draw together in DM halo potential wells, where residual gas cools, fragments and forms the luminous matter in galaxies (White & Rees, 1978). Therefore galaxies lie in an extensive DM halo and have a dense luminous central core. Galaxy survival in the cluster environment relies on substantial amounts of concentrated mass to maintain the galaxies' structure and prevent stripping of large amounts of material.

1.2.1 Cluster Environment

The cluster environment is a very turbulent region where large numbers of galaxies orbit the cluster centre in very close proximity to each other. The virial mass of DM halos can range from $M_{200} \sim 10^{13} M_{\odot}$ in groups to $M_{200} \sim 10^{16} M_{\odot}$ in large clusters (Popesso et al., 2005). Simulations of galaxies (Moore et al., 1996) in clusters reveal that galaxies within a cluster are primarily affected by mutual gravitational interactions with neighbouring galaxies. Moore et al. (1996) conclude that the harassment by other galaxies in the cluster may potentially change the gas distribution, orbital distribution of stars and the galaxies' morphology. In the simulations spiral galaxies merge to form bright ellipticals. Low luminosity spiral galaxies undergo harassment in the cluster and become dwarf elliptical galaxies. This shows the effect neighbouring galaxies in clusters may have on diffuse, extended sources. Spiral galaxies on radial trajectories were found to become gas-poor faster than spirals on circular orbits (Dressler, 1986). This suggest that spiral galaxies further from the cluster center are less affected by the cluster's tidal pressures. The simulations by Moore et al. (1998) show that the global cluster potential and interaction with neighbouring galaxies cause small disk galaxies to evolve into spheroidal galaxies commonly found in nearby clusters. The gas in cluster galaxies is also exposed to several other environmental effects, including strangulation (Berrier et al., 2009), starvation (Haines et al., 2013) and ram pressure stripping (Tonnesen et al., 2007).

1.3 Ultra-diffuse Galaxies

Ultra-diffuse Galaxies (UDGs) fall into a class which distinguishes the largest and faintest galaxies. Van Dokkum et al. (2015) conceived the term Ultra-diffuse Galaxy after discovering 47 extremely low surface brightness galaxies in the Coma cluster. These galaxies were found using the Dragonfly Telephoto Array (Abraham & van Dokkum, 2014) while searching for extended ultra low surface brightness structures in Coma. UDGs are defined by van Dokkum et al. (2015) to have a central surface brightness of $\mu_0(g) \gtrsim 24\,\mathrm{mag/arcsec^2}$ and an effective radius of $r_e \gtrsim 1.5\,\mathrm{kpc}$. Previously, dwarf galaxies with similar properties to UDGs have been observed in various environments (Cohen et al., 2018; Danieli & van Dokkum, 2019). The UDG classification distinguishes the largest and faintest of these galaxies from other galaxy populations. UDGs may be considered to be an extreme subset of low surface brightness galaxies or dwarf galaxies. Following the discovery van Dokkum et al. (2015), other authors searched for low surface brightness galaxies in nearby clusters. Koda et al. 2015 found more than 800 UDG-like galaxies in Coma with over 300 satisfying the van Dokkum et al. (2015) criteria, using deeper data from the Subaru telescope (Okabe et al., 2014). The Subaru data have a limiting image depth of $\sim 30.2\,\mathrm{mag/arcsec^2}$ (1σ) in a $10''$ compared to Dragonfly's $\sim 28.6\,\mathrm{mag/arcsec^2}$ (1σ). Therefore Koda et al. 2015 data are ~ 1 mag deeper than van Dokkum et al. (2015) and as expected more faint sources are found in their images. The unexpected discovery of an abundance of UDGs in Coma has ignited research into these large low surface brightness galaxies and their environments (e.g van der Burg et al. 2017, Trujillo et al. 2017a, Bellazzini et al. 2017).

1.3.1 Ultra-diffuse Galaxy Properties

Since the initial classification and discovery of a large number of UDGs in the Coma cluster, there have been numerous projects attempting to find and determine the characteristics of these galaxies (e.g. Beasley et al. 2016; van der Burg et al. 2016; Ruiz-Lara et al. 2018; Sifón et al. 2018). The following sections will discuss the attributes of UDGs.

One of the criteria set by van Dokkum et al. (2015) requires galaxies to have a central surface brightness in the g-band greater than $24\,\mathrm{mag/arcsec^2}$ to be considered UDGs. The second criterion is that the effective radius must be larger than 1.5 kpc. Figure 1.3, taken from van Dokkum et al. (2015), compares UDGs to typically observed galaxies in the radius-surface brightness plane. From the plot we can see that the criteria set by van Dokkum et al. (2015) distinguishes the largest and faintest galaxies from the rest of the galaxy population. The sizes of these UDGs are comparable to typical spiral galaxies, however the surface brightnesses of the Coma UDGs are similar to the fainter dwarf galaxies in the Virgo cluster. The extended visible stellar structure of these galaxies is not expected to survive in the harsh cluster environment. Their abundances in clusters may imply a high DM content in UDGs, which could be responsible for maintaining the stellar population within the galaxy (van der Burg et al., 2016).

The environments where UDGs have been discovered are very important as they may have impacted their formation and evolution (e.g. van der Burg et al. 2017; Román & Trujillo 2017a; Román & Trujillo 2017b). UDGs have been predominantly found in cluster and group environments, with a few identified

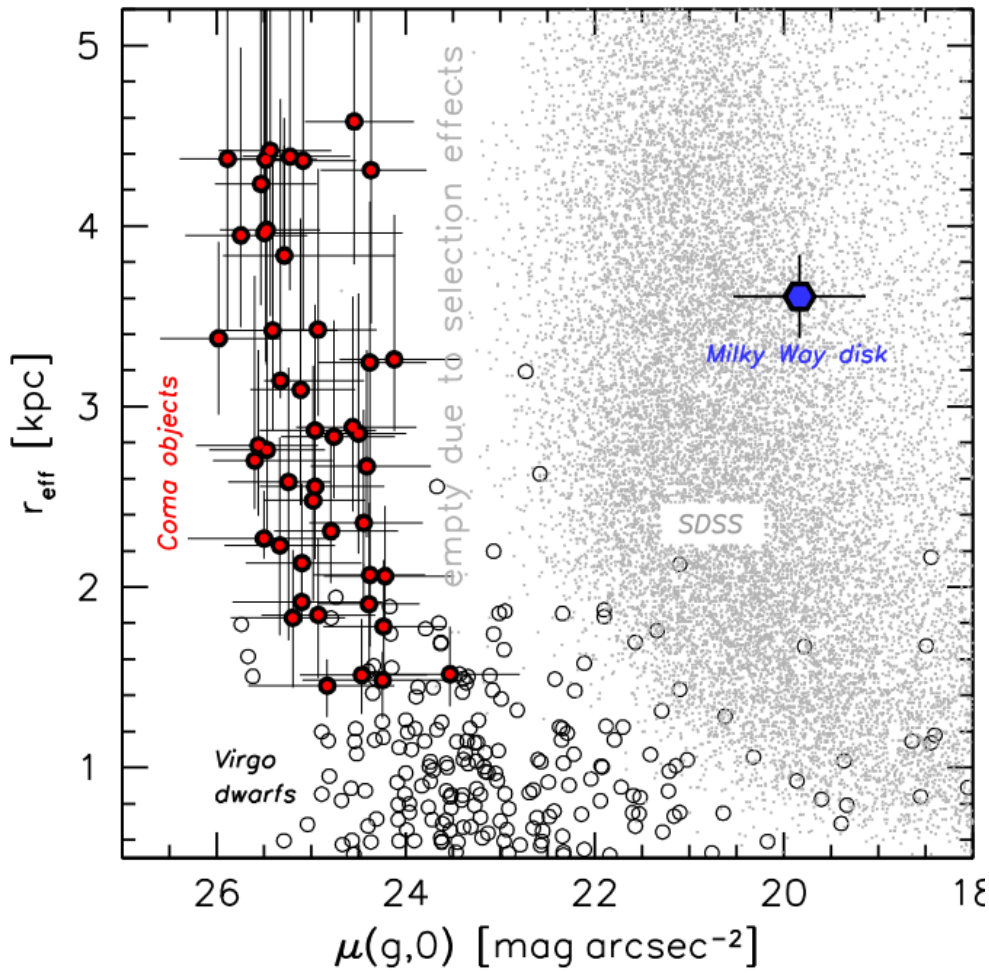

Figure 1.3: Effective radius vs. central surface brightness plot compares Coma UDGs, red points, to typical galaxies. The Milky Way disk is identified in blue, low redshift SDSS galaxies are the grey dots and dwarf galaxies in Virgo are identified by the hollow circles. Figure taken from van Dokkum et al. (2015).

in the field. Table 1.1 displays recent UDG surveys using data from different telescopes. The Coma cluster has been investigated by van Dokkum et al. (2015), Koda et al. (2015) and Yagi et al. (2016). This is perhaps the most well-studied UDG environment, utilizing both Dragonfly data (Abraham & van Dokkum, 2014) and Subaru archival data (Okabe et al., 2014). Van Dokkum et al. (2015) identify 47 UDGs in Coma, while Koda et al. (2015) and Yagi et al. (2016) find 332 and 278 UDGs respectively. The Subaru data is ~ 1 mag deeper than the Dragonfly data therefore the number of UDGs are significantly higher. Román & Trujillo (2017a) searched the Abell 168 cluster and its surrounding regions, identifying 80 UDGs. The abundances and spatial distributions of UDGs in 8 nearby clusters were investigated by van der Burg et al. (2016) and the number of UDGs per cluster ranges from 29 to 189. The higher redshift Abell 2744 cluster was investigated with deep HST data from the Hubble Frontier Fields (HFF) program (Lotz et al., 2017) by both Lee et al. (2017) and Janssens et al. (2017). They found 40 and 76 UDGs respectively. The large difference arises from using different UDG selection methods. Lee et al. (2017) also examined Abell S1063 where they identified 47 UDGs in the cluster. The studies on Abell 2744 and Abell S1063 only cover a small portion of the clusters as only the central cluster regions were imaged in the HFF program. These confirmed UDGs are reported in Table 1.1. The Fornax and Virgo clusters were investigated by Mihos et al. (2015), Muñoz et al. (2015) and Venhola et al. (2017), discovering 3, 9 and 9 UDGs in these regions respectively.

UDGs have been theorized to exist in low density environments (Di Cintio et al. 2017; Rong et al. 2017; Chan et al. 2018; Di Cintio et al. 2019). Di Cintio et al. (2017, 2019) use zoom-in simulations from the Numerical Investigation of a Hundred Astrophysical Objects (NIHAO) project (Wang et al., 2015) to model the formation of UDGs. The models predict UDGs are formed due to star formation outflows and therefore imply their existence in the field environment. The predictions made from the

Paper	Region	Telescope	UDGs	<b/a>	Sérsic, n
van Dokkum et al. (2015)	Coma	Dragonfly	47	0.70	1
Koda et al. (2015)	Coma	Subaru	332	0.69	0.99
Yagi et al. (2016)	Coma	Subaru	278	-	-
van der Burg et al. (2016)	Nearby clusters	CFHT	29 - 189	-	-
Román & Trujillo (2017a)	Abell 168 & surr.	Sloan Foundation	80	0.7	0.70
Román & Trujillo (2017b)	Nearby clusters	Sloan Foundation	6	0.70	0.87
Janssens et al. (2017)	Abell 2744	HST	76	-	-
Lee et al. (2017)	Abell 2744	HST	40	0.69	1.14
Lee et al. (2017)	Abell S1063	HST	47	0.67	0.94
Mihos et al. (2015)	Virgo	Burrell Schmidt	3	-	0.90
Muñoz et al. (2015)	Fornax	Blanco & VISTA	9	-	1.07
Venhola et al. (2017)	Fornax	VST	4;5*	0.38;0.69	0.81;0.80

Table 1.1: UDG surveys of different regions and using different telescopes. Also included are the number of UDGs, the average axis ratio and the Sérsic index. *Venhola et al. (2017) separate their UDGs by size, 4 UDGs have radius $r_e > 3.0$ kpc, a mean axis ratio $<b/a> \sim 0.38$ and Sérsic index $n \sim 0.81$.

models by Rong et al. (2017) agree with their subsequent search for UDGs in the Local Group and Local Volume, suggesting UDGs form in low density regions. We discuss the details of these simulations and UDG models further in Section 1.3.2 of this chapter.

Román & Trujillo (2017a) identify six UDGs in isolated galaxy groups and Martínez-Delgado et al. (2016) report the discovery of the UDG DGSAT 1 in a filament of the Pisces-Perseus supercluster. Two field UDGs were discovered by Bellazzini et al. (2017), one of which has an unusually high gas content, $M_{HI}/M_\star \sim 90$. The characteristics of low density UDGs are slightly different compared to cluster UDGs. Their colours are bluer, indicating a younger stellar population and possibly ongoing star formation. In contrast, the majority of UDGs discovered so far in the cluster environment have been found to be red and passively evolving. Bluer UDGs have also been found in clusters, however they are usually further from the cluster centre, in lower density regions than typical UDGs. Figure 1.4 (Koda et al., 2015) displays sources from the Coma cluster. The UDGs, in green, can be seen to follow the red sequence as we expect for typical cluster galaxies. However we do see a few UDGs with bluer colours, possibly the UDGs in the outer regions of the cluster with ongoing star formation.

The age of the stellar population in UDGs can be estimated with stellar population synthesis models (e.g. Conroy et al. 2009, Bruzual & Charlot 2003, Vazdekis et al. 2015). The colours determined by the models are compared to the observed UDG colours, as the spectral energy distributions are not currently available for these sources. The models with similar colours to the UDGs are used along with the other measurable properties to make the age estimates. The models are generally run using several estimated metallicities. Typically low-mass galaxies like these UDGs have low stellar metallicities (Kirby et al., 2013), therefore commonly used metallicities are well below solar metallicity values. The 47 UDGs found in Coma by van Dokkum et al. (2015) have an age of 7 Gyr given a metallicity of [Fe/H]=-1.4, or 4 Gyr with [Fe/H]=−0.8. The nearby galaxy clusters studied by van der Burg et al. (2016) were reported to have an age of 2 Gyr with a solar metallicity, [Fe/H]= 0.013, or 6 Gyr with [Fe/H]= –0.7. Consequently the UDGs in these clusters have expected stellar populations younger than most of the massive cluster galaxies in their respective systems. This may indicate UDGs have not always been a part of the cluster and may in fact have been accreted at a later time.

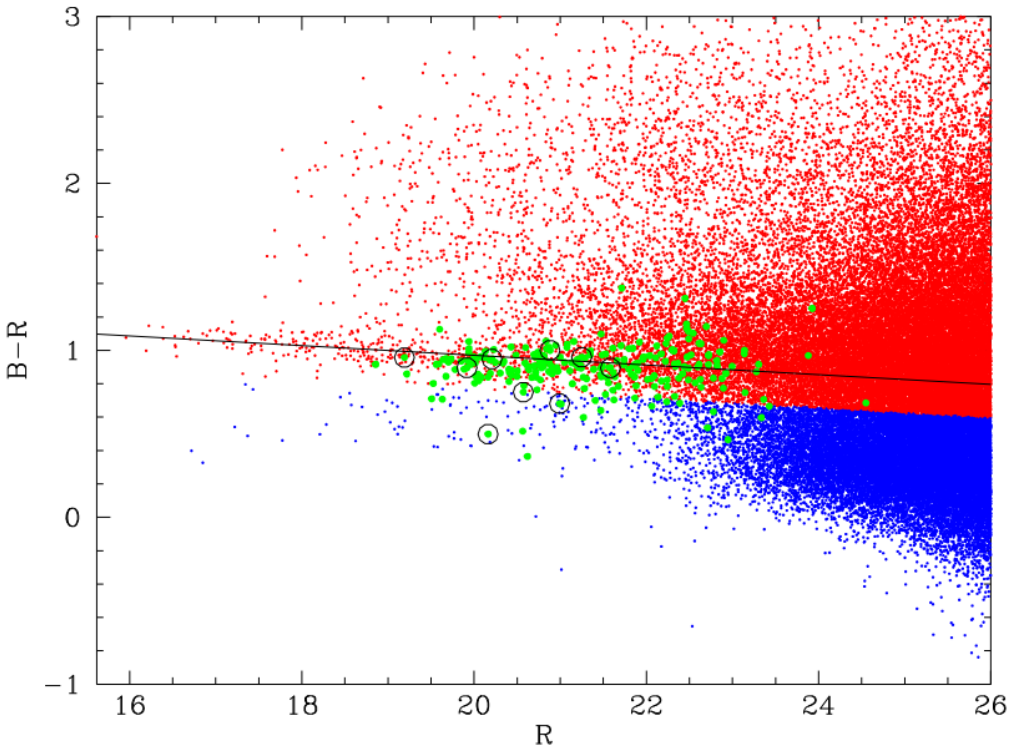

Figure 1.4: Colour-magnitude diagram, $B - R$ colour vs. R-band magnitude for sources identified in the Coma cluster. Red galaxies and blue galaxies are identified by their respective colours, both Coma members and background sources are included. The solid black line distinguishes the red sequence. The green points mark the colours of 232 UDGs in the Koda et al. (2015) Coma UDG catalogue and the circled UDGs are those also identified by van Dokkum et al. (2015). Figure taken from Koda et al. (2015).

The axis ratio describes the shape of the UDG; it compares the size of the semi-minor and semi-major axis. An axis ratio of 1 implies the galaxy is spherical, while a low number means the galaxy is more elongated. The average axis ratios found by different UDG surveys are shown in Table 1.1. The mean axis ratio of the 47 Coma UDGs in van Dokkum et al. (2015) was found to be 0.70 which is in agreement with the axis ratio of 0.69 found by Koda et al. (2015). An approximate axis ratio for the UDGs found in the Abell 168 region is 0.7 (Román & Trujillo, 2017a). In the Fornax cluster, Venhola et al. (2017) determined an axis ratio of 0.38 for large UDGs ($R_e > 3.0$ kpc) and 0.69 for small UDGs ($R_e < 3.0$ kpc). These results suggest UDGs have a spheroidal shape, however the larger UDGs in the Fornax cluster do appear to be more elongated than in other clusters.

The light profile of a galaxy can be described by the Sérsic index (Sérsic, 1963). Low indices, $n < 1.0$, are indicative of a shallow light profile with no bulge. Large indices, $n > 1.0$, indicate a steep light profile with a relatively brighter central region compared to the outer regions of the galaxy. The Sérsic index is described in greater detail in Section 2.2.4. Table 1.1 also displays the Sérsic indices for UDG surveys. Figure 1.5 displays a comparison of the Sérsic indices of Coma, Abell 168, AS1063 and A2744 and their respective scatter. Koda et al. (2015) report an average Sérsic index $n = 1.0$ for UDGs in the Coma cluster with a standard deviation of 0.34. This is consistent with an exponential light profile which is similar to the profiles of spiral galaxies and dwarf elliptical galaxies. The average Sérsic indices found in Abell 168 are approximately $n \sim 0.70$ with a standard deviation of 0.24 (Román & Trujillo, 2017a), which implies a much shallower light profile compared to the Coma UDGs. The surveys by (Venhola et al., 2017) and Mihos et al. (2015) report Sérsic indices of $n \sim 0.80$ and n $\sim n \sim 0.90$ for the Fornax and Virgo cluster UDGs respectively. The surveys by Lee et al. (2017) report average Sérsic indices of $n \sim 0.94$ and $n \sim 1.14$ for the UDGs in Abell S1063 and A2744 clusters respectively, with standard deviations of 0.62 and 0.64. In Figure 1.5 the scatter of the Sérsic Indices in AS1063 and A2744 UDGs can be seen to be larger than the scatter reported in Coma and Abell 168. However, the Sérsic indices and scatter in these surveys overlap and show that the determined indices of the UDG samples are quite consistent. The difference in light profiles observed in the UDGs of these surveys may be caused by different environments

or an evolution with redshift. All the surveys identified here used GALFIT to determine the Sérsic indices, except Román & Trujillo (2017a). IMFIT (Erwin, 2014) was used to model the Sérsic indices for UDGs in Abell 168. This may imply that the methods used in IMFIT produce models with shallower profiles than GALFIT. Interestingly, Venhola et al. (2017) measures identical Sérsic indices for their larger and smaller UDGs even though the axis ratios are significantly different.

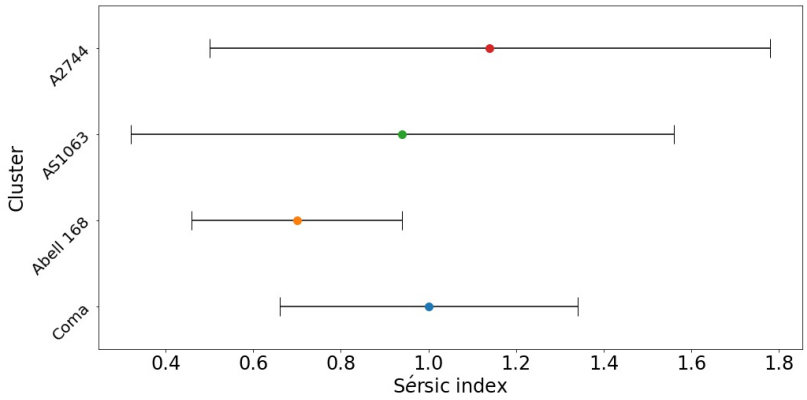

Figure 1.5: Comparison of Sérsic indices and their scatter in Coma, Abell 168, AS1063 and A2744. The y-axis identifies the clusters and the Sérsic index is on the x-axis. We can clearly see that the error bars in these clusters overlap and are quite consistent.

The stellar masses of UDGs can be calculated using stellar population synthesis models (e.g. Taylor et al. 2011, Bruzual & Charlot 2003, Bell et al. 2003) and measured mass-to-light ratio measurements. The observed colours of the UDGs are used to determine their mass-to-light ratios which are used with the models to estimate their masses. Van Dokkum et al. (2015) used the Taylor et al. (2011) method along with the measured UDG absolute magnitudes and colours to estimate the stellar mass. The resulting UDG masses range from $1 \times 10^7\,M_\odot$ - $3 \times 10^8\,M_\odot$. The absolute magnitudes and adopted mass-to-light ratio, $\mathrm{M/L}_R \sim 3$ were used by Koda et al. (2015) to determine stellar masses of Coma UDGs, which were found to range from $1 \times 10^7\,M_\odot$ - $5 \times 10^8\,M_\odot$, in agreement with van Dokkum et al. (2015). Van der Burg et al. (2016) calculated an average stellar mass of $\sim 10^8\,M_\odot$ using the Bruzual & Charlot (2003) model for UDGs in nearby clusters. Similar stellar masses were found for UDGs in the Abell 168 region, with a peak at approximately $10^8\,M_\odot$ (Román & Trujillo, 2017a). Simple stellar population models were used to estimate the stellar masses of UDGs in the Abell S1063 and Abell 2744 clusters, which ranged from$10^8\,M_\odot$ to $10^9\,M_\odot$. The stellar masses of these UDGs are in agreement, and also have masses similar to dwarf galaxies, $\sim 10^8\,M_\odot$. Figure 1.6 displays the mass distribution of UDGs compared to regular galaxies with measured spectroscopic redshifts in the Abell 168 region taken from Román & Trujillo (2017a). The UDG masses are clearly lower than the average mass for regular galaxies in the region. However, selection effects may have resulted in the apparent separation in the galaxy populations.

The UDGs discovered by van Dokkum et al. (2015) were all in the outer regions of Coma at a radius $r_e \gtrsim 300\,\mathrm{kpc}$. Clusters have very strong tidal fields. Galaxies require a minimum mass (m_{tot}) within radius (r_d) to resist disruption in the cluster. The total mass of the galaxy can be approximated by:

$$m_{tot} \gtrsim 3M\left(\frac{r_d}{D}\right)^3 \quad , \tag{1.2}$$

where D is the radial distance from the cluster centre and M is the cluster mass within the radial distance (Binney & Tremaine, 1987). For UDGs to survive at this radius it would require a total mass $m_{tot} \gtrsim 3 \times 10^9\,M_\odot$. The stellar mass of the UDGs measured by van Dokkum et al. (2015) account for only 2% of the total mass within the tidal radius. The colours of these galaxies indicate they are gas-poor and passively evolving, therefore they likely have high DM content. Yagi et al. (2016) modelled Coma UDGs and determined a tidal mass equivalent to van Dokkum et al. (2015) and identically concluded they probably have high DM fractions. Nearby cluster UDGs were also determined to be highly DM dominated, with a total mass of at least 20 times larger than the median stellar mass (van der Burg et al., 2016).

Beasley et al. (2016) studied VCC 1287, a UDG in the Virgo cluster. They analyzed the dynamics of its globular clusters, and determined a velocity dispersion $v_{sys} = 33^{+16}_{-10}\,\mathrm{km\,s^{-1}}$ in the UDG. They

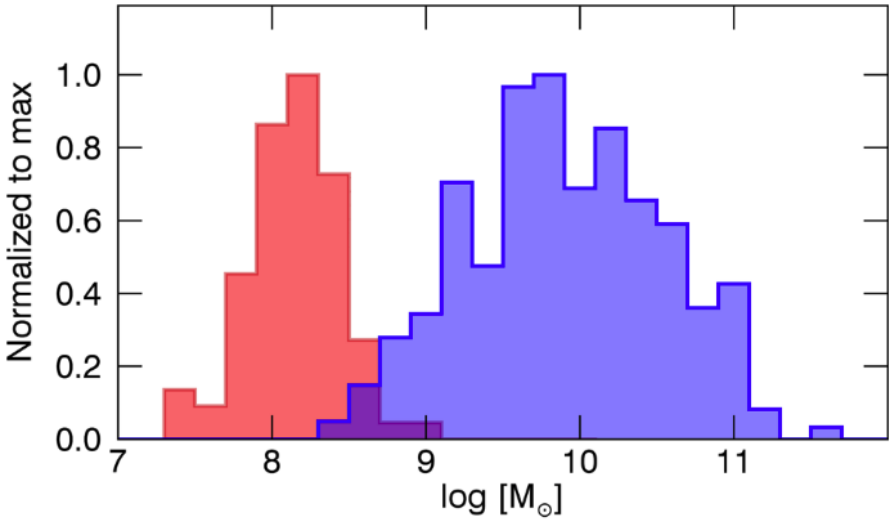

Figure 1.6: The normalized stellar mass distribution of UDGs in red compared to galaxies with measured redshifts in blue for the Abell 168 region. The UDGs clearly peak at a lower stellar mass, whereas galaxies for which spectra can be easily obtained have a higher average mass. The selection effects of the galaxies evaluated results in a clear separation between the UDG and normal galaxy populations, this is likely not the true underlying galaxy distribution. Figure taken from Román & Trujillo (2017a).

estimated the virial mass of the UDG to be $\sim 8 \times 10^{10}\, M_\odot$ from the cumulative mass curve and globular cluster data. Beasley et al. (2016) conclude the stellar mass to DM fraction in VCC 1287 is $\sim 3.5 \times 10^{-4}$, suggesting the DM faction is ~ 100 times greater than the UDGs in Coma. The nearest UDG discovered exists in the M77 group, UGC 2162 (Trujillo et al., 2017b). This galaxy is irregular and blue with star forming regions, quite different to the vast majority of identified UDGs. UGC 2162 lies in an HI gas cloud, with mass $\sim 1.9 \times 10^8\, M_\odot$. The HI mass paired with the stellar mass ($\sim 2 \times 10^7\, M_\odot$) make up less than 1% of the estimated virial radius ($\sim 8 \times 10^{10}\, M_\odot$). This is in line with the DM fractions determined in Coma even though the UDGs have very different compositions.

Studies of UDGs and their abundance in the cluster environment have given rise to the expectation that UDGs have high DM fractions. In contrast, recently a possible UDG (NGC1052-DF2) without DM was investigated by van Dokkum et al. (2018) with follow up in Danieli et al. (2019). Using the Keck Cosmic Web Imager Danieli et al. (2019) found a stellar velocity dispersion of $\sigma_{stars} = 8.5^{+2.3}_{-3.1}\,\mathrm{km\,s^{-1}}$, implying a stellar mass of $M_{stars} = 1.0 \times 10^8\, M_\odot$. The dynamical mass determined from the globular clusters in NGC1052-DF2 is $M_{dyn} = 1.3 \times 10^8\, M_\odot$ (van Dokkum et al., 2018). Both the dynamical and stellar masses are similar which indicates NGC1052-DF2 has much less DM than expected, perhaps it has no DM (Danieli et al., 2019). Van Dokkum et al. (2015) reports a second galaxy (NGC1052-DF4) in the Coma cluster to have no DM, possibly suggesting that UDGs without DM are common in clusters.

1.3.2 Formation Scenarios for UDGs

UDGs have been predominantly found in the cluster environment which is quite unexpected. The diffuse and extended nature of these galaxies suggests that they would not survive in the strong tidal fields of clusters. The existence of UDGs in this environment has prompted research into the formation and evolution of these sources in both the cluster environment and the field (e.g. Carleton et al. 2019; Chan et al. 2018; Román & Trujillo 2017b; Rong et al. 2017).

The Millenium II cosmology simulation (Boylan-Kolchin et al., 2009) and Phoenix simulation (Gao et al., 2012) were used by Rong et al. (2017) to determine that UDGs are dwarf galaxies. Millenium II is an N-body simulation of DM evolution, while the Phoenix simulation is a zoomed-in resimulation of nine different clusters. The spatially-extended size results from a late formation time compared to typical dwarfs and a high spin of the host halo. Amorisco & Loeb (2016) similarly conclude that UDGs are formed from dwarf galaxies with high angular momentum using the standard model of disc formation. Di Cintio et al. (2017) used cosmological zoom-in hydrodynamical simulations from the NIHAO project

(Wang et al., 2015) to determine that UDGs form in halos similar to dwarf galaxies. Gas outflows caused by star formation result in a passively evolving UDG. Therefore Amorisco & Loeb (2016), Rong et al. (2017) and Di Cintio et al. (2017) conclude that UDGs should also exist, quite commonly, in the field. Yozin & Bekki (2015) used numerical simulations to determine that UDGs are under-developed galaxies with quenched growth rates. The overdense environment found in clusters strip the galaxy of gas as it is accreted into the cluster. Carleton et al. (2019) show that observed UDGs are formed from LSB field dwarfs after tidal stripping by neighbouring galaxies in their semi-analytic model. Therefore, among others, Yozin & Bekki (2015) and Carleton et al. (2019) conclude that UDGs are caused by the tidal effects of neighbouring galaxies and the cluster environment. Jiang et al. (2019) use zoom-in cosmological simulations to model the formation of UDGs and determine that UDGs are formed both in the field and in clusters. The field UDGs are caused by supernovae outflows in dwarf galaxies quenching and expanding the galaxy. UDGs in group environments become quenched and diffuse through the effects of ram pressure stripping. More observational constraints on the properties and locations of UDGs will help to distinguish between these possible scenarios.

1.4 Motivation and Outline

In this thesis I examine the effects of the cluster environment on large LSB galaxies in clusters by identifying a new, uniformly selected sample of galaxies in 16 low redshift clusters using Stripe 82 data. This is the largest sample of clusters in which UDGs have been studied to date. Given the limitations on currently available data we investigate a sample that extends to brighter surface brightnesses than the UDG definition of van Dokkum et al. (2015) (hereafter UDG candidates). This increase in the range of surface brightness we study will allow for comparisons between UDGs and a brighter population of dwarf and LSB galaxies.

There are three main goals of this thesis. Firstly, I aim to find any relationship between the properties of the UDG candidates, such as axis ratio, spatial distribution and Sérsic index, by comparatively analyzing them. Secondly, I study the dependence on redshift of the number of UDG candidates in clusters. The goal here is to determine whether the number of UDGs in clusters has changed over time. The final main goal is to determine the effect of cluster halo mass on UDG candidate numbers. Knowledge of cluster halo mass dependence for these UDG candidates may provide insight into the effect of the cluster environment on galaxy evolution.

Chapter 2 describes the methods implemented to select UDG candidates in the clusters. The UDG candidate properties and results are presented and discussed in Chapter 3. Chapter 4 summarizes the relationships found amongst our UDG candidates and future work. We use the following cosmological parameters throughout this thesis: $H_0 = 69.3\,\mathrm{km\,Mpc^{-1}\,s^{-1}}$, $\Omega_m = 0.286$ and $\Omega_\Lambda = 0.713$ (Bennett et al. 2013; Riess et al. 2016).

Chapter 2

Methods

In this chapter I discuss the data used to identify galaixes in clusters and the methods employed to select UDG candidates. The RedMaPPer (Rykoff et al., 2014) cluster catalogue was used to identify clusters with potential UDG candidates. The UDG candidates were identified from the IAC Stripe 82 Legacy Project's extended sources catalogue (Fliri & Trujillo, 2016).

2.1 Data

2.1.1 IAC Stripe 82 Legacy Project

The Stripe 82 area covers 275 deg^2 on the sky with right ascension ranging from $-50.0\,^\circ$ to $+60.0\,^\circ$ and declination ranging from $-1.25\,^\circ$ to $+1.25\,^\circ$. This region has been imaged over 80 times in the Sloan Digital Sky Survey(SDSS) with the Sloan Foundation 2.5m Telescope in the u,g,r,i and z filters (Aihara et al., 2011). The SDSS implemented a drift scan imaging method. The telescope is set to track great circles at the sidereal rate, with exposures of 54.1 s in each filter. The SDSS Stripe 82 data were collected in two strips: north and south. They cover constant lines of latitude but the coverage area generally rises from west to east. The southern strip area increases by about 25% while the northern strip area increases by about 15%. Figure 2.1 displays the spatial coverage of the Stripe 82 region. The northern strip is at positive declinations and the southern strip lies at negative declinations.

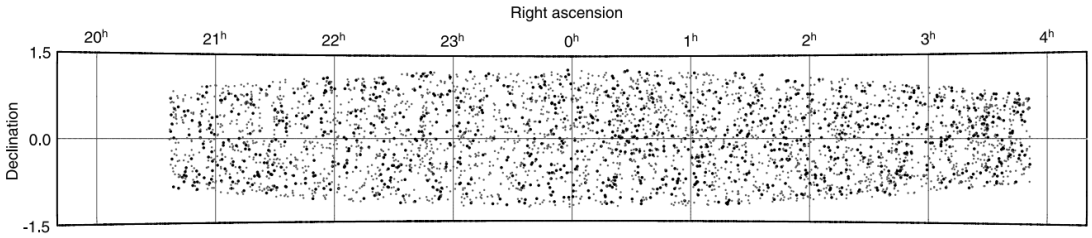

Figure 2.1: The spatial distribution of galaxy clusters determined by Geach et al. (2011). The cluster distribution illustrates the area covered by Stripe 82.

The IAC Stripe 82 Legacy Project (Fliri & Trujillo, 2016) is a wide-area survey to identify the faintest sources in the Stripe 82 region. The IAC Stripe 82 Legacy Project team performed a re-reduction of the SDSS images to reach the faintest sources. The IAC were able to detect these faint sources by measuring and subtracting from their images a more representative background level. This included accurately determining the background noise in all the images, and removing images with high background values. Masks were also used to remove sources which may have affected the calculation of the background, including the faint extended tails of galaxies. A criterion was then imposed on the images to remove images collected during bad observing conditions. The remaining images were aligned and co-added with SWARP (Bertin et al., 2002) software. Each co-added image consists of at least 50 individual images.

The image depth reaches a surface brightness limit of 28.5 mag/arcsec^2, with a $3\,\sigma$ detection at scales of 10×10 arcsec^2 in the r-band. Table 2.1 compares the 50% completeness limit for SDSS Data Release 7 (DR7) (Abazajian et al., 2009) and the co-added IAC images in the different bands. The IAC co-added images have 50% completeness limits for point sources at 24.2, 25.2, 24.7, 24.3, 23.0 mags for the u,g,r,i

and z bands respectively. The DR7 50% completeness limits for point sources have been determined to be 22.3, 23.2, 23.0, 22.6 and 21.1 mags for the u,g,r,i and z bands. The IAC Stripe 82 data is thus 1.9, 2.0, 1.7, 1.7 and 1.9 mags deeper in the respective bands.

Band	DR7 [mag]	IAC [mag]	Gain [mag]
u	22.3	24.2	1.9
g	23.2	25.2	2.0
r	23.0	24.7	1.7
i	22.6	24.3	1.7
z	21.1	23.0	1.9

Table 2.1: Comparison of the 50% completeness limits for points sources in the DR7 and IAC images (Fliri & Trujillo, 2016).

Fliri & Trujillo (2016) used completeness simulations to estimate the completeness limit for extended sources in the IAC reduction of Stripe 82. This was achieved by adding sources with different profile shapes and effective radii to the IAC images and calculating the recovery fraction. The PSFEX (Bertin, 2011) software was used to generate deep Point Spread Function (PSF) frames. The PSFs were used to construct models of extended sources with GALFIT (Peng et al., 2002) which were then added to the images. GALFIT is an algorithm designed to extract galaxy features and model light profiles of spatially resolved sources (a more in-depth description of GALFIT is provided in Section 2.2.4). In total 5000 sources were added to the images per filter and size-brightness combination. The added sources were detected and measured by SExtractor (Bertin & Arnouts, 1996). Each successful measurement required a $3\,\sigma$ detection with 3 connected pixels above 1.74 times the background value. The resulting detection map of the r-band is displayed in Figure 2.2 for both de Vaucouleurs and exponential light profiles. The effective radius is on the y-axis in log scale, with apparent magnitude of the r-band on the x-axis. The completeness fraction is displayed in colour, with 50% completeness displayed in green. The lines of equal effective surface brightness are labelled for the exponential profile. A completeness of 50% is reached at a surface brightness of $\mu_e(r) \sim 25.5\,\mathrm{mag/arcsec^2}$. The 50% surface brightness completeness limit for the u,g,i and z bands are (25, 26, 25, 24) $\mathrm{mag/arcsec^2}$ respectively.

The sources detected by the IAC were separated into a point source catalogue and an extended source catalogue. They used the SExtractor (Bertin & Arnouts, 1996) and DAOPHOT (Stetson, 1987) software packages in conjunction to distinguish between point and extended sources. The properties recorded in the IAC extended catalogue were determined by the SExtractor software. The positions, luminosities, effective radii and structural parameters of the sources were measured. The parameters measured by SExtractor in the IAC catalogue are used extensively throughout our UDG detection algorithm.

2.1.2 RedMaPPer Catalogue

The RedMaPPer (Rykoff et al., 2014) cluster catalogue is used to identify clusters in Stripe 82 which will be examined for UDG candidates. The RedMaPPer cluster catalogue contains 25,236 galaxy clusters in the 10,400 square degrees covered by the full SDSS survey. The RedMaPPer algorithm is a red sequence cluster finder which has been applied to the SDSS DR8 dataset (Aihara et al., 2011) to create a cluster catalogue. Early type galaxies within clusters exhibit a colour-magnitude relation called the red sequence which can be used to estimate galaxy and cluster redshifts (Gladders & Yee, 2000).

There are several reasons for using the RedMaPPer cluster catalogue as opposed to the other available catalogs. Firstly, the algorithm is able to consistently detect galaxy clusters where the photometric data span the 4000 Å break. The SDSS survey in the redshift range $0.05 < z < 0.55$ satisfies this criteria, and suits our search for low redshift clusters. Secondly, the cluster catalogue contains a cluster membership probability for the galaxies used to determine the cluster's properties. We were able to use this to better refine our cluster membership selection. Finally, the cluster richness estimates are also provided for each cluster. This is a very important parameter which we need to make our cluster mass

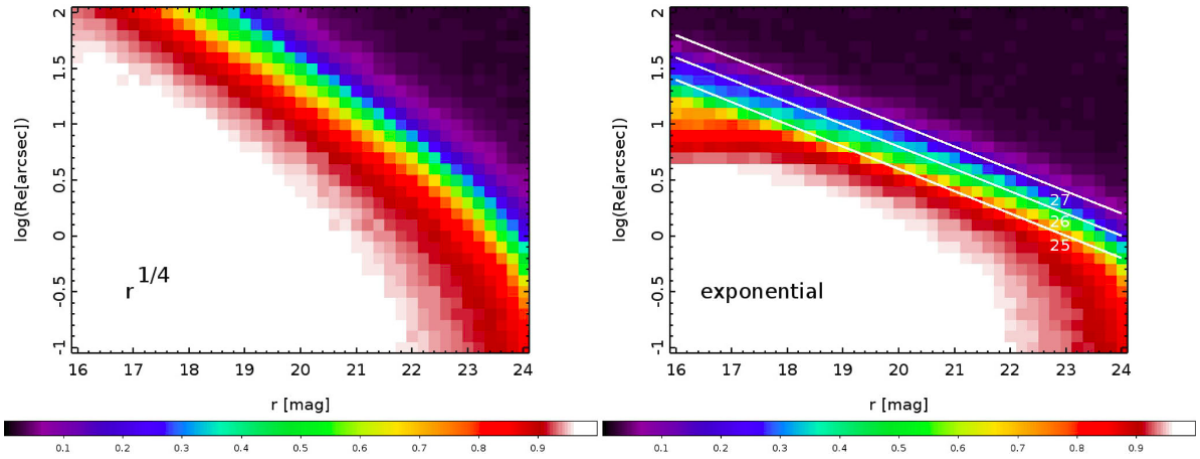

Figure 2.2: Detection map from the IAC Legacy survey paper (Fliri & Trujillo, 2016) displaying the recovery fraction of simulated extended sources in the r-band. On the left is recovery fraction for de Vaucouleurs profiles and the right exponential profiles. The lines of equal effective surface brightness at $\mu_e(r) = 25, 26, 27\,\mathrm{mag/arcsec^2}$ are also shown in the image.

estimates. The richness estimate (λ) is a measure of the number of galaxies within a cluster and can be directly related to the cluster mass (Simet et al., 2018).

However the RedMaPPer algorithm is not perfect and does fall short in determining the centres of clusters which have a population of galaxies undergoing strong star formation. These galaxies are bluer and do not lie on the red sequence. Therefore these galaxies are not considered when determining the cluster centre and result in an incorrect cluster centre measurement and furthermore, the cluster parameters. Rykoff et al. (2014) have estimated the rate of miscentering due to blue cluster galaxies and have found that less than 2% of clusters are likely to be miscentered. The clusters we investigate are at low redshifts, where the galaxies are expected to follow the cluster's red sequence more consistently and therefore are unlikely to be affected by this miscentering.

The RedMaPPer algorithm relies on the identification of the red sequence. The old stellar population in cluster galaxies have similar spectral energy distributions (SEDs). The 4000 Å break is one of the significant features observed in these SEDs, which Rykoff et al. (2014) utilized to find the red sequence. Figure 2.3 displays a typical elliptical galaxy SED and its 4000 Å break with respect to the different SDSS wavelength filters. For effective cluster detection the red sequence needs to be calibrated. Rykoff et al. (2014) identified red spectroscopic galaxies in the SDSS DR8 dataset and used these to initially calibrate the red sequence. The mean colours of these galaxies were then determined as a function of redshift and the mean colour-redshift relationship was subsequently used to identify the final sample of "seed" galaxies. All galaxies found within $500\,h^{-1}$ kpc of these "seed" galaxies having colours consistent with the spectroscopic colour-redshift relationship were selected. These galaxies were used to fit a new red sequence and measure the cluster richnesses. The galaxies in overdense regions were assigned the same redshift as the initial "seed" galaxy; this was the training sample. The training sample was then input into the cluster finder, which we shall describe below. The output thereof was used to re-calibrate and improve the red sequence colour-redshift relationship.

Figure 2.4 displays the procedures implemented by the cluster finder. The input catalogue consists of the training sample created in the calibration stage. In the first pass the galaxies in the training sample are reduced through modest statistical and luminosity criteria. The richness of every cluster galaxy is then calculated within a $500\,h^{-1}$ kpc radius. Central cluster galaxy candidates in clusters with low richnesses are rejected. The richnesses and associated membership probabilities for each cluster galaxy are then determined. A new redshift estimate is made by selecting high membership probability galaxies and maximizing the likelihood function described in Rykoff et al. (2014). A convergence in the redshift is reached by iterating the above richness and membership probability calculation with the likelihood function. The galaxies are then passed through the Likelihood Sorting phase, which sorts the galaxies by their richness likelihood and centering likelihood (Rykoff et al., 2014). The Percolation phase assigns galaxies to clusters and avoids assigning a galaxy to multiple clusters. Firstly, the richness and redshift of

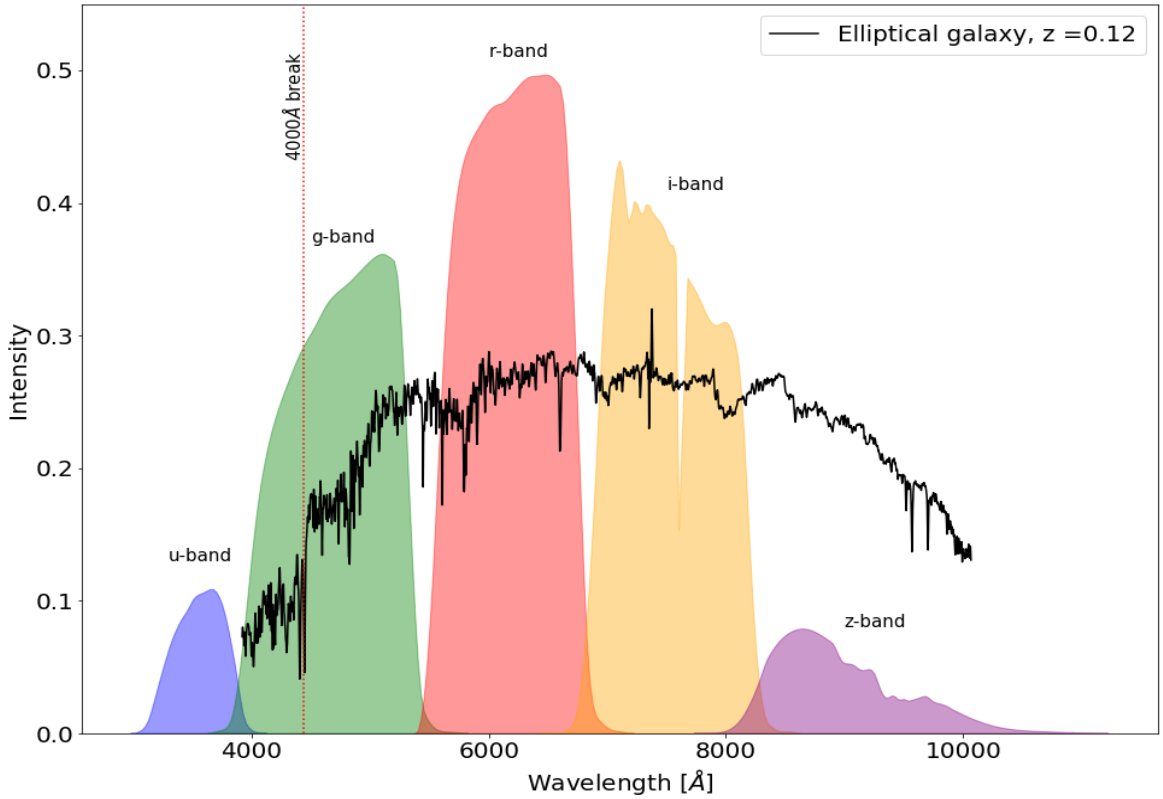

Figure 2.3: A typical elliptical galaxy SED shifted to redshift $z = 0.12$. The SDSS wavelength coverage of each filter (u, g, r, i and z) is also displayed in this image to identify the position of the 4000 Å with respect to the filters. Plot adapted from code developed in Pedregosa et al. (2011).

each cluster is recalculated. Following this, the cluster centre and centering probabilities are calculated. The richnesses and redshifts are then updated. Updates to the galaxy catalogue are made based on membership probabilities. All galaxies with a lower possible cluster centre rank and high cluster membership probability are removed from being a potential cluster centre. The Percolation phase is then iterated for all subsequent galaxies until all galaxies are appropriately assigned.

I have used the cluster richness provided by RedMaPPer to estimate the halo masses of the clusters, described in the following sections. The clusters in the RedMapper catalogue have richness values $\lambda \geq 20S(z_\lambda)$, where $S(z_\lambda)$ relates the galaxy counts to richness when the data are not deep enough to reach $0.2L_*$. Therefore each cluster has effectively a minimum of 20 galaxies with either fluxes above the survey flux limit or fluxes above $0.2L_*$ at the cluster redshift. The luminosity limit reduces the scatter in the mass-richness relationship (Rykoff et al., 2012). The mass-richness relation is an optical indicator for the mass of a cluster given the number of identified cluster members. The scatter in the mass-richness relation of a cluster arises from the cluster members themselves having varied properties, including mass, luminosity, radius, etc. By limiting the luminosity to the brightest sources in a cluster the minimum mass of the members is also limited and therefore the mass-richness relationship will have fewer outliers and less scatter.

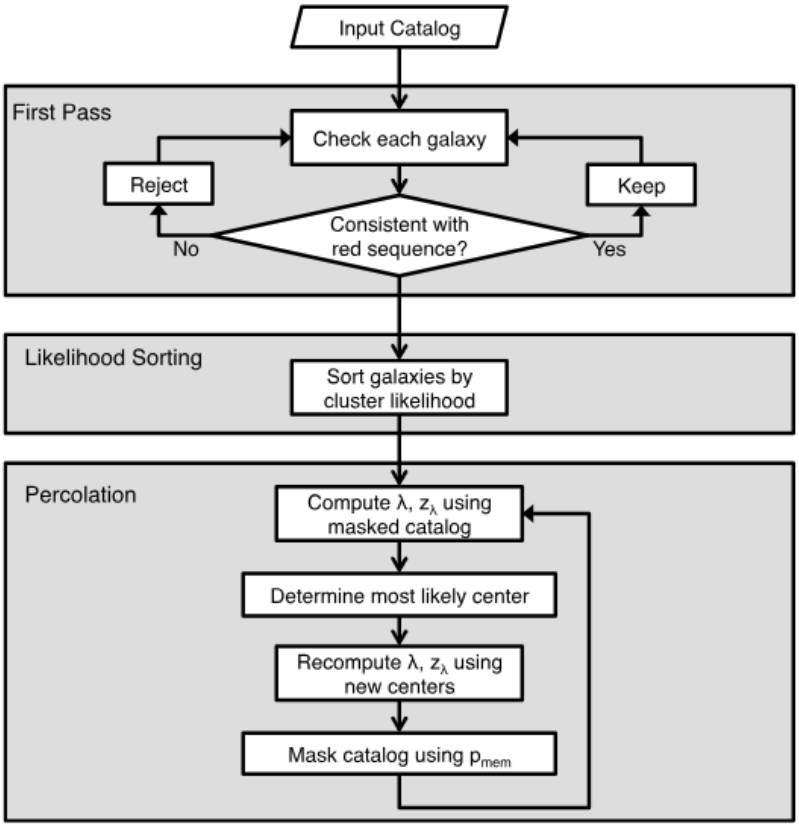

Figure 2.4: A flowchart of the procedures of the cluster finder used by RedMaPPer. Taken from Rykoff et al. (2014).

2.2 Sample Selection

The UDG candidate selection algorithm we have implemented has several steps which we list below and describe in detail in the following sections:

1. Cluster identification
2. Preliminary source identification
3. Cluster member identification
4. Estimation of galaxy properties through model fitting
5. UDG candidate selection
6. Coverage correction
7. Background correction

2.2.1 Cluster Identification

We used the RedMaPPer cluster catalogue to identify clusters with potential UDG candidates. The clusters selected were limited to the Stripe 82 region and low redshifts. A redshift limit $z < 0.15$ was chosen to ensure all potential candidates in their respective clusters were resolvable. The IAC co-added SDSS images have a $0.396''$/pixel scale, a median seeing of $1.1''$ and a median FWHM $= 1.24''$ in the g-band for the PSF as seen in Table 2.2. Taking the FWHM as the minimum diameter from which galaxy properties can be accurately determined results in a requirement that a galaxy spans at least 3.13 pixels in the images. The cluster with the lowest redshift ($z = 0.0921$) has a size scale of 0.683 kpc/pixel while the highest redshift cluster ($z = 0.1454$) has a size scale of 1.016 kpc/pixel. Therefore the minimum galaxy radius for the highest redshift cluster is 1.59 kpc. For the lowest redshift cluster the minimum radius is 1.07 kpc.

Band	FWHM [arcsec]
u	1.31
g	1.24
r	1.10
i	1.02
z	1.04
r_{deep}	1.08

Table 2.2: The median full width at half-maximum values for the PSF, taken from Fliri & Trujillo (2016).

Table 2.3 displays the details of all 16 clusters explored. The cluster positions, redshifts and richnesses, λ, are shown alongside richness scale factors, S (Rykoff et al., 2014), and cluster masses, M_{200m}. The richness scale factor accounts for effects caused by the survey depth, including missing and masked regions. The number of galaxies above the magnitude limit of the survey is determined by $\frac{\lambda}{S}$. M_{200m} is the cluster mass measured at radius r_{200m}, where r_{200m} is the radius at which the mean density within is 200 times the mean matter density of the universe at the cluster's redshift. The cluster mass equation (Simet et al., 2018) with statistical and systematic error is given by

$$< M_{200m}|\lambda >= 10^{14.369 \pm 0.021\,\text{stat.}\ \pm 0.023\,\text{sys.}} \left(\frac{\lambda}{40}\right)^{1.30^{+0.10}_{-0.09}}. \tag{2.1}$$

Figure 2.5 displays the distribution of redshifts, richnesses and masses of our selected clusters as well as the spread in mass vs. redshift. We can see an even spread in clusters across redshift. The richness and mass distributions are similar, decreasing in number as richness/mass increases. From the mass vs. redshift plot we can see a relatively flat distribution with no obvious trend.

No	ID	RA [deg]	DEC [deg]	z_λ	λ	S	M_{200m} $[h^{-1}M_\odot]$
1	4873	338.7998	-1.1472	0.0921	25.91	1.03	1.33×10^{14}
2	8897	353.8570	1.0591	0.0944	24.06	1.01	1.21×10^{14}
3	3198	353.3446	-1.1486	0.1004	39.01	1.01	2.26×10^{14}
4	4645	11.4576	-0.8504	0.1059	27.25	1.03	1.42×10^{14}
5	8361	5.4323	-0.8544	0.1071	23.42	1.01	1.17×10^{14}
6	2688	323.9146	0.1659	0.1189	39.73	1.01	2.32×10^{14}
7	8751	330.1560	-0.5459	0.1216	28.41	1.07	1.50×10^{14}
8	5001	11.6008	0.0024	0.1221	24.63	1.02	1.24×10^{14}
9	5202	11.8812	-0.8825	0.1248	26.47	1.01	1.37×10^{14}
10	15150	23.2281	0.9760	0.1291	22.29	1.03	1.09×10^{14}
11	752	321.4432	0.9311	0.1325	56.78	1.01	3.69×10^{14}
12	2979	322.6123	-0.0068	0.1348	34.77	1.01	1.95×10^{14}
13	2098	15.6795	1.1363	0.1384	35.06	1.01	1.97×10^{14}
14	3964	13.4426	-0.7803	0.1404	37.30	1.02	2.14×10^{14}
15	14226	336.2302	-0.3840	0.1446	22.26	1.00	1.09×10^{14}
16	9086	351.0900	0.3191	0.1454	25.50	1.01	1.30×10^{14}

Table 2.3: List of all 16 clusters at $z < 0.15$ identified in the RedMaPPer cluster catalogue that form our sample. The clusters are ordered according to increasing redshift. The positions (RA and DEC), redshift (z_λ), richness (λ), richness scale factor (S), and cluster mass (M_{200m}) are all identified in the table.

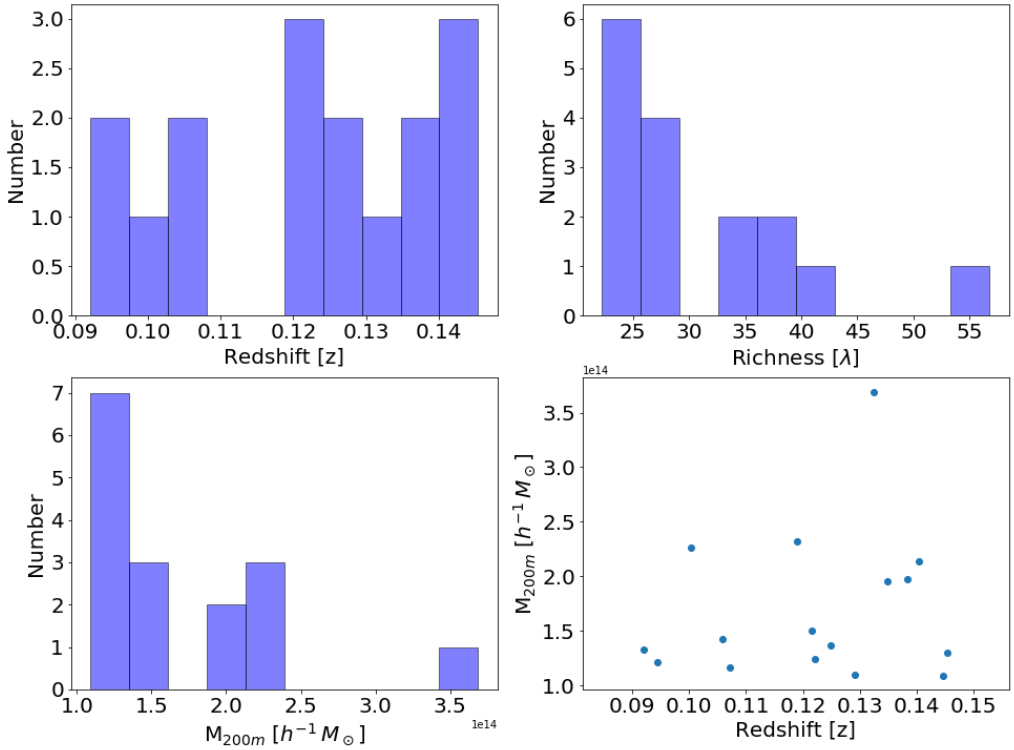

Figure 2.5: Histograms displaying some of the properties of the 16 RedMaPPer clusters in our sample. Top-left panel: The redshift distribution of our cluster sample. Top-right panel: Distribution in richness of the sample. Bottom-left panel: Distribution of mass of the clusters in the sample. Bottom-right panel: Plot of the mass vs. redshift. The masses of the clusters are quite similar across the redshift range.

2.2.2 Preliminary Source Identification

Once we have identified all the clusters that satisfy our selection criteria, we identify which galaxies are associated to each cluster. The virial theorem relates the total potential energy and kinetic energy of a system. The r_{200m} radius depends on the density of the system relative to the critical density of the universe at the system's redshift. We used the following equation to calculate the r_{200m} radius from the M_{200m} mass (Navarro et al., 1996):

$$r_{200m} = \frac{GM_{200m}}{100H_0^2} \quad , \tag{2.2}$$

where G is the gravitational constant and H_0 is the Hubble constant. Figure 2.6 displays a histogram of the r_{200m} radii for all the clusters. As an example, Figure 2.7 shows the image of cluster 5202 from the the RedMaPPer cluster catalogue with the r_{200m} radius identified with the blue circle. We used the IAC extended source catalogue to identify all sources within the r_{200m} radius of each cluster. This initial selection of extended sources includes foreground and background sources.

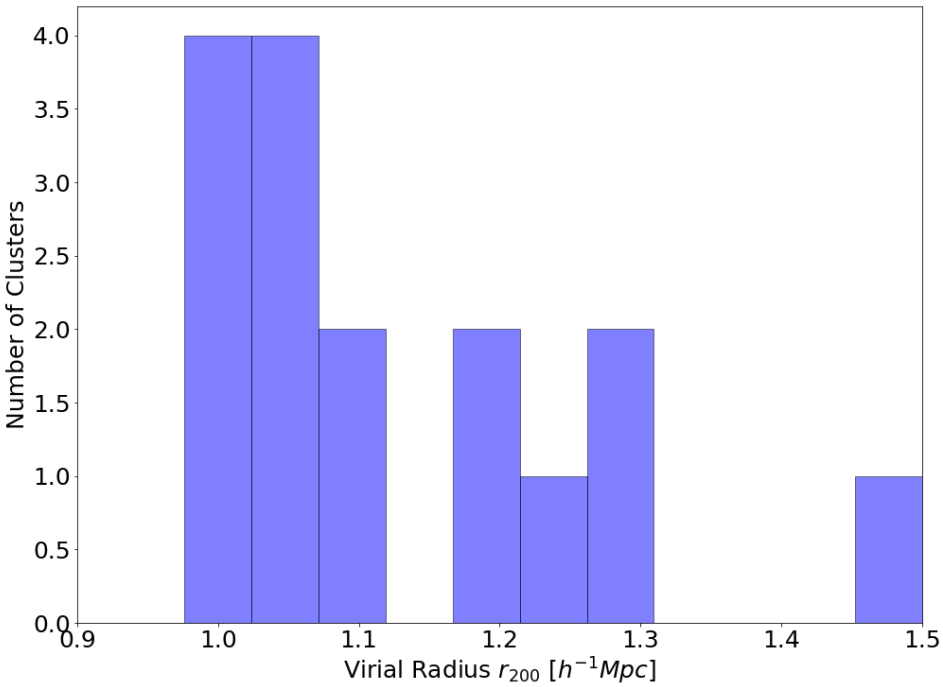

Figure 2.6: Histogram of the r_{200m} radii for the identified 16 clusters.

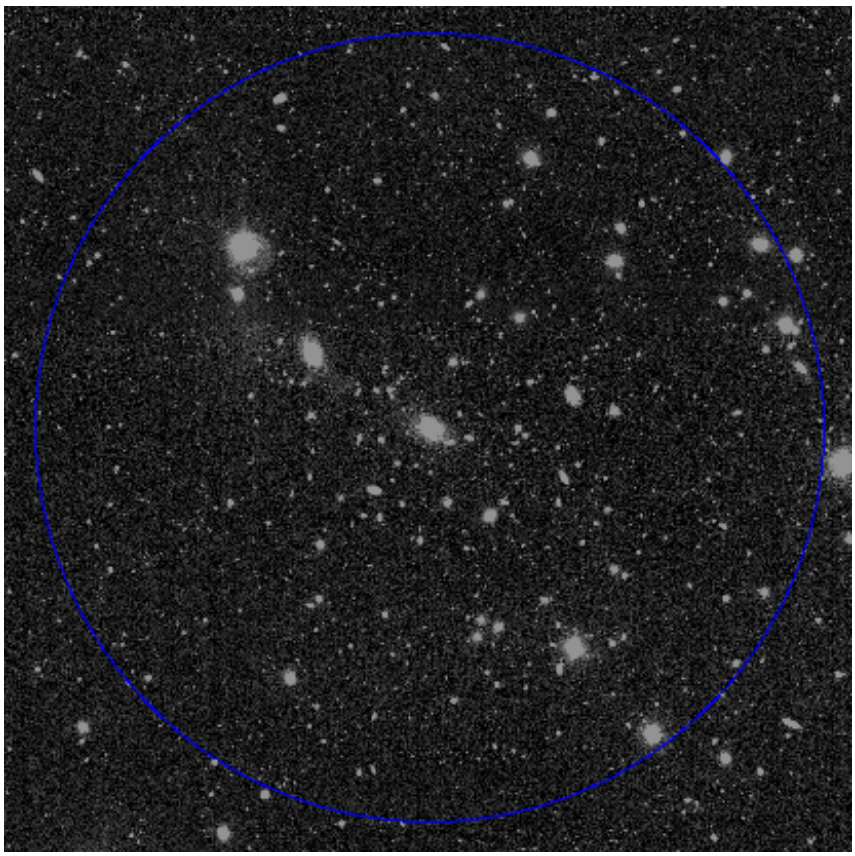

Figure 2.7: IAC SDSS image of Cluster 5202 in the g-band. The r_{200m} radius (blue circle), $r_{200m} = 1.067\,\mathrm{Mpc}$, is used to identify the area of the cluster.

2.2.3 Cluster Member Identification

The next step is to distinguish cluster members from foreground and background sources. We use the red sequence to separate cluster members from other sources. The 4000 Å break is one of the significant features observed in the spectra of typical cluster galaxies which we utilize to find the red sequence. Figure 2.3 displays this feature clearly, there is an increase in opacity for wavelengths shorter than 4000 Å . This attribute is caused by ionized metals in stars, therefore this effect is more prominent in old, metal-rich stars and galaxies (Kauffmann et al., 2003). The red sequence is identified by measuring the colour from two bands which the 4000 Å break crosses. One caveat of using this method is that the galaxies identified are likely cluster members, however not all the cluster members are identified from the color cut. Figure 2.3 displays the spectrum of an elliptical galaxy at a redshift of 0.12, at the centre of my redshift window. I have selected the $g-r$ colour as this feature lies within the g-band. There are two main implications of using this method. The first is the loss of metal-poor or younger cluster members. The second is the inclusion of foreground and background sources which satisfy the colour cuts. Consequently bluer candidates will be lost with this selection process and non-cluster members may be included.

The sources within the r_{200m} radius were first corrected for Galactic extinction (Schlafly & Finkbeiner, 2011). Galactic extinction is a phenomenon where light emitted from distant sources within our galaxy as well as sources external to our galaxy is scattered and absorbed by dust in our Galaxy. This dust is composed of elements produced in stars and has been ejected into the interstellar medium throughout the lives of stars. Sources within each cluster are all corrected by the same amount, using the value of the extinction at the centre of each cluster.

To determine the cluster members we identified the red sequence of each cluster by measuring the colours of the previously identified RedMaPPer galaxies (Rykoff et al., 2014), and extrapolating to fainter magnitudes. These RedMaPPer galaxies were used to find the cluster and measure its parameters. I selected only RedMaPPer galaxies with a cluster membership probability greater than 0.5 for the red sequence measurement. This allows us to implement a tighter red sequence colour fit, as those galaxies with low probabilities are less likely to be members of the cluster. A single RedMaPPer galaxy in cluster 6 was excluded, with a large colour difference from the red sequence. Using the IAC Stripe 82 extended source catalogue I cross-matched and identified the RedMaPPer galaxies in the IAC catalogues to within $2''$.

Figure 2.8 displays the sources within the r_{200m} radius of sample cluster 9, $g-r$ colour against r-band magnitude. I use the magnitudes from the IAC catalogue for all the sources, including the RedMaPPer galaxies. The red points show the RedMaPPer galaxies and all the IAC sources are in blue. The RedMaPPer galaxies are much brighter than the galaxies we are interested in. The top-left panel displays all the sources, the top-right panel displays the determined red sequence. After fitting a straight line to the red sequence I rotated the data to the horizontal using the y-intercept as an anchor. The bottom-left plot displays the rotated data with the rotated red sequence identified with the green line. The bottom-right panel displays the red sequence sources with black dots. Appendix 5.1 displays the red sequence colour selection for all 16 clusters.

Figure 2.9 displays a histogram of the maximum $g-r$ colour widths of the RedMaPPer galaxies in each cluster. Most clusters (15 out of 16) have a tight red sequence, with a maximum colour difference of 0.3 mags or less. We therefore chose the size of the $g-r$ colour cut to be 0.3 mags, i.e. for each cluster we selected only the galaxies with $g-r$ colours that are less than 0.15 mags from the cluster's $g-r$ colour. A tighter red sequence colour cut will include a higher proportion of cluster members as opposed to a wider cut which is more likely to include foreground and background sources. By implementing a tighter selection we may lose some potential candidates, however we reduce contamination in all other clusters. In this respect we have a more conservative and pure sample compared to having a higher completeness with more contamination. Figure 2.10 is an enlarged plot of the bottom-right panel from Figure 2.8. The black dots identify all sources considered to be potential cluster members.

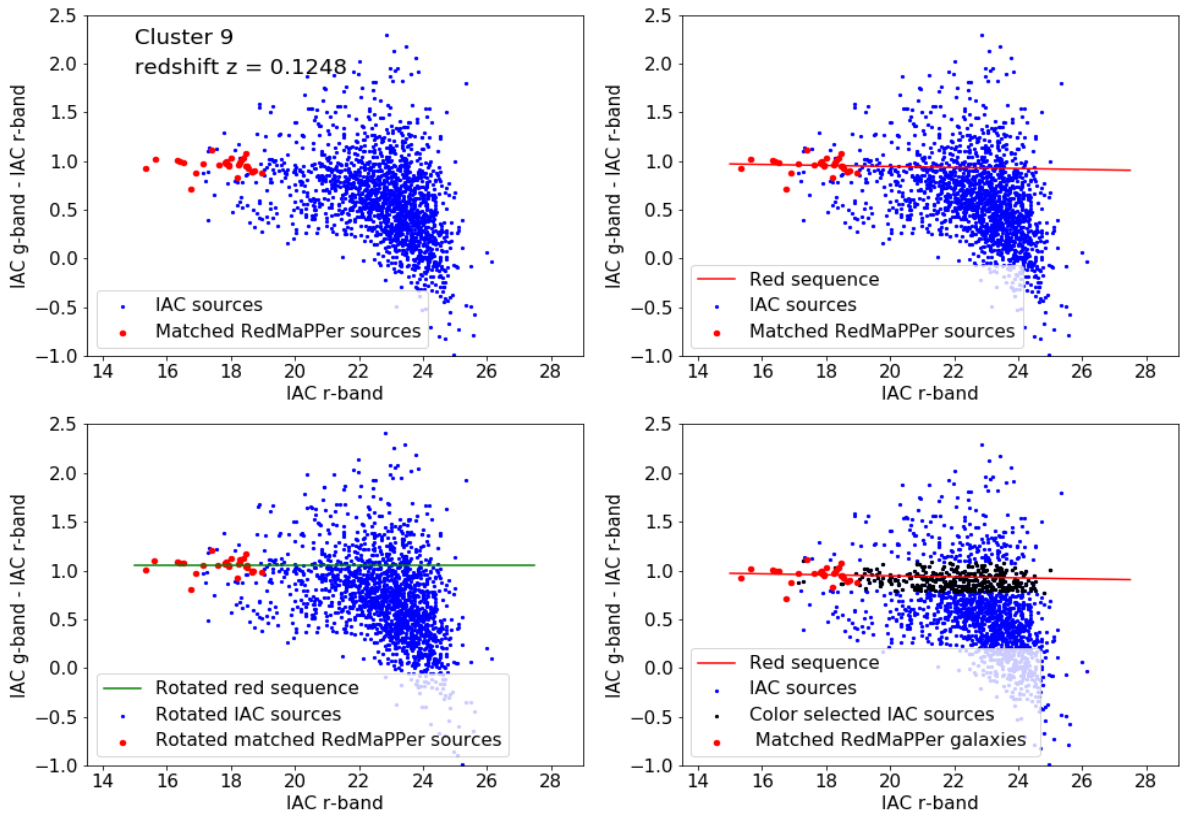

Figure 2.8: Sources in cluster 9. The red dots indicate galaxies utilized by RedMaPPer in their cluster identification. The blue dots are all the sources within the r_{200m} radius of the cluster from the deeper IAC catalogue. The top-left panel displays the distribution of $g-r$ colour as a function of r-band magnitude. The top-right panel shows the red sequence identified by the red line. The bottom-left displays all the data rotated to the horizontal with the red sequence identified by the green line. The bottom-right panel displays all the sources identified as cluster members by the red sequence in black.

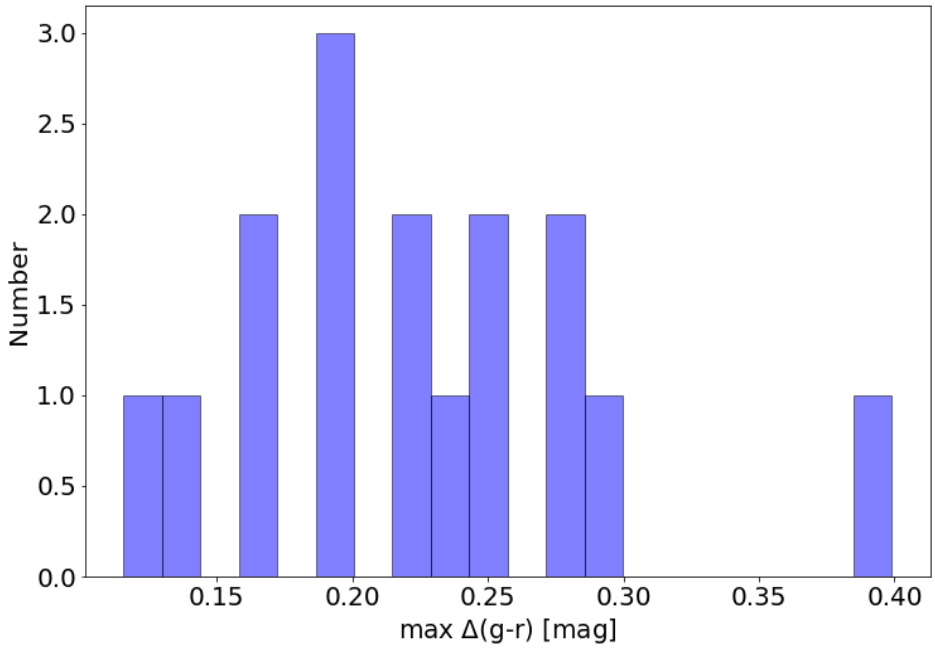

Figure 2.9: Histogram of the maximum $g-r$ colour widths of the RedMaPPer galaxies with membership probabilities above 0.5 in each cluster.

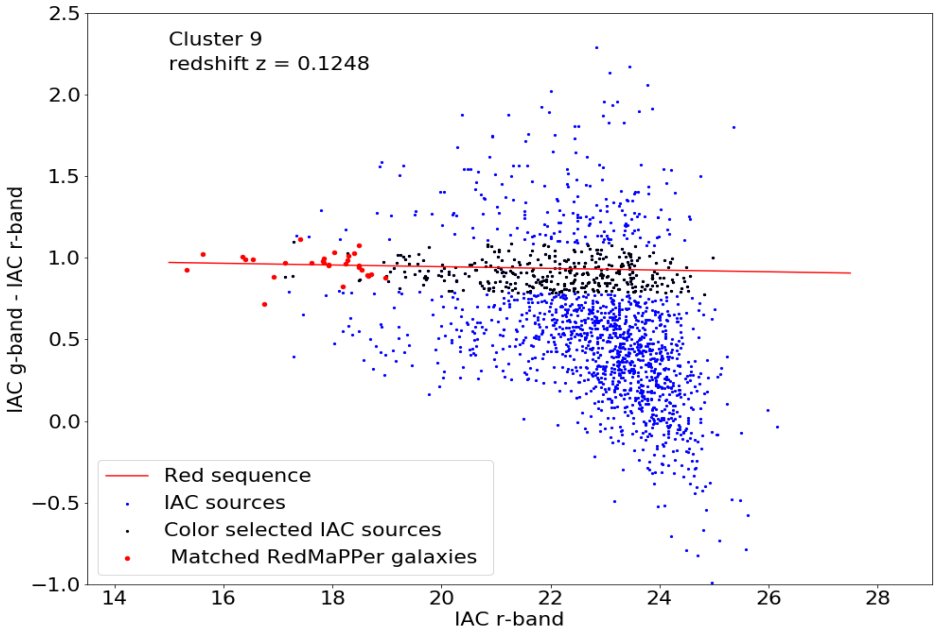

Figure 2.10: An enlarged plot of the bottom-right panel from Figure 2.8. The red dots indicate galaxies utilized by RedMaPPer in their cluster identification. The blue dots are all the IAC sources within the r_{200m} radius of the cluster. The black dots indicate all the potential cluster members identified within 0.15 mags of the red sequence fit.

2.2.4 Estimation of Galaxy Properties Through Model Fitting

The GALFIT (Peng et al., 2002) software measures the properties of galaxies in FITS images through two dimensional profile fitting. I have used GALFIT to determine the surface brightness, the effective radius and Sérsic index of my cluster members from the IAC g-band co-added images. The Sérsic profile (Sérsic, 1963) is a measure of how the light from a galaxy is distributed over its area. We used the galaxy surface brightness as the flux parameter to determine the Sérsic profile. The Sérsic function (Sersic, 1968) can be written as:

$$I(r) = I_e\, e^{-b_n\left[\left(\frac{r}{r_e}\right)^{\frac{1}{n}}-1\right]} \quad , \tag{2.3}$$

where n is the Sérsic index,
r_e is the effective radius containing half the total light of the model profile,
I_e is the surface brightness at r_e,
$I(r)$ is the major-axis brightness profile,
r is the major-axis radius,
$b_n \simeq 0.868\, n - 0.142$ (Caon et al., 1993a).

Large values of n represent a steep, central light concentration and a shallow decline toward the outer regions with extended wings. A smaller n represents a shallower and more evenly spread light distribution at the centre with a sharp truncated outer wing. These features are displayed in Figure 2.11. A Sérsic index of $n = 1$ corresponds to an exponential intensity profile and a de Vaucouleurs profile has a Sérsic index of $n = 4$.

To effectively run GALFIT, certain parameters need to be appropriately set. I describe these parameters below. I input into GALFIT the positions of all the candidates, the g-band magnitudes and radii from the IAC catalogue as initial estimates. For the initial Sérsic index, axis ratio and position angle estimates I used a value of 1 as the IAC catalogue does not provide these. A Sérsic index of $n = 1$ corresponds to a source with an exponential intensity profile. An axis ratio of $b/a = 1$ corresponds to a source with

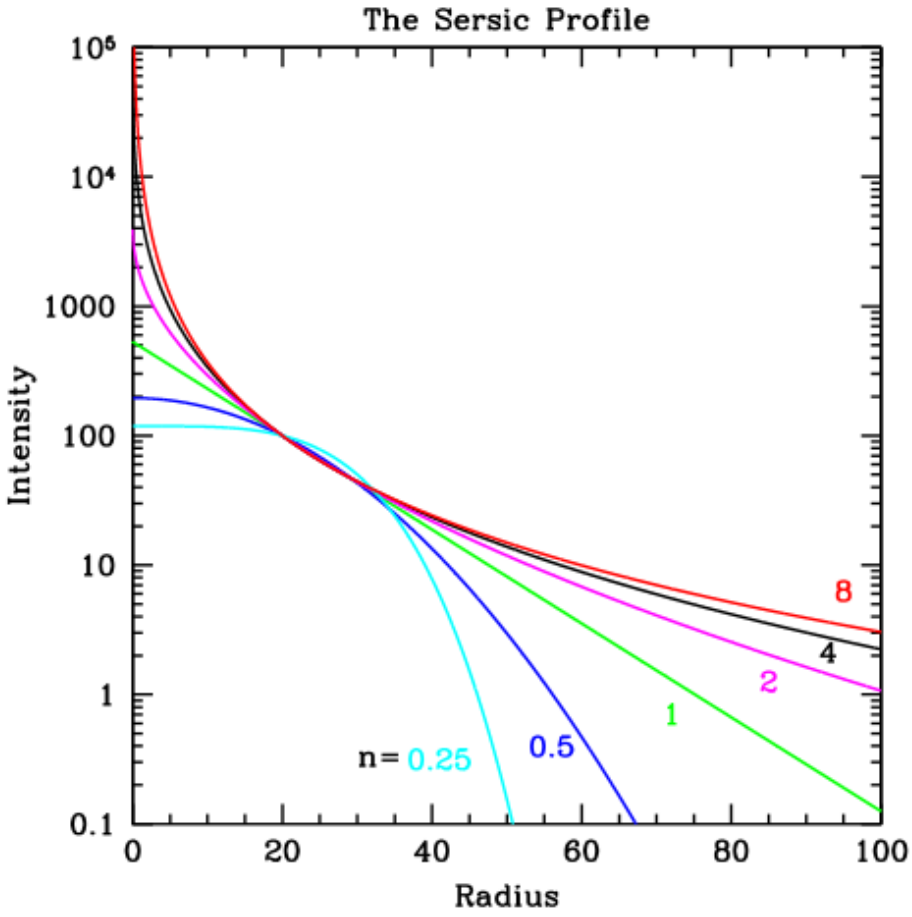

Figure 2.11: The Sérsic profiles for a range of Sérsic indices are displayed. Exponential profiles have an index of 1, while an index of 4 indicates a de Vaucouleurs profile. Image taken from Peng et al. (2010).

circular morphology. A position angle of $PA = 1$ corresponds to a source which is rotated by 1 degree; as we are not inspecting each image for an initial orientation the value selected was non-specific and standard for all sources. GALFIT requires the point spread function (PSF) of the image as input. I used the PSFs provided by the IAC legacy survey.

Segmentation maps were created using SExtractor (Bertin & Arnouts, 1996) to identify all sources in an image. The IAC have stacked the co-added g, r and i band images and created the deeper r_{deep} images. These images reach 3σ surface bightness limits of $\sim 28.5\,\mathrm{mag/arcsec^2}$. I created the segmentation maps using these r_{deep} images as they are deeper than the individual images in any band, therefore fainter sources can be identified in them. This allows for contaminating sources to be properly masked. For each UDG candidate the segmentation maps were used to mask all sources other than the current candidate. This avoids the merging of nearby sources with our candidates and incorrectly modelling prospective UDG candidates. A sample mask is shown in the 4^{th} panel of Figure 2.12, where the white areas identify the masked sources.

GALFIT is an iterative algorithm, which uses the χ^2 statistic to determine a convergence of the model to an appropriate fit. The reduced χ^2 for each galaxy determines the goodness of fit of the model and how to adjust the model parameters for the subsequent iterations.

An example of the output from GALFIT is displayed in Figure 2.12. The images from left to right are the data image, model, residual and mask respectively. The scale of the images is in pixels, with each image cutout having dimensions of 40×40 pixels, corresponding to $15.84''$ per side. The residual image is the data image with the model subtracted from it. Good models have residuals which have no significant bright or dark features at the galaxy's position. GALFIT also outputs the properties of the model galaxy: the surface brightness, effective radius, Sérsic index, axis ratio and position angle, along with their respective errors.

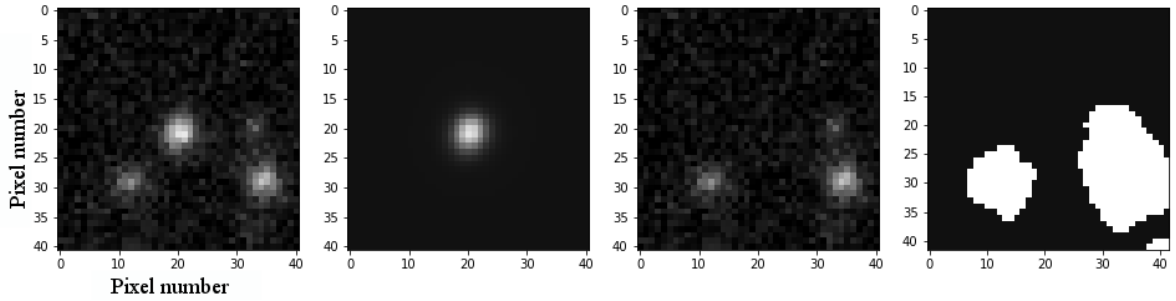

Figure 2.12: An example of the GALFIT output for a galaxy in cluster 5202. From left to right: g-band co-added image, model of galaxy, residual and the mask.

2.2.5 UDG Candidate Selection

GALFIT was run on all the sources which were determined to be potential red sequence cluster members; these included UDG candidates as well as non-UDG candidates. Several sources were immediately removed from the sample as GALFIT was unable to converge and model them. On average 37.2% of the sources could not be modelled. GALFIT fails to model galaxies where the surface brightness is too faint compared to the background, the size of the galaxy is too small to create a model and determine its properties or too many galaxies are concentrated in close proximity. Table 2.4 displays the number of sources which passes the $g-r$ colour (N_{g-r}) and the number successfully modelled by GALFIT (N_*). In the following I will use cluster 9 to illustrate the various quality cuts we applied to the GALFIT results before identifying UDG candidates. Figure 2.13 displays the properties of a subset of all the members of cluster 9. The full sample of all clusters is displayed in Appendix 5.2. The top-left panel shows the spread in radius as the surface brightness grows fainter. The top-right, bottom-left and bottom-right panels display the surface brightness, radius and Sérsic index values and their relative errors. The errors are given as a percentage of the respective value, some of which are rather high. Determining the radius for very small sources can be very difficult given the limits of the GALFIT software.

The percentage errors of the GALFIT model parameters are quite large, specifically the Sérsic index, as seen in Figures 2.13 - 2.16 and Appendix 5.2. The large uncertainties in the model parameters are possibly caused by several aspects. The faint sources I am modelling are hard to distinguish above the sky background as the signal-to-noise is low. Therefore, the weak signal from these sources may make the size and luminosity determinations more uncertain. The fluctuating sky background, stars and neighbouring galaxies in the different images near our clusters may cause an increase in the uncertainty as they are globally set for all sources in a cluster, opposed to uniquely determining them for each galaxy. These effects cannot be precisely quantified by the models and therefore the uncertainty increases. We employed the Sésic index cut to remove very diffuse unresolvable sources as well as the likely poorly modelled sources. The galaxy models that passed all the cuts were visually inspected for bad residuals and offset positions by myself and both my supervisors independently and cross-checked. Only sources with parameters which seemed to accurately fit the model galaxies were passed. Furthermore, by using the Sérsic cut and visual inspection I remove poorly modelled sources irrespective of their parameter uncertainties.

The Sérsic indices below 0.1 indicates very diffuse unresolvable sources. In Figure 2.13 these sources with low Sérsic values are identified with the red ellipse in the bottom-right panel. As the candidates we are looking for are extended sources I remove these sources to avoid including sources in the sample with very large uncertainties on their measured values. Figure 2.14 displays the properties of a subset of all the members of cluster 9 after applying the Sérsic index > 0.1 restriction. The most compact and possibly poorly modelled sources have been removed, as can be seen in the bottom-right panel of Figure 2.14.

Van Dokkum et al. (2015) state that for a galaxy to be a UDG it needs to meet two criteria:

$$\text{surface brightness}: \quad \mu_0(g) \gtrsim 24\,\text{mag/arcsec}^2 \tag{2.4}$$

$$\text{radius}: \quad r_e \gtrsim 1.5\,\text{kpc}. \tag{2.5}$$

I applied a similar selection criteria on the resulting sample, utilizing a brighter cut in surface brightness, as well as an upper limit on radius.

$$\text{surface brightness}: \quad \mu_e(g) \gtrsim 24\,\text{mag/arcsec}^2 \tag{2.6}$$

$$\text{radius}: \quad 1.5\,\text{kpc} \lesssim r_e \lesssim 7.0\,\text{kpc}. \tag{2.7}$$

Our surface brightness cut equates to a central surface brightness of $\mu_0(g) \gtrsim 22.18\,\text{mag/arcsec}^2$ assuming an exponential light profile. Therefore our resulting UDG candidates sample includes brighter sources. We directly compare our UDG candidate sample to the van Dokkum et al. (2015) UDGs in Section 3.1.6. Figure 2.15 displays the properties of all the remaining members in cluster 9. The remaining galaxy sample has much smaller percentage errors for all measured parameters compared to the plots before the cuts were applied.

Finally, to ensure the final sample of UDG candidates have been modelled well I along with my supervisors independently visually inspected each UDG candidate model to reject sources that had bad residuals or were incorrectly centered. The results were compiled and successful candidates required a 2/3 agreement on well-fit models. The final number of UDG candidates after visual inspection is displayed in Table 2.4. The final UDG candidate selection for cluster 9 is displayed in Figure 2.16. Two examples of the GALFIT output of sources are shown in Figures 2.17 and 2.18. The source identified in Figure 2.17 is both relatively large and bright with respect to the rest of the sample, and these two properties can easily be seen in the GALFIT figures. Figure 2.18 displays the model output for the second source, which is both relatively brighter and smaller than the first.

Table 2.4 displays the numbers of UDG candidates in each cluster as they are filtered through the selection algorithm steps. Through this we can identify how each step affects the number of UDG candidates in these clusters.

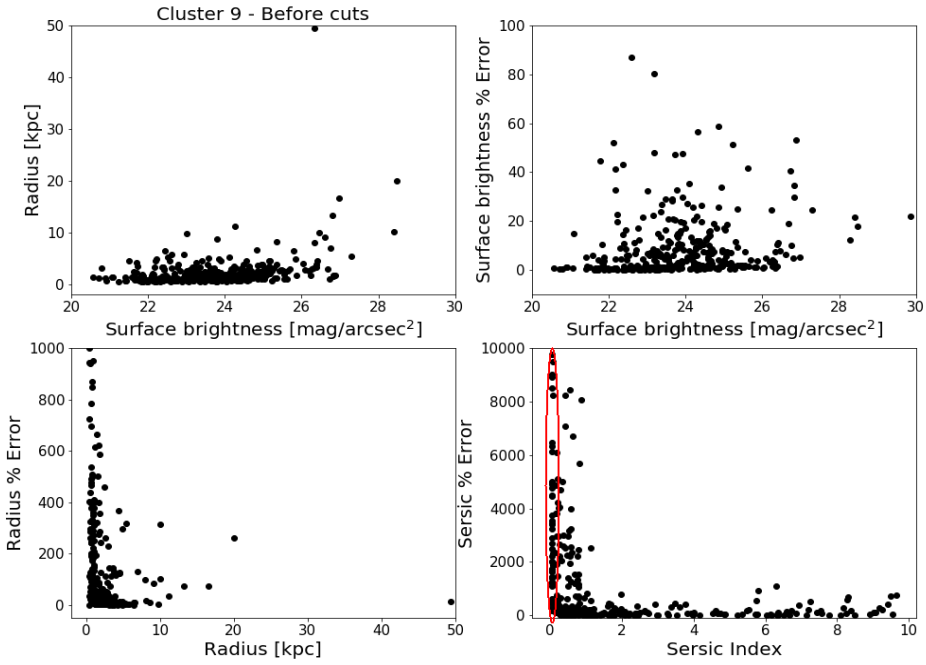

Figure 2.13: Four panel plot containing the dense region of all the sources in cluster 9, which were modelled by GALFIT. The complete sample of all clusters is shown in Appendix 5.2. The red ellipse in the bottom-right panel indicates Sérsic indices of the source which are removed with the Sérsic cut.

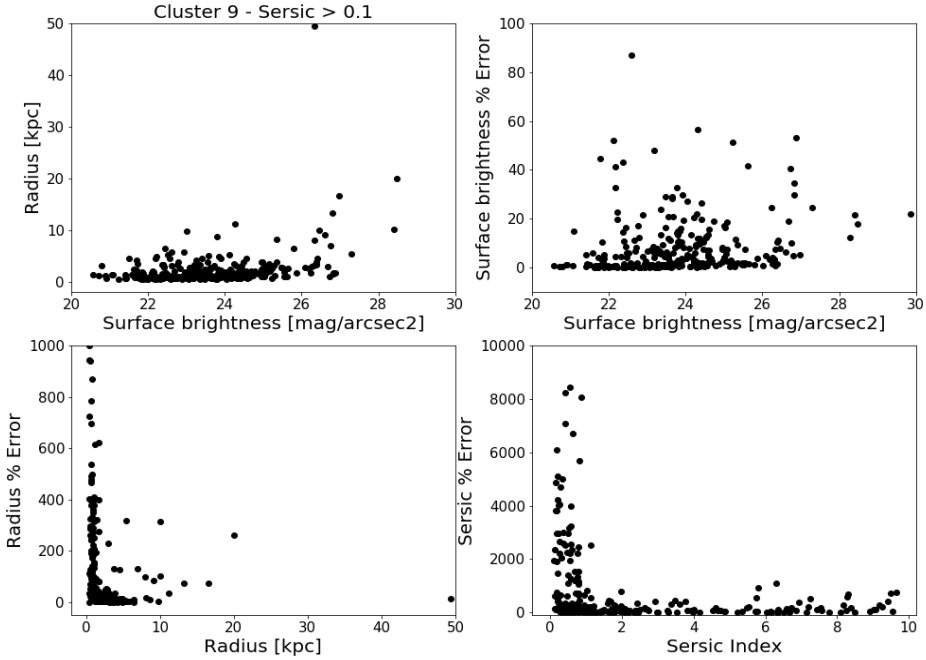

Figure 2.14: Four panel plot containing the dense region of all the sources in cluster 9 after application of the Sérsic index $n > 0.1$ cut.

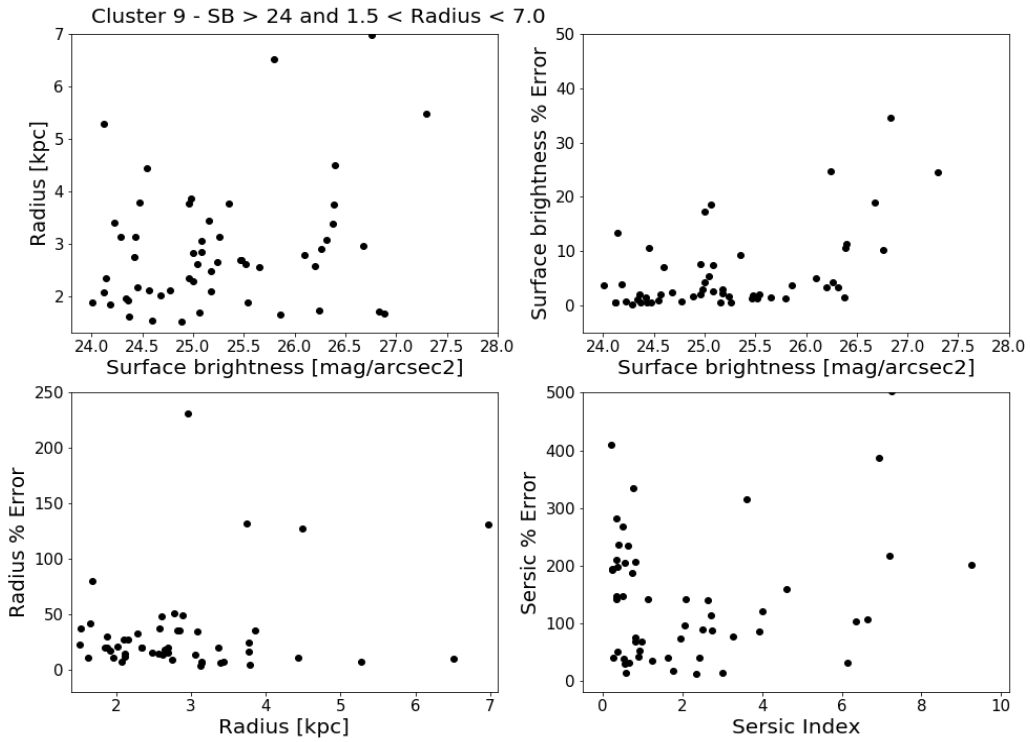

Figure 2.15: Four panel plot of all sources in cluster 9 after the applying the surface brightness ($\mu_e(g) \gtrsim 24\,\mathrm{mag/arcsec^2}$) and radius ($1.5\,\mathrm{kpc} \lesssim r_e \lesssim 7.0\,\mathrm{kpc}$) criteria.

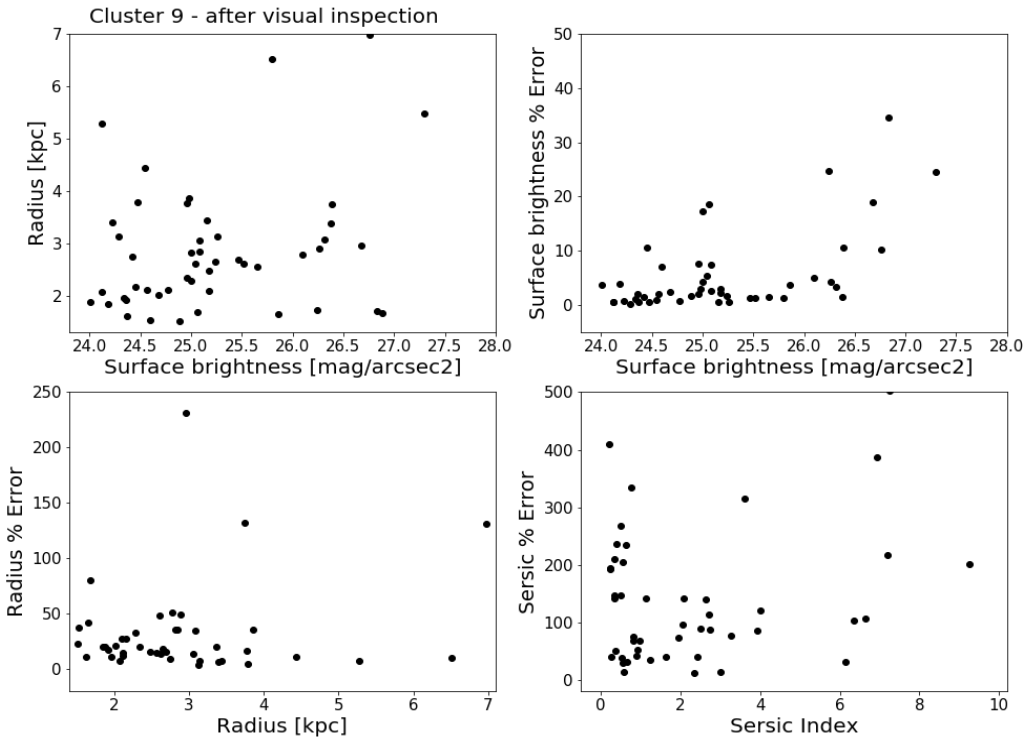

Figure 2.16: Four panel plot of all sources in cluster 9 modelled after visually inspecting all UDG candidates and removing all poorly modelled galaxies. The complete sample of all the clusters is shown in Appendix 5.2.

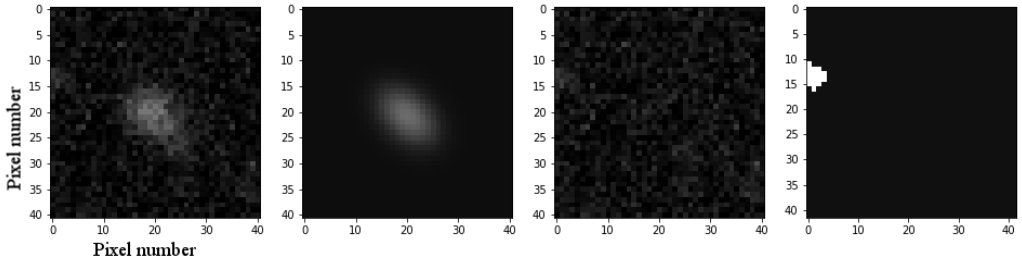

Figure 2.17: Example GALFIT output for a source with large radius in cluster 9. The 1st panel displays a cutout of the galaxy. The second is the model produced by GALFIT. The residual image is displayed in panel 3, the model subtracted from the cutout image. The 4th panel displays the mask used to remove sources not associated to the galaxy. (Model properties: $\mu_e(g) \sim 24.56\,\mathrm{mag/arcsec^2}$ and $r_e \sim 4.48\,\mathrm{kpc}$)

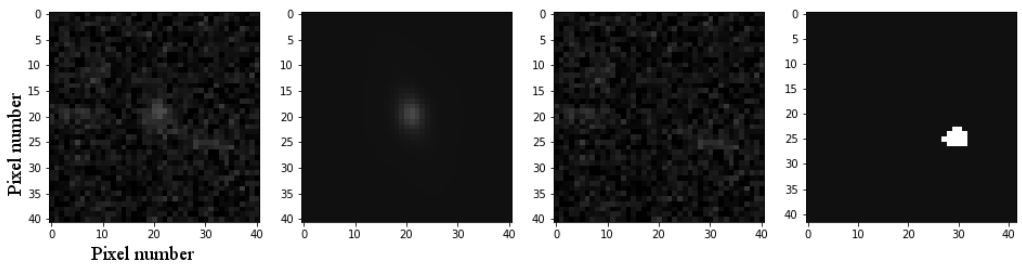

Figure 2.18: Example GALFIT output for a source with small radius in cluster 9. The 1st panel displays a cutout of the galaxy. The second is the model produced by GALFIT. The residual image is displayed in panel 3, the model subtracted from the cutout image. The 4th panel displays the mask used to remove sources not associated to the galaxy. (Model properties: $\mu_e(g) \sim 24.02\,\mathrm{mag/arcsec^2}$ and $r_e \sim 1.87\,\mathrm{kpc}$)

No	ID	N_{VR}	N_{g-r}	N_*	N_S	N_{sc}	N_{VI}
1	4873	2292	665	495	404	98	77
2	8897	2994	649	449	377	76	61
3	3198	2782	716	518	424	122	83
4	4645	2640	716	524	448	98	77
5	8361	2456	534	390	333	73	39
6	2688	2446	605	434	378	87	55
7	8751	1696	423	316	265	78	61
8	5001	2238	468	338	277	55	48
9	5202	1749	376	298	248	51	48
10	15150	1938	407	287	236	58	42
11	752	3183	869	598	515	142	111
12	2979	2010	443	330	274	53	38
13	2098	2238	544	406	354	96	65
14	3964	2008	571	417	354	96	62
15	14226	1528	317	238	192	59	33
16	9086	1295	307	224	194	53	44

Table 2.4: The effect of each step along the UDG candidate selection algorithm is displayed in this table. The numbers shown indicate the remaining UDG candidates after each criteria and limit is applied. N_{VR} = r_{200m} radius, N_{g-r} = colour cut, N_* = successful GALFIT convergence, N_S = Sérsic index greater than 0.1, N_{sc} = UDG candidate selection criteria ($\mu_e(g) \gtrsim 24\,\mathrm{mag/arcsec^2}$ and $1.5\,\mathrm{kpc} \lesssim r_e \lesssim 7.0\,\mathrm{kpc}$), N_{VI} = visual inspection.

2.2.6 Coverage Correction

The clusters examined in my sample cover large areas in Stripe 82, some of them extending beyond the limits of the IAC Stripe 82 legacy project. The gaps resulting from non-total coverage require a correction to the total number of UDG candidates and their distributions. This allows us to statistically compare the candidate numbers and distributions in each cluster to the others. As an example, I show cluster 13 in Figure 2.19. This cluster extends past the declination limit of the data. I use a circular aperture given by the r_{200m} radius, which is shown by the blue circle, for the selection of galaxies. The green dots identify all IAC sources. We use the full source catalogue to help identify where there is no coverage. Another failure in the detection of sources in the IAC project can be seen in cluster 6 (Figure 2.20). Clearly there are sources in the image in the red box, however no detections are catalogued in this part of the cluster. The reason for this failure has not been stated, but only occurs in this particular image. The existence of sources in this region can be seen, therefore we make an identical correction as stated above for non-total coverage. This is done by calculating the average UDG candidate density in the full coverage region and applying this to the missing region. Appendix 5.3 shows an example of the calculation method used for cluster 13 (Figure 2.19).

Some smaller regions of the cluster are obscured by foreground sources. However these are distributed randomly throughout every image and they have a minimal effect on the UDG candidate number count for each cluster. These foreground sources have a similar effect for every cluster. Therefore I do not correct for foreground sources obstructing the detection of UDG candidates in any of the clusters.

There are 4 clusters which have missing regions, the missing area as a fraction of their total area ('area frac'), are shown in Table 2.5. Assuming the UDG candidate number density is the same in the missing area as for the rest of the cluster, I calculate the number of candidates expected to be missing for each cluster and add it to the total. The correction term added, 'corr', is also displayed in Table 2.5 along with the number of candidates after correction, N_{corr}. We have assumed a constant uniform UDG candidate number density, however the distribution may in fact be decreasing or increasing from the centre. Either scenario is plausible; galaxy density tends to decrease further from the centre of clusters, however UDGs are thought to be more abundant in the outer regions, therefore the UDG candidate density may increase (van Dokkum et al., 2015).

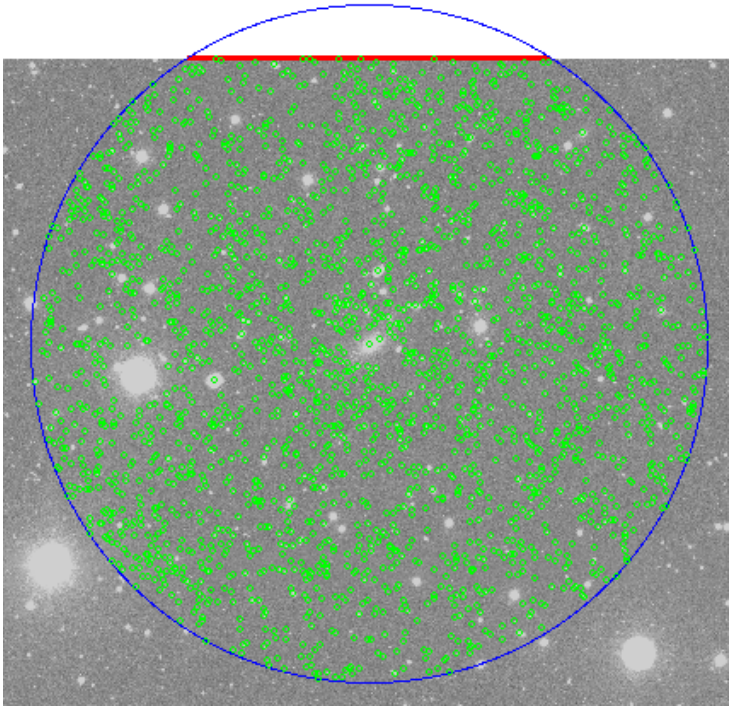

Figure 2.19: SDSS image of cluster 13. The blue circle shows the r_{200m} radius of the cluster. The green circles identify all the catalogued IAC sources in the r_{200m} radius of the cluster. The red line shows the limit of the IAC Legacy project data.

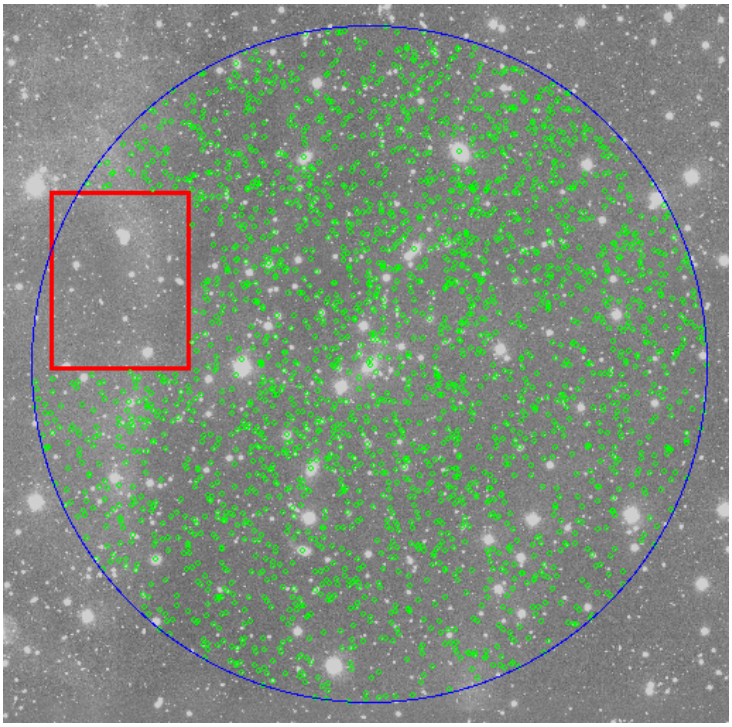

Figure 2.20: SDSS image of cluster 6. The blue circle shows the r_{200m} radius of the cluster. The green circles identify all the catalogued IAC sources in the r_{200m} radius of the cluster. The red box shows the region of missing sources in the IAC Legacy project catalogue.

No	ID	N($cl\ mem$)	area [deg^2]	area frac	corr	N$_{corr}$
1	4873	77	0.090	0.159	12.26	89.26
2	8897	61	0.081	-	-	61
3	3198	83	0.110	0.206	17.13	100.13
4	4645	77	0.074	-	-	77
5	8361	39	0.063	-	-	39
6	2688	55	0.083	0.068	3.75	58.75
7	8751	61	0.060	-	-	61
8	5001	48	0.053	-	-	48
9	5202	48	0.054	-	-	48
10	15150	42	0.044	-	-	42
11	752	111	0.094	-	-	111
12	2979	38	0.060	-	-	38
13	2098	65	0.058	0.038	2.46	67.46
14	3964	62	0.060	-	-	62
15	14226	34	0.036	-	-	33
16	9086	44	0.040	-	-	44

Table 2.5: The UDG candidate numbers are displayed along with their updated values as we correct for the missing regions. The number of UDG candidates in shown in column N$_{cl\ mem}$. Total circular area covered by the cluster is shown in column named 'area'. The correction values added to each cluster which accounts for missing regions are shown. Only 4 clusters have missing regions. The fraction of the missing area compared to the clusters area are calculated in the 'Area frac' column. The correction term added is displayed in the column 'corr' alongside the updated number of UDG candidates, N$_{corr}$.

2.2.7 Background Correction

The main source for contamination of our sample of UDG candidates arises from foreground and background sources (hereafter referred to as background sources) passing the initial colour cut. The properties of the sources passing this colour cut are determined and modelled based on the assumption that they are at the cluster's redshift. To account for this inclusion of background sources we attempt to determine the average distribution of non-UDG candidate sources which fall within the colour cut. I then directly remove this number density from the number density of UDG candidates within our clusters.

We selected 5 random IAC Stripe 82 images, which were near the same areas of our clusters. The density of sources fluctuate significantly throughout the images and restricting potential image regions to near our clusters will provide a better measure of the background densities. The images were examined using the RedMaPPer cluster catalogue to locate clusters in the images. These images were only scrutinized with one criterion in mind; no cluster should be in the central regions of the images. This will allow us to determine a background density rather than the density of UDG candidate-like sources in another cluster. Images with clusters near the edges were included as their number densities are expected to have a minimal effect when averaged over the whole image's area. The 5 images selected are displayed in Figures 2.21 to 2.25.

To identify sources in the field which are similar to the sources we identified in our cluster, I proceeded to perform a 'general' $g-r$ colour cut on all the images. The red sequence of all the clusters were used to determine the minimum and maximum colour limits of the background sample. Figure 2.26 displays this limit applied to background image f0461. To be inclusive we used $\Delta(g-r) = 0.35$ mags, 0.05 mags broader than the UDG candidate colour cut used for our clusters. The minimum and maximum $g-r$ colours were identified within the r-band range, 15 mags $<$ r$_{band}$ $<$ 26 mags. The maximum and minimum $g-r$ colours were then used universally throughout the images to extract sources. GALFIT was then run on all these sources. The $g-r$ red sequence colour cut for each cluster was then applied, as described in Section 2.2.3. The method for determining the number of background sources is identical to that of the UDG candidates, detailed in sections 2.2.4 and 2.2.5. Independent visual inspection of all the

No	ID	N_{corr}	BG_{avg}	BG_{std}	BG_{tot}	N_{UDG}
1	4873	89.26	49.85	7.84	72.0	17.3
2	8897	61	45.60	7.81	59.0	2.0
3	3198	100.13	46.45	7.28	82.0	18.0
4	4645	77	47.45	7.28	55.8	21.2
5	8361	39	41.00	7.66	41.5	-2.5
6	2688	58.75	45.35	7.21	60.4	-1.7
7	8751	61	47.05	7.61	45.1	15.9
8	5001	48	45.40	7.38	38.2	9.8
9	5202	48	42.55	7.63	36.7	11.3
10	15150	42	40.75	7.65	28.6	13.4
11	752	111	45.95	7.12	69.3	41.7
12	2979	38	37.90	7.21	36.3	1.7
13	2098	67.46	44.85	7.53	41.3	26.1
14	3964	62	44.90	7.52	42.7	19.3
15	14226	33	33.70	6.75	19.5	13.5
16	9086	44	41.95	7.86	27.0	17.0

Table 2.6: The number of UDG candidates after coverage correction, N_{corr}. The average number of background counts in each $0.0625\,\mathrm{deg}^2$ area corresponding to the respective cluster's red sequence cuts, BG_{avg}. The standard deviation with respect to the average number of background sources are shown in column BG_{std}. The total background sources in the area of each respective cluster is displayed in the column BG_{tot}. N_{UDG} is the resulting total number of UDG candidates in each cluster after subtracting the background counts.

background sources was performed in the same way as for the UDG candidates (Section 2.2.5). Poorly modelled sources due to complex extended structure, nearby contamination, off-centering, bad residuals or extreme faintness were removed.

The background for each cluster is determined separately using the cluster's respective red sequence to get different background sub-samples for each cluster. This is done by performing the $\Delta(g-r) = 0.3$ mags red sequence colour cut for each cluster on the background sample. In order to quantify the variation of the background source counts in different regions of the background fields, we divide the background images into quarters and count the number of UDG candidates in each quarter. The size of each quarter is $area = 0.0625\,\mathrm{deg}^2$, which is similar to the scale of the clusters (displayed in column 'area' in Table 2.5). Table 2.6 displays the average number of background sources over all 20 background sub-regions for each cluster. The average number of background sources range from 33.70 to 49.85 for the different red sequence colour cuts. The standard deviation of the number of background sources for each cluster image was then calculated, shown in column 'BG_{std}'. The average standard deviation for all 16 clusters is 7.46 sources in a $0.0625\,\mathrm{deg}^2$ area.

Finally we remove the background sources from our sample of UDG candidates as follows. The number of background sources per deg^2 was scaled to the size of each cluster (displayed in column 'BG_{tot}' of Table 2.6). We directly find the number of UDG candidates in each cluster (column 'N_{UDG}' in Table 2.6) by subtracting the background sources ('BG_{tot}') from the current UDG candidate sample ('N_{corr}'). The resulting numbers of candidates in each cluster are mostly positive and above the standard deviation determined for the quarter image area. However, at least 2 clusters are consistent with having zero UDG candidates. This may suggest there are fewer UDG candidates in these clusters than UDG candidate-like sources in the background.

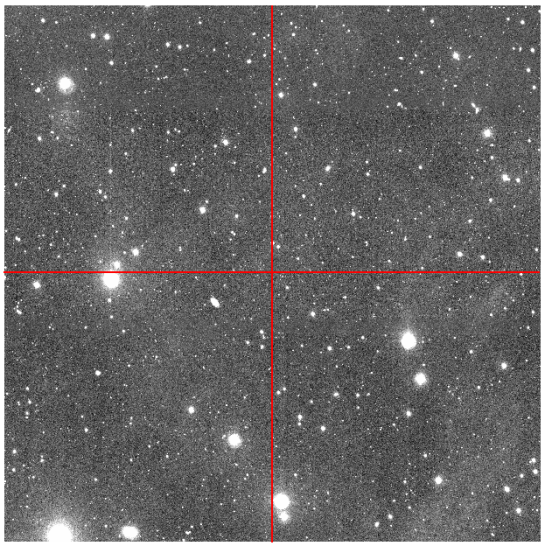

Figure 2.21: Background image f0461.

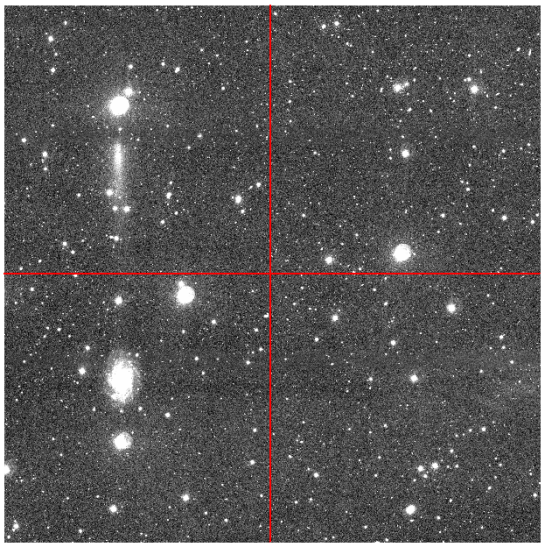

Figure 2.22: Background image f0614.

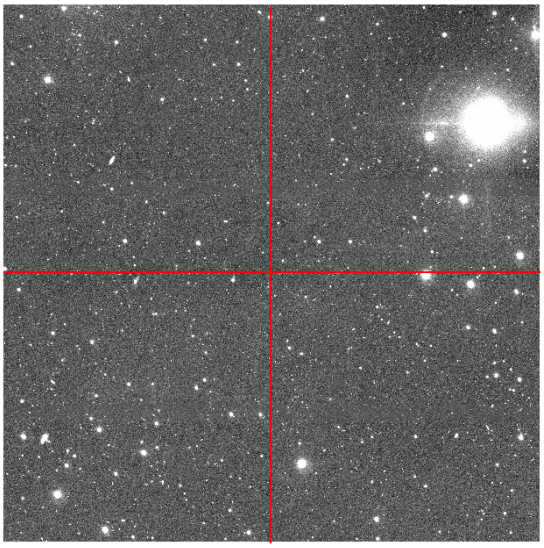

Figure 2.23: Background image f1012.

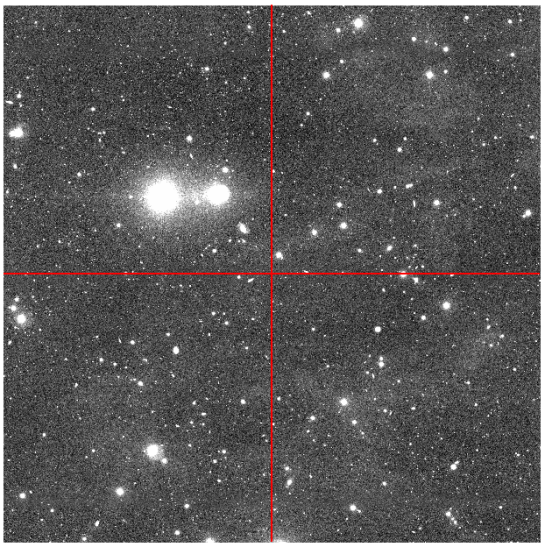

Figure 2.24: Background image f1053.

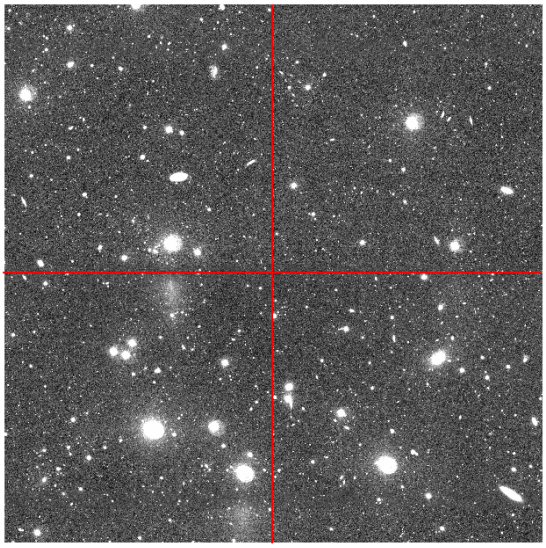

Figure 2.25: Background image f1413.

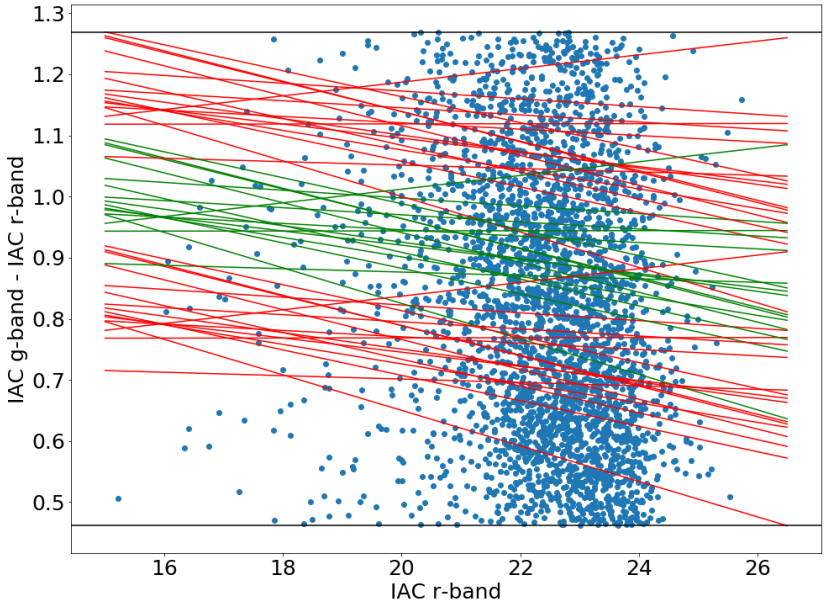

Figure 2.26: The 'broad' red sequence is displayed. The IAC sources within image f0461 are shown in blue. The green lines identify all the red sequences of every cluster in our sample. The red lines indicate both the maximum and minimum red sequences which comfortably includes all sources to be considered for background correction. The black lines identify the maximum and minimum $g-r$ colours, $g-r\ \sim 1.27$ and $g-r\ \sim 0.46$ respectively for all the clusters combined.

Chapter 3

Results

In this chapter we explore and analyze the properties of our UDG candidates. In the first section we compare the properties of the UDG candidates in their respective clusters before applying the background subtraction. Next, we investigate the UDG candidate's properties after applying the background subtraction. The candidates are combined into a single overall UDG candidate sample in this section. This increases our sample size and we are able to determine average properties from a larger sample. The redshift range of our clusters is quite small, $0.09 < z < 0.15$, therefore any evolutionary effects are likely to be small.

3.1 UDG Properties Before Background Subtraction

3.1.1 Spatial Distribution

The spatial distribution of UDGs in the cluster is a very important property beacause if UDGs are found at specific radius ranges or certain regions of the cluster, it may imply the environment in these areas is ideal for UDG existence. One caveat is that the spatial distribution is only 2-dimensional, which results from the lack of redshift information for faint galaxies in these clusters. We use the red sequence to identify candidates with a highly probable cluster association and assume they have the redshift of the cluster. Therefore, UDG candidates which appear near the cluster centre may in fact be further from the centre along the line of sight.

The spatial distributions of UDG candidates in our sample are shown by the blue dots in Figures 3.1, 3.2 and 3.3. The purple shaded regions identify regions where there are gaps in the IAC data, the RedMaPPer galaxies (red dots) are still identified in these areas. The RedMaPPer galaxies display a slight overall overdensity in the central region, with a considerably more sparse distribution in Cluster 10 and 15. However, the UDG candidates have a scattered distribution from the centre to the outskirts. They cover both regions with and without RedMaPPer galaxies, as well as not being detected in some regions where RedMaPPer galaxies are found. UDG candidates are also observed in the central regions of the clusters, keeping in mind the lack of line-of-sight distance measurements. Van Dokkum et al. (2015) found that the UDGs in Coma were located further than 300 kpc from the centre and speculated that UDGs cannot exist within 300 kpc from the cluster centre. Clusters have strong tidal fields, therefore existence in the central regions is not expected. However, even in our richest cluster, Cluster 11 ($\lambda = 56.78$), we find UDG candidates near the cluster centre. Koda et al. (2015) and Román & Trujillo (2017b) report UDGs closer to the cluster's centres than previous works, however the immediate centre had no UDGs. A few of the clusters have gaps in the UDG distribution near the cluster's centres (cluster 2, 7, 9, 10, 15, 16). However, this is not consistent throughout, therefore we cannot presume any regions in the cluster are preferred or avoided by UDG candidates.

3.1.2 Galaxy Radius

A main feature of UDGs are their extended sizes, which is one of the main criteria set by van Dokkum et al. (2015) for identifying UDGs; $r_e \gtrsim 1.5$ kpc. The effective radius we use is determined by GALFIT (Peng et al., 2002) to be the radius in which half the galaxies total flux is contained. Here we analyze the effective radius distributions of our UDG candidates.

Figures 3.4 and 3.5 display the UDG radius distribution in each cluster. These histograms have a 0.5 kpc binning between 1.5 and 7.0 kpc. In the figures we see that for all the clusters the number of

UDG candidates peaks at low radii ($\sim 2\,\mathrm{kpc}$) and decreases towards the higher radii. Galaxies have a wide range of sizes and are generally more numerous and easier to detect at lower radii, which can be observed in these plots. We also find at the lowest redshifts that the slopes of the radius distributions are steeper than the slopes of the highest redshift clusters, e.g. Cluster 1 radius distribution is much steeper than that of Cluster 16. This shows that we detect fewer low radii UDG candidates at high redshifts than at lower redshifts. This may be a selection effect (see Section 3.1.5 and Figure 3.10). We detect fainter dwarf galaxies in low redshift clusters compared to higher redshift clusters. Therefore, we find more low radii candidates in low redshift clusters than the higher redshift clusters.

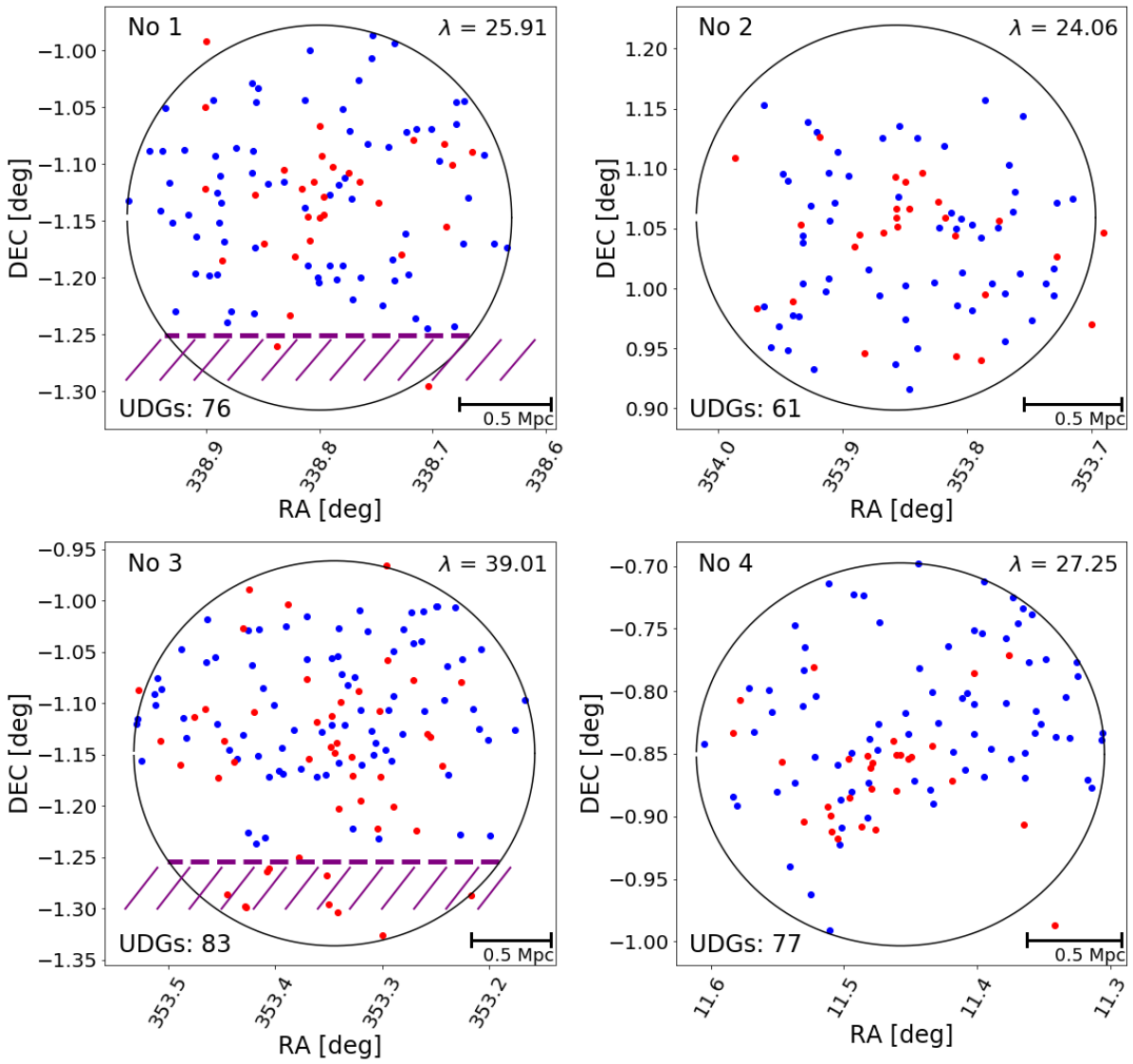

Figure 3.1: Spatial distribution of UDG candidates inside the r_{200m} radius of each cluster. Clusters 1-4 are displayed here, clusters 5-16 are shown on the following pages. The large black circles identify the r_{200m} radius, blue dots mark the positions of UDG candidates and the red dots identify the RedMaPPer galaxies. The purple lines and boxes identify regions where there are gaps in the data; these identifiers were used to estimate the number of missing UDG candidates, as described in Section 2.2.6.

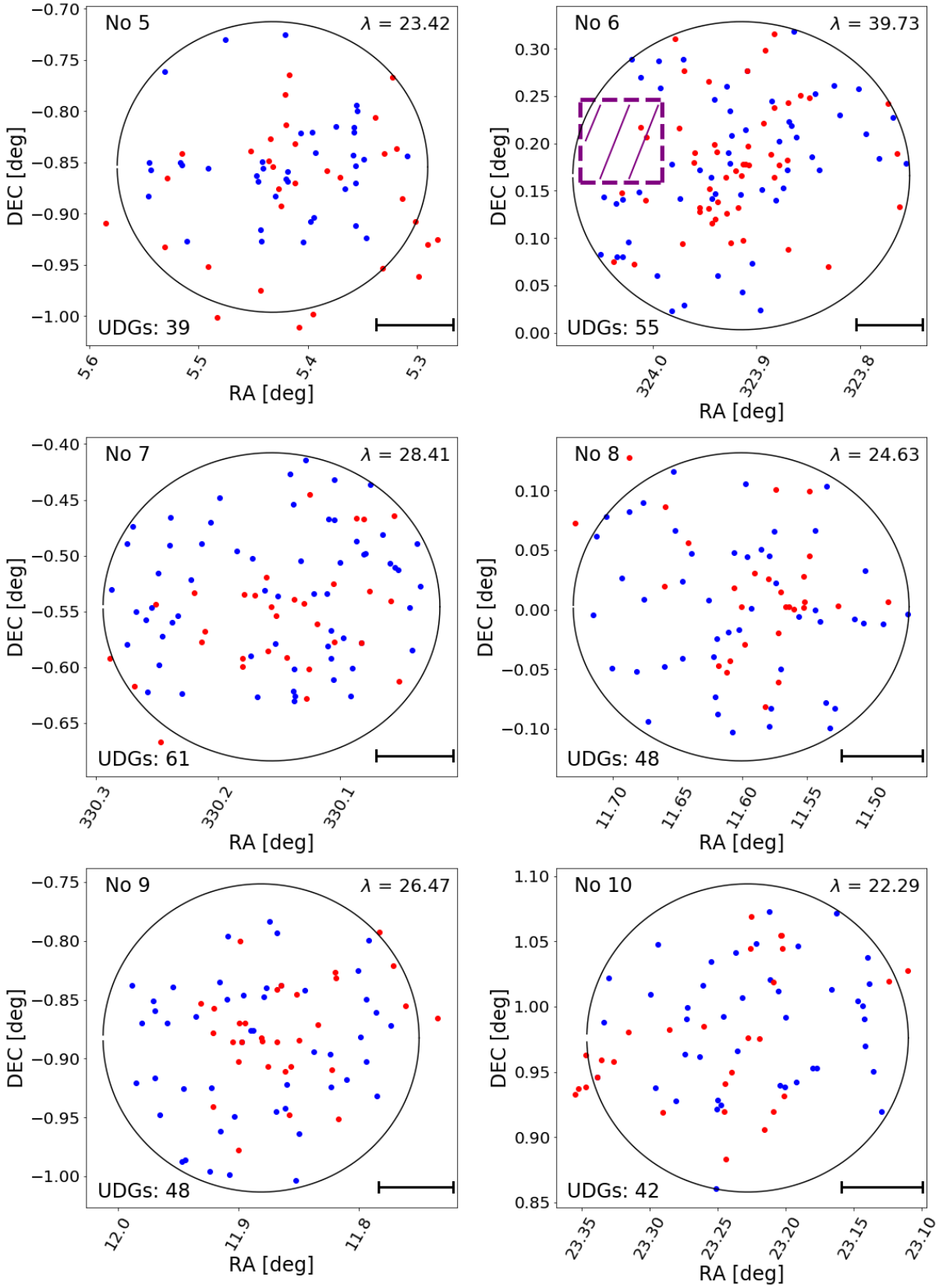

Figure 3.2: (Continued) Spatial distribution of UDG candidates inside the r_{200m} radius of each cluster. Clusters 5-10 are displayed here.

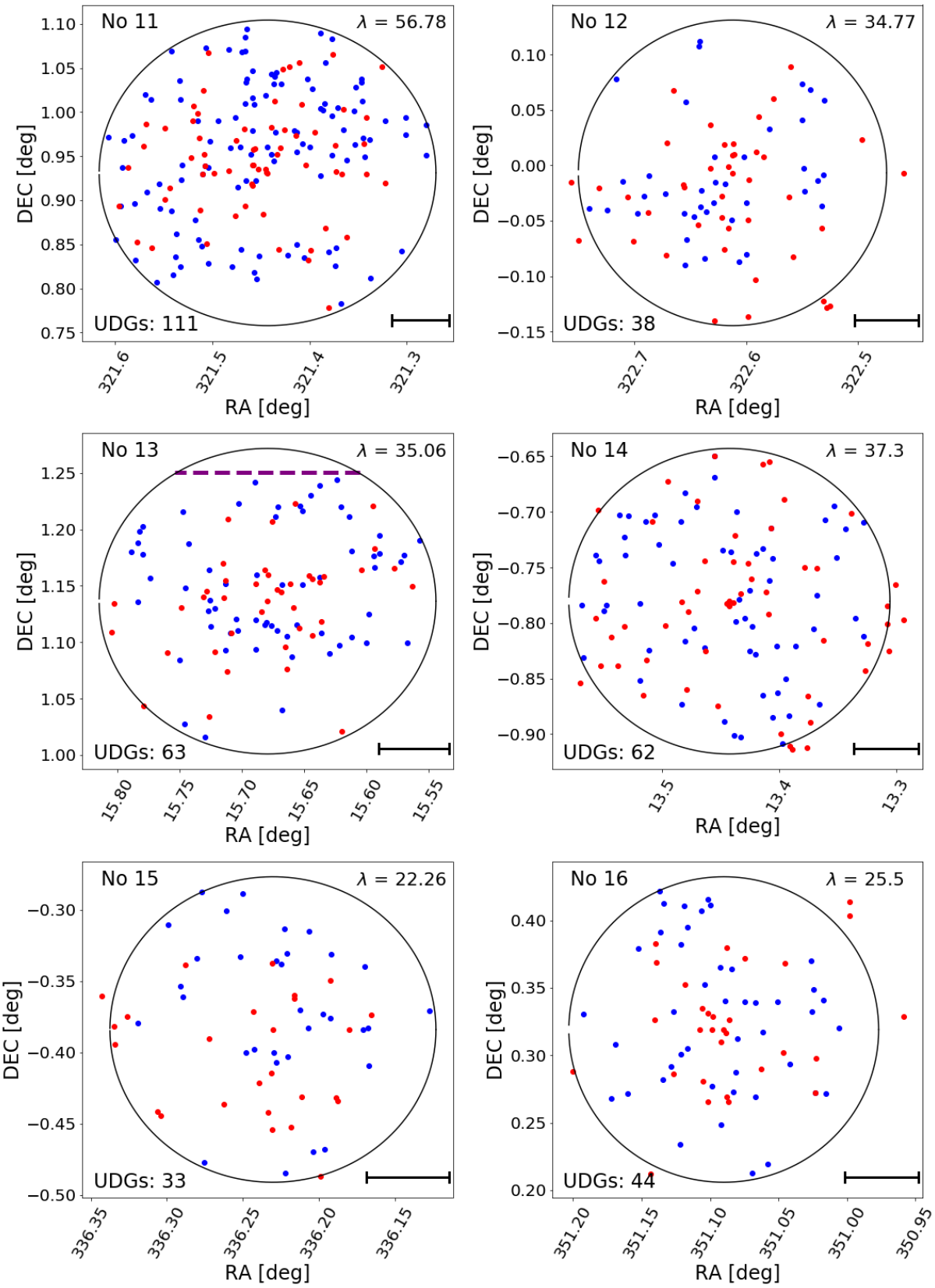

Figure 3.3: (Continued) Spatial distribution of UDG candidates inside the r_{200m} radius of each cluster. Clusters 11-16 are displayed here.

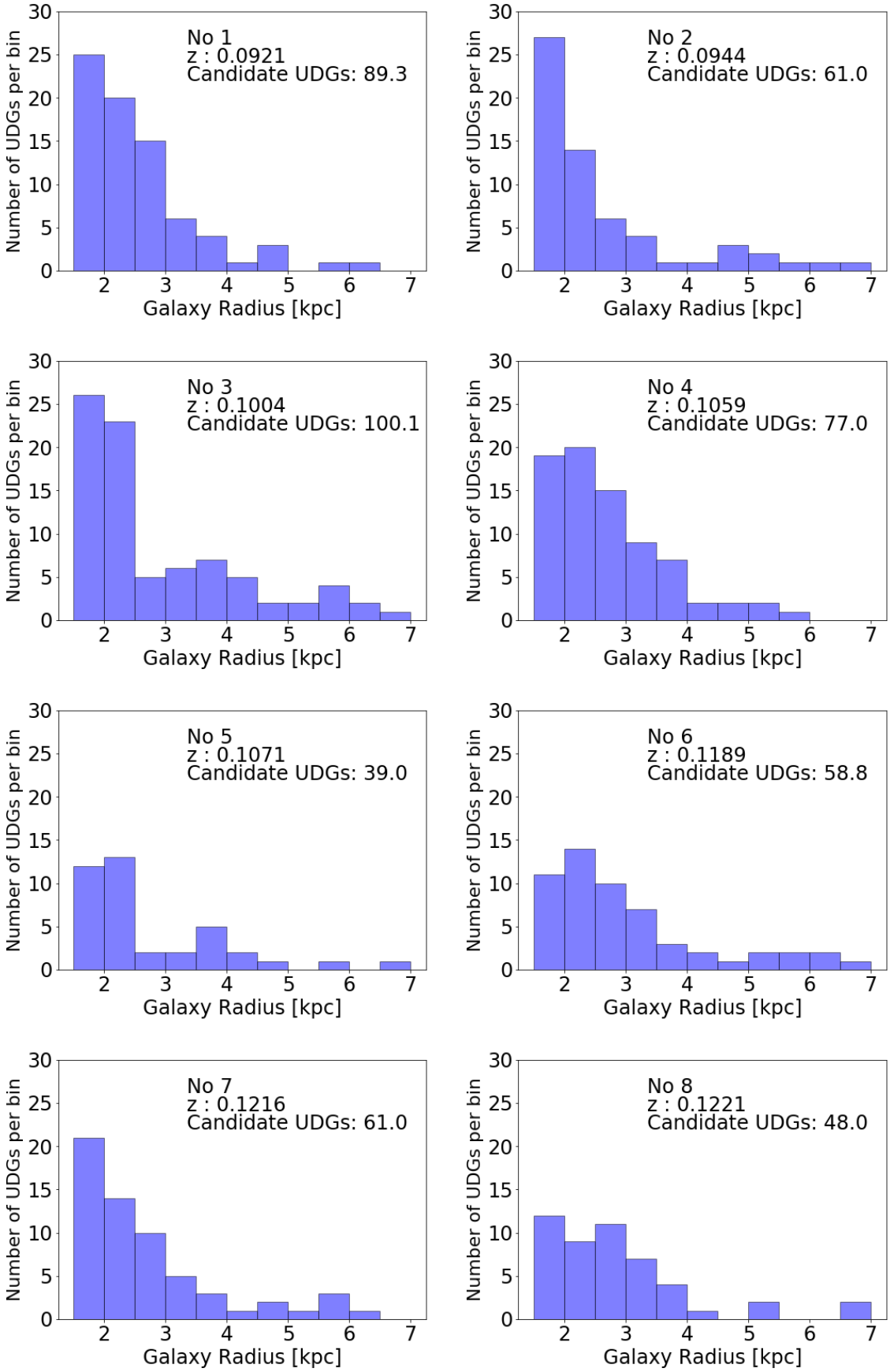

Figure 3.4: Histograms of the effective radii of UDG candidates in clusters 1-8.

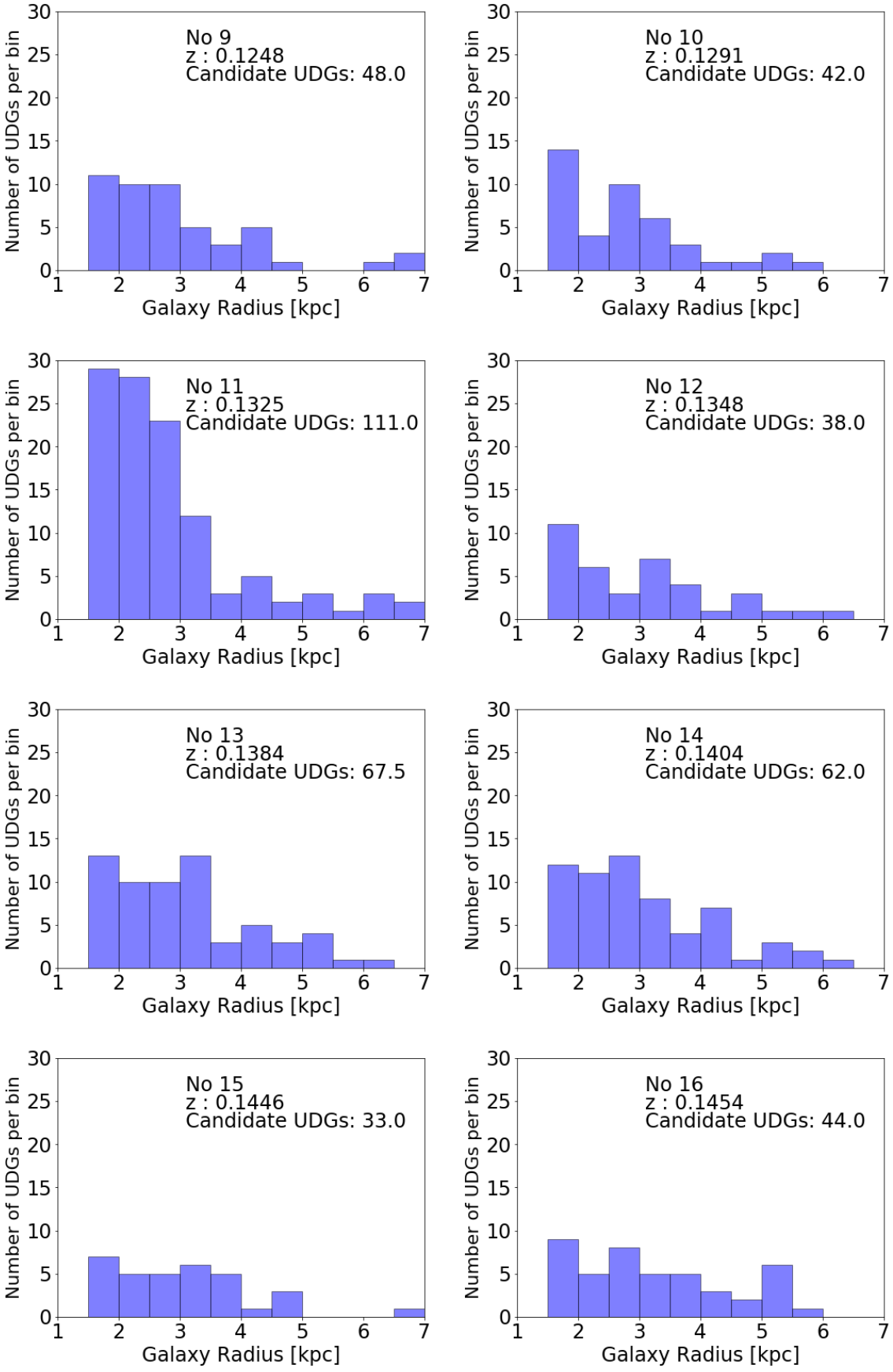

Figure 3.5: (Continued) Histograms of the effective radii of UDG candidates in clusters 9-16.

3.1.3 Galaxy Surface Brightness

The surface brightness is another main criterion which distinguishes UDGs from other galaxies. Our surface brightness cut requires sources to have an effective surface brightness $\mu_e(g) \gtrsim 24\,\mathrm{mag/arcsec^2}$.

Figures 3.6 and 3.7 display the surface brightness distributions for our sample of 16 clusters. These histograms show that our UDG candidates are generally more numerous at brighter surface brightness and there are fewer at fainter surface brightness. Brighter sources are much more easily detectable. The central part of the cluster usually has higher background levels due to intra cluster light and the halos of bright galaxies, making it difficult to observe faint sources around the centre of the cluster. Furthermore, observational limits also restrict the detection of faint sources. The data we use from the Stripe 82 Legacy project has a 50% effective surface brightness completeness limit of $26\,\mathrm{mag/arcsec^2}$ in the g-band. The simulations performed by van der Burg et al. (2016) show that detectability of sources depends on both size and surface brightness. Subsequently, we expect the number of sources above the 50% completeness limit to be lower than the total UDG counts in the clusters. The larger number of UDG candidates observed at the brighter surface brightness end of these plots are expected when taking these factors into account.

3.1.4 Galaxy Sérsic Index

The Sérsic indices of UDGs describes the light profile, as described in Section 2.2.4. Several papers report that UDGs have mean Sérsic indices, $n \sim 1$, as detailed in Section 1.3.1. These including Lee et al. (2017) on the massive Abell 2744 (z=0.348) and Abell S1063 (z=0.308) galaxy clusters, with average UDG Sérsic indices of $n \sim 1.14$ and $n \sim 0.94$ respectively. The lower redshift clusters of Fornax (z=0.005) and Virgo (z=0.003) have similar values, $n \sim 1.07$ and $n \sim 0.90$ respectively (Muñoz et al. 2015, Mihos et al. 2015).

Figures 3.8 and 3.9 display the Sérsic index distribution for our 16 clusters. The binning of these histograms has been chosen to be centered on integer values, spanning from 0 to 10 with a bin size of 1. The minimum value is set by the cut of $n > 0.1$ (Section 2.2.5), and the upper limit is the default set by GALFIT (Peng et al., 2002). All of the clusters show a large number of sources with exponential light profiles, with the median Sérsic index over all 16 clusters n = 1.28. These figures agree with the previously found values (Table 1.1 in Section 1.3.1 of the introduction) and indicate our UDG candidates have light profiles similar to previously found UDGs. Moreover, our median Sérsic index agrees with both the higher redshift clusters investigated by Lee et al. (2017) and the lower redshift clusters investigated by Mihos et al. (2015) and Muñoz et al. (2015). The average Sérsic indices of the UDGs in Coma, Abell 168, AS1063 and A2744 and their respective are plotted in Figure 1.5. The median Sérsic index of our sample of UDGs in Stripe 82 and their distribution is consistent with the indices found in these surveys. We only observe a small number of candidates with larger Sérsic indices, which is representative of a steeper light profile (Kormendy, 1977). Our sample may be brighter than the typical UDGs, however, their light profiles are still quite similar. This agrees with the sentiment that UDGs are not unique galaxies, they are simply the largest and faintest galaxies that have been observed in clusters (van Dokkum et al., 2015). Furthermore, this suggests a continuum of galaxy properties between bright galaxies and dwarfs in clusters.

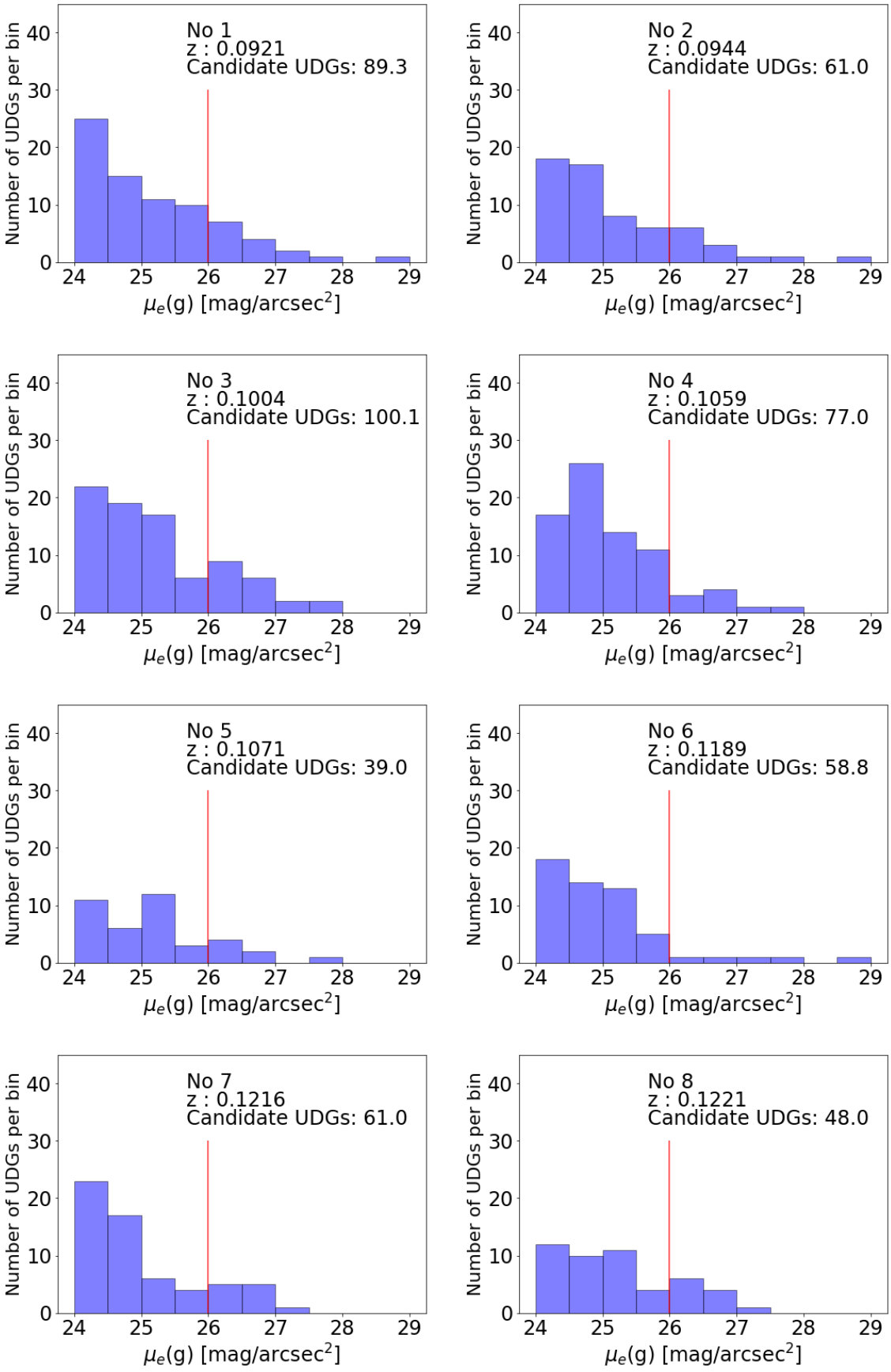

Figure 3.6: Histograms of the effective surface brightness in the g-band for UDG candidates in clusters 1-8. The 50% completeness limit $\mu_e(g) = 26\,\mathrm{mag/arcsec^2}$ is indicated by the red vertical lines. Clusters 9-16 follow on the next page.

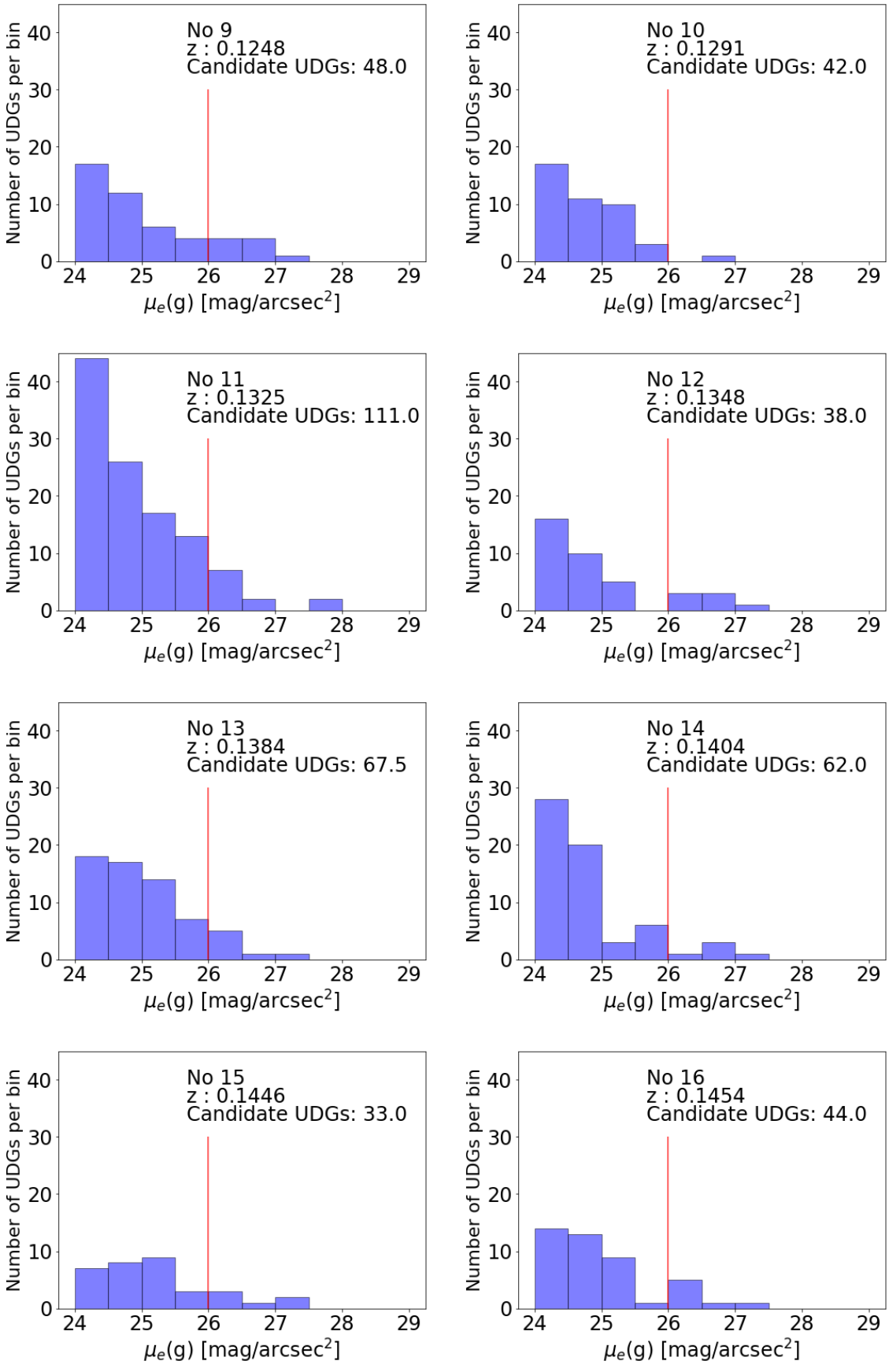

Figure 3.7: (Continued) Histograms of the effective surface brightness in the g-band for UDG candidates in clusters 9-16.

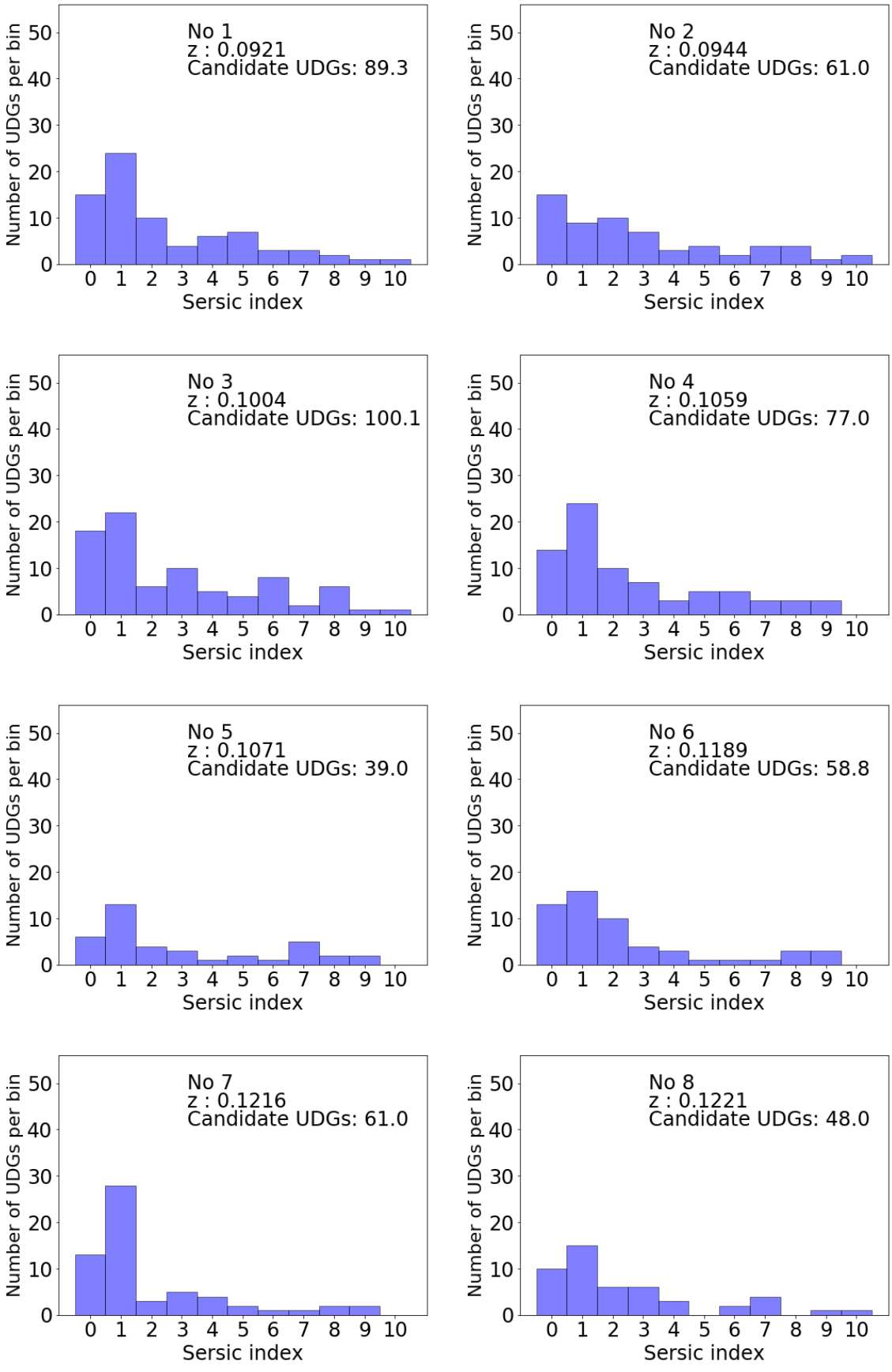

Figure 3.8: Histograms of the Sérsic indices of UDG candidates in clusters 1-8. Clusters 9-16 follow on the next page.

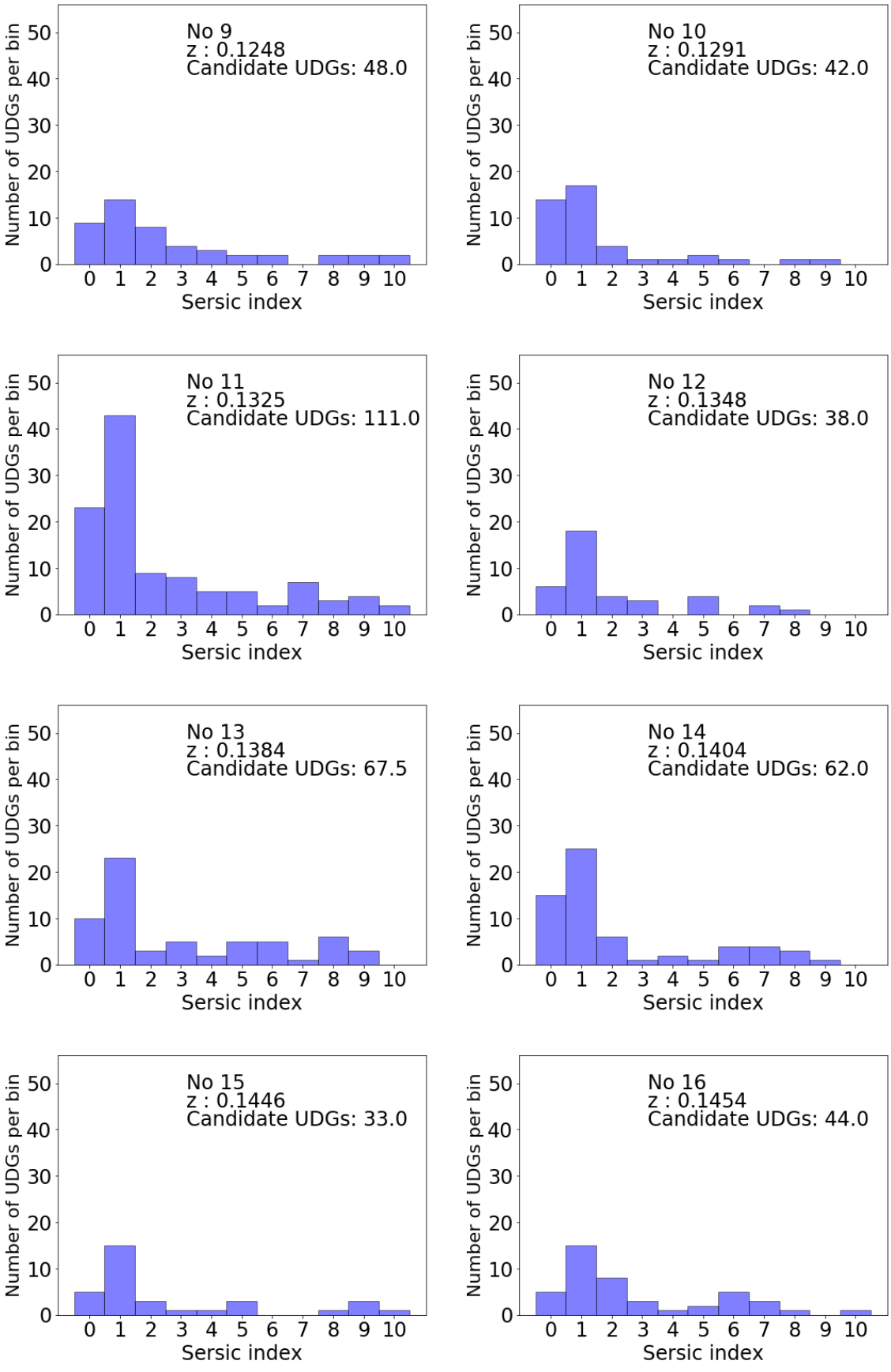

Figure 3.9: (Continued) Histograms of the Sérsic indices of UDG candidates in clusters 9-16.

3.1.5 Faint Galaxy Properties as a Function of Redshift

The evolution of UDGs can be studied by investigating their properties and how they change at different redshifts. The properties of the UDG candidates in our 16 clusters are shown altogether in Figure 3.10, where the colour of each point indicates the redshift of the cluster. The top-left panel shows the data from the 16 clusters in our sample. This plot compares the galaxies' radii and surface brightness values, as we expect all the data in each cluster lies in the same region with similar number densities. The density of sources increases toward the bottom-left of the plot, which is expected as brighter sources are more easily detected and smaller sources are more numerous. The top-right panel shows the radius as a function of axis ratio. Previous research, displayed in Table 1.1 (Section 1.3.1), consistently shows a preference toward an axis ratio <b/a>$\sim$ 0.7. Our UDG candidate distribution in axis ratio is spread near-evenly, from highly elongated sources at small values to circular sources with an axis ratio of b/a ~ 1. The average axis ratio of our candidates are <b/a>$= 0.52$, contrary to the reported <b/a>$\sim$ 0.7 in previous research. The published axis ratio distributions of Abell 168 and its surrounding regions (Román & Trujillo, 2017a) and the Coma cluster (van Dokkum et al. 2015; Koda et al. 2015; Yagi et al. 2016) distributions are all concentrated around the <b/a>$\sim$ 0.7 average.

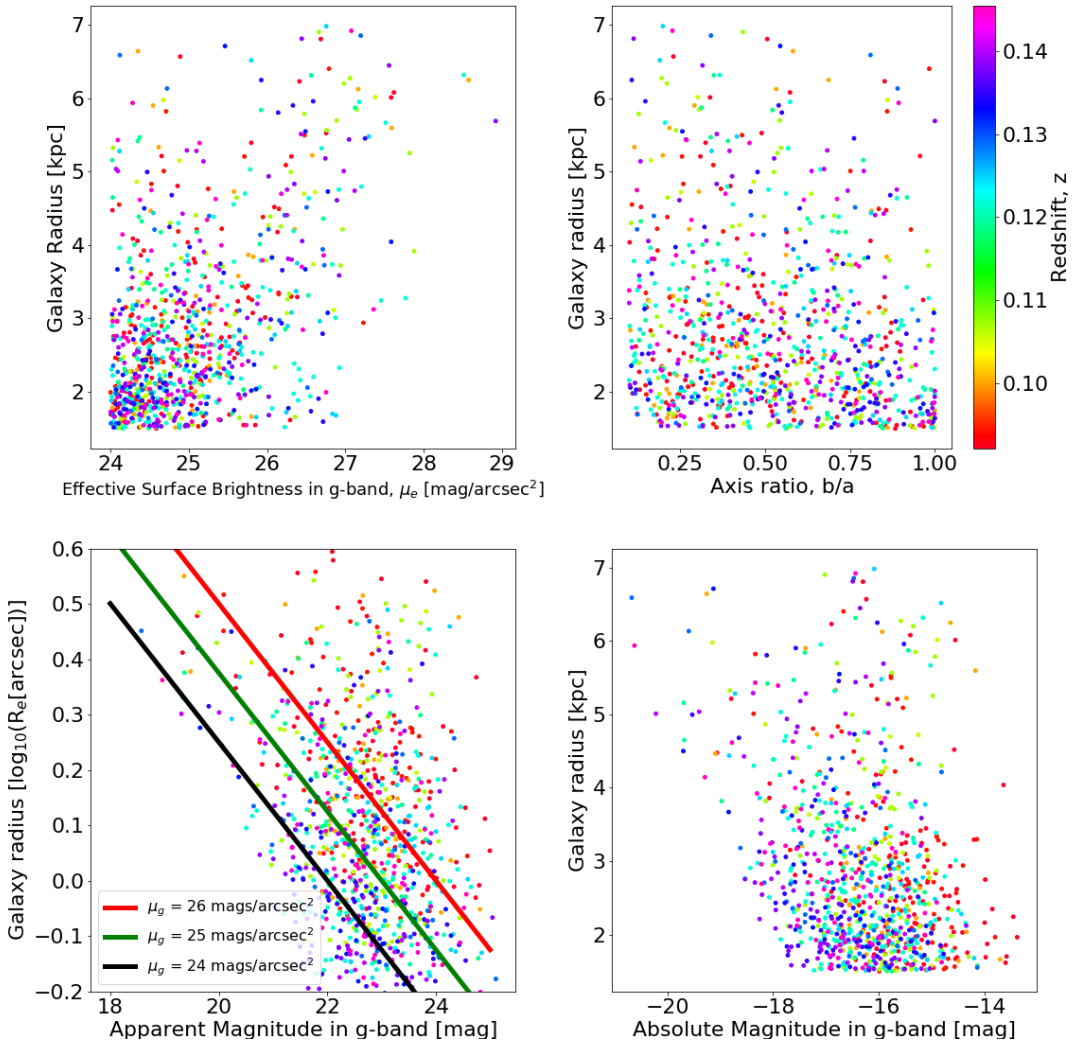

Figure 3.10: The top-left panel displays the galaxies radius vs. effective surface brightness in the g-band for all the candidate UDGs in every cluster before background subtraction. The top-right panel displays the galaxies radius vs. axis ratio. The bottom-left panel displays the galaxies' radii vs. apparent magnitude. Lines indicating the equal effective surface brightness of 24, 25 and 26 mag/arcsec^2 for sources with exponential profiles are shown in black, green and red respectively. The bottom-right panel displays the candidate UDGs radius vs. k-corrected absolute magnitude.

Next, we analyzed the angular radius vs. g-band apparent magnitude in the bottom-left plot. The angular radius drops below $0.631''$, equivalent to a diameter of $1.26''$. The FWHM of the images is $1.24''$ (displayed in Table 2.2). There are 13 sources with a diameter below the FWHM, however they are only marginally smaller than the FWHM value. Lines of equal effective surface brightness of 24, 25 and 26 mag/arcsec^2 for sources with exponential profiles are shown. From the plot we see the higher redshift UDG candidates clump toward the lower angular radius. The lower redshift candidates are more spread throughout the plot, with very low numbers at the lower angular radius. The higher redshift galaxies appear smaller as they are further away, therefore they are more numerous at smaller angular radii. Many of these sources appear to have surface brightness below our $\mu_e(g) \gtrsim 24\,\mathrm{mag/arcsec^2}$ cut. However, some of the sources in our UDG sample do not have exponential profiles therefore they fall below the $24\,\mathrm{mag/arcsec^2}$ line.

The IAC legacy project reaches a 50% completeness limit in the g-band at a surface brightness of $\mu_e(g) = 26\,\mathrm{mag/arcsec^2}$. This implies that the number of observed sources with $\mu_e(g) = 26\,\mathrm{mag/arcsec^2}$ is only half of the expected total number of sources at this surface brightness. Brighter surface brightnesses have a higher completeness limit and therefore the number of observed sources approaches the expected total number of sources. Whereas, fainter surface brightnesses have lower completeness limits and a much smaller fraction of the expected total number of sources are actually observed. Therefore, the fraction of observed sources compared to expected sources decreases at fainter surface brightnesses. Furthermore, the expected number of UDG candidates in a cluster are presumed to increase as the surface brightnesses become fainter. If taking incompleteness into account, we would expect the effective surface brightness distribution not to tail off toward fainter surface brightnesses and the total number of galaxies detected to increase.

The bottom-right plot displays galaxy radius vs. k-corrected g-band absolute magnitude. Flux measurements of sources are affected by their redshifts. K-correction converts these measurements in each wavelength band to distance independent rest-wavelength values. The k-corrected absolute magnitudes were calculated using a k-correction calculator described in Chilingarian et al. (2010) and Chilingarian & Zolotukhin (2012). Clearly from the plot we can see a slight offset between the blue, high redshift points and the red low redshift points. High redshift galaxies are intrinsically brighter than low redshift galaxies of the same apparent magnitude. Therefore, in a magnitude limited survey galaxies in a higher redshift cluster will be shifted toward more negative absolute magnitudes. Subsequently, fainter dwarf galaxies are seen in the closer clusters, which is visible in the plot.

3.1.6 Comparison to Van Dokkum et al. (2015) and LSB Galaxies

The van Dokkum et al. (2015) UDG surface brightness cut ($\mu_0(g) \gtrsim 24\,\mathrm{mag/arcsec^2}$) is fainter than the cut we use ($\mu_0(g) \gtrsim 22.178\,\mathrm{mag/arcsec^2}$). Here we directly compare our UDG candidates to the van Dokkum et al. (2015) UDGs. We also compare our results after making their fainter surface brightness cut. We utilized the following equation described by Caon et al. (1993b) to convert from effective surface brightness to central surface brightness:

$$\mu_r = \mu_e + c_n\left[\left(\frac{r}{r_e}\right)^{1/n} - 1\right] \qquad , \tag{3.1}$$

where r = 0; c_n is approximated by $2.5(0.868n - 0.142)$; with $n = 1$, we adopt an exponential as it roughly matches our median Sérsic index; r_e is the effective radius.

Figure 3.11 compares our UDG candidates' properties to the van Dokkum et al. (2015) UDGs. The top-left panel compares the effective radius vs. central surface brightness, our UDGs are blue dots and the van Dokkum et al. (2015) UDGs are red outlined triangles. The vertical dotted line indicates the UDG minimum surface brightness criteria. We can see that most of our UDG candidates fall below the criteria, and are brighter than the van Dokkum et al. (2015) sources. Our candidates' radii span a larger range of values, up to 7.0 kpc, whereas the maximum van Dokkum et al. (2015) radius is only 4.6 kpc. We report a total of 941 UDG candidates before background subtraction, of which 165 pass the $\mu_0(g) \gtrsim 24\,\mathrm{mag/arcsec^2}$ criteria. Many of the UDG candidates passing this cut would survive the background subtraction as they are larger and fainter than the typical background galaxies (see Section 3.2). Indicating that our clusters have an excess of UDGs. The bottom-left panel plots the effective radius vs. UDG candidates which satisfy this cut. Comparatively our candidates are much more spread in radius and surface brightness, with more smaller and fainter recorded sources.

The top-right panel compares the axis ratio between our sample and the van Dokkum et al. (2015) UDGs. The distribution of our candidates are fairly uniform throughout with no clear overdense regions. It can be roughly seen that our smaller candidates have an axis ratio closer to ~ 1, which appears to agree with their small sources. This effect is expected, as the resolution limit is approached sources appear to be rounder and more point-like. The larger radii candidates seem to be more elongated, which can also be seen in the van Dokkum et al. (2015) UDGs.

The radius vs. k-corrected absolute magnitude is displayed in the bottom-right panel. Our candidates appear to be mostly brighter than the van Dokkum et al. (2015) UDGs. However, there is a region where quite a few of our sources overlap their UDGs. From these plots we can see that the sources we are investigating have very similar properties to UDGs, in fact many have identical properties. We can clearly see from this plot and Figure 3.10 that UDGs are an extension of the galaxy population, which identifies the faintest and most diffuse galaxies. The top-left panel places the van Dokkum et al. (2015) UDGs quite well in a continuous distribution with our sources.

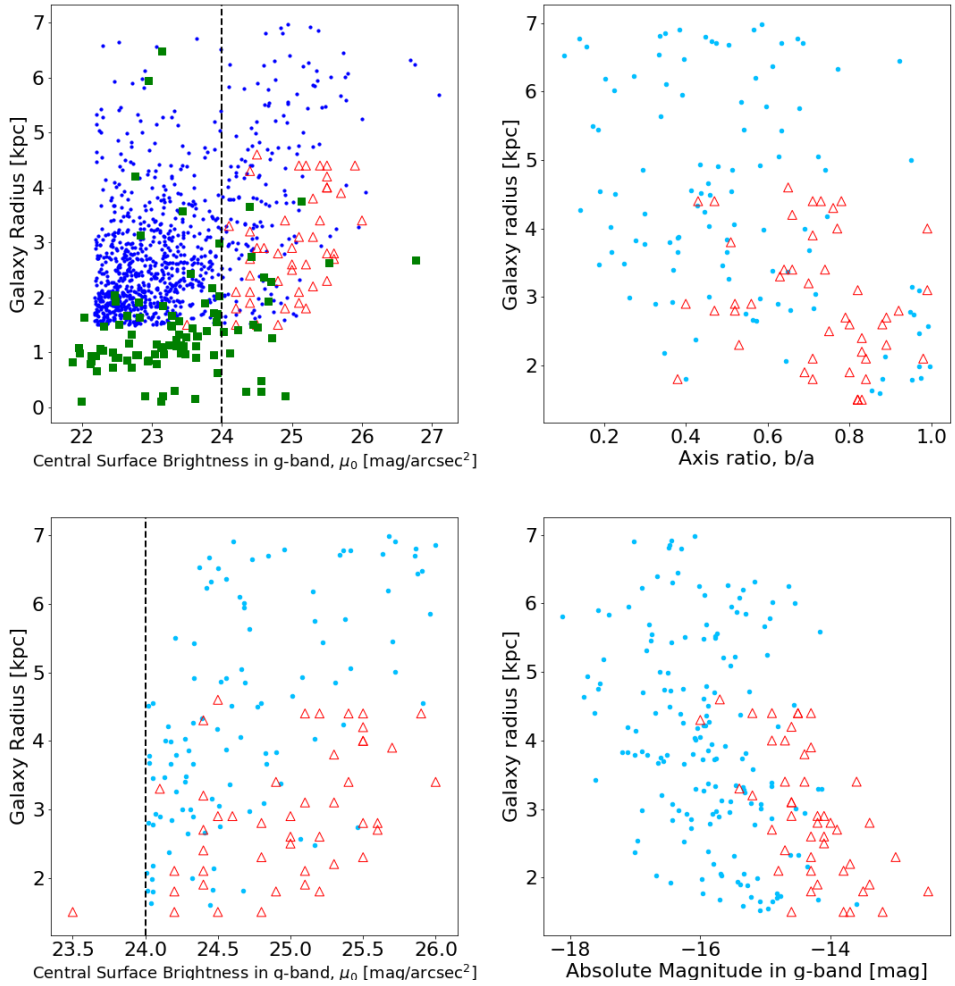

Figure 3.11: These figures directly compare the properties of our UDG candidates to the van Dokkum et al. (2015) UDGs and LSB galaxies. Our UDG candidates are shown in blue, while the van Dokkum et al. (2015) UDGs are identified by the red outlined triangles and the LSB galaxies are indicated by the green squares (O'Neil et al., 1997a). The top-left panel displays the galaxies radius vs. central surface brightness in the g-band for all sources. The top-right, bottom-left and right panels specifically compares the van Dokkum et al. (2015) UDGs to our UDG candidates after applying their central surface brightness criteria, $\mu_0(g) \gtrsim 24\,\mathrm{mag/arcsec^2}$ (plotted in light blue). The top-right panel displays the radius vs. axis ratio. The bottom-left panel displays the galaxies radius vs. central surface brightness in the g-band. The bottom-right panel displays radius vs. k-corrected absolute magnitude.

LSB galaxies from the wide-field survey for LSB galaxies (O'Neil et al. 1997a, O'Neil et al. 1997b) are also shown in the top-left panel of Figure 3.11. The galaxies from this survey were observed in regions centered on the Pegasus cluster, the Cancer constellation and the low density region of the Great Wall. We used the Lupton (2005) conversion to calculate the central g-band surface brightness from their observed B-band observations, $g = B - 0.3130 \times (g - r) - 0.2271$. The average colours of the galaxies in O'Neil et al. (1997a) are blue. We adopt a result from the IllustrisTNG simulations (Nelson et al., 2018), which indicates that a colour $g - r \sim 0.35$ approximately represents this population of blue galaxies. The radius of the sources were given in scale length. The average light profiles of these galaxies were exponential, therefore we are able to convert their exponential scale length (r_s) to effective radius using $r_e \simeq 1.678 \times r_s$ (Courteau et al., 1996).

The LSB galaxies have no minimum radius criteria, therefore a large number of their galaxies appear to have smaller radii than our sample and the van Dokkum et al. (2015) UDGs. Their size may be more comparable to dwarf galaxies. The surface brightness follows a similar trend to our UDG candidates, a larger number of brighter sources at small radii and fewer at larger radii. However, these LSB galaxies, on average, are much bluer than both our sample and the van Dokkum et al. (2015) UDGs. There is only a minority of LSB galaxies in their survey with colours indicative of an older population, this may be caused by selection effects.

3.2 UDG Properties After Background Subtraction

Galaxy clusters span a wide area, and many foreground and background sources may appear to be in the cluster when they are not associated. The radial distance to a source is required as well as the on-sky position to know the source's location. Since we do not have redshift information for all our cluster fields, there will be contamination of our cluster UDG samples due to galaxies in front of and behind our clusters. We will refer to this as background contamination. The background sources contaminate our UDG candidates in each cluster and potentially skew the properties we would like to investigate. Therefore we attempted to account for the average effect of background sources on our faint galaxy population. At this point we examine both the radius and surface brightness in 2-D histograms for each cluster and an average non-cluster field, thereby exploring the differences in the distributions and whether background subtraction can be done in 2-D space.

Each cluster was binned in both radius and surface brightness. The radius bins range from 1.5 - 7.0 kpc with a bin size of 0.5 kpc. The surface brightness bins range from 24 - 29 mag/arcsec^2 and have bin sizes of 0.5 mag/arcsec^2. As an example, Figure 3.12 displays three 2-D histograms, which shows the distribution of UDG candidates in cluster 15 with respect to their effective radius and effective surface brightness values. The remaining clusters are displayed in Appendix 5.4.

The left panel displays the distribution of UDGs in cluster 15 before applying background subtraction. Each cluster roughly covers the same phase-space regions with relatively similar number densities. In the combined sample of UDGs from all our clusters (Figure 3.10) we can see a smoother transition from the high density region to lower densities. Whereas, in the distributions for individual clusters we can see a number of isolated UDG candidates. These isolated sources are usually at fainter surface brightness where the data is incomplete.

The middle panel displays the background UDG-like sources (hereafter background sources) distribution scaled to the area of cluster number 15. Each cluster has a different size, and therefore we scaled the background sources for each cluster. As mentioned in methods Section 2.2.7, the background sources were obtained from 5 IAC Stripe 82 images. The average number of background sources were calculated per square degree. We use this value to determine the expected number of background sources in each cluster by scaling to the area of each cluster. Then, we determine the radius-surface brightness distributions for all the background sources in the 5 IAC Stripe 82 images. These distributions are scaled to the number of expected background sources in each cluster, plotted in the middle panel. The background cluster distribution is more concentrated toward small and bright sources. However, the UDG candidate sample is more evenly spread over several radii and surface brightness values with a much smaller inclination toward the small and bright sources. The candidates at larger radii and fainter surface brightnesses are easily seen above the background. This clearly shows the properties of our UDG candidates are distinct from the average properties of galaxies satisfying the same broad colour, surface brightness and radius cuts in the field.

The right panel displays the difference between the number of UDG candidates in each cluster and the averaged background scaled to the cluster's area. The scaled background is directly subtracted from the UDG candidate distribution. In these figures the negative bins represent regions in the radius-surface brightness space where the number of estimated background sources exceeds the number of UDG candidates in the cluster. The positive bins represent regions in the space where our UDG candidates exist above the estimated background. The fainter and larger UDG candidates are relatively unaffected by the background subtraction, whereas the smaller and brighter regions are greatly affected by the background subtraction. Table 2.6 in Section 2.2.7 shows the final counts which are displayed in these figures.

Figures 3.13, 3.14 and 3.15 display the background subtracted 2-D distributions for all the clusters. The 2-D histograms are also deconstructed into 1-d radius and surface brightness histograms in these figures. Negative counts, where the number of background sources is greater than the number of UDG candidates, are also displayed. At the low radius and bright end regions the number of UDG candidates fluctuates. The number of resulting sources in each bin in this phase-space appears to be random. Bins with positive and negative counts are scattered without a clear pattern at these values. At larger radius and fainter surface brightness we clearly see positive counts in the 2-D histograms. However, the 1-d histograms do not directly reflect this. The background sources are a continuous distribution. The number of background sources in each bin may be much lower than the number of UDG candidates in particular bins at the large and faint regions of the 2-D histograms. However, when flattening the 2-D histograms into two 1-d histograms these average background sources accumulate and negate the positive UDG candidate counts. On average we can clearly and consistently distinguish our UDG candidates at larger radius and fainter surface brightness in the 2-D phase-space from the background. The background sources do not have large average counts in these regions. This region where the candidates in the clusters are consistently above the background is also where the UDGs which satisfy the van Dokkum et al. (2015) criteria are found.

The effects of incompleteness on the background sources is identical to that of our UDG candidates. The fraction of observed sources compared to expected sources decreases at fainter surface brightnesses. The 2-D histograms in Figures 3.13, 3.14 and 3.15 show that the background has much lower counts at larger radii and fainter surface brightness than the UDG candidates in the 2-D phase space. This shows that the background is deficient of faint and large UDG-like sources and only very few are expected to exist. Therefore, at the largest radii and faintest surface brightnesses only the UDG candidates in clusters are expected to have significant numbers which we do not have the sensitivity to observe. With more sensitive data we would expect our 2-D histograms to show a clearer overdensity of large and faint UDG candidates in the cluster compared to the background.

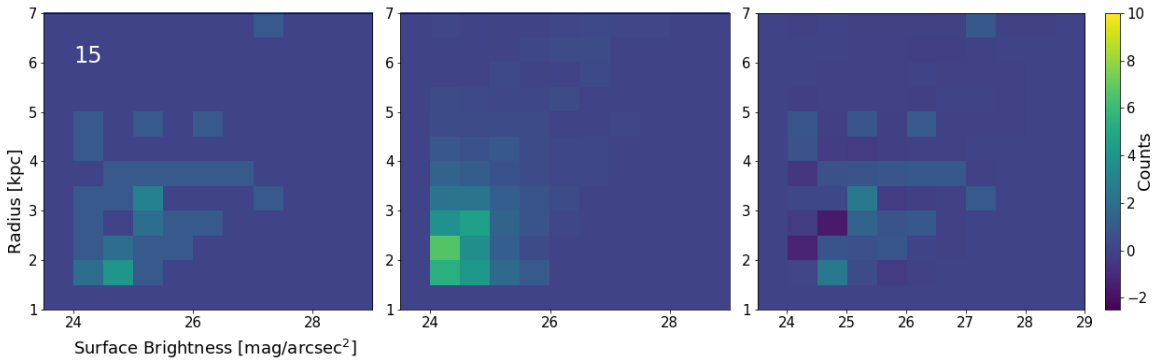

Figure 3.12: Two dimensional binned distributions of radius and surface brightness in cluster 15. The left panel shows the UDG candidates found with our UDG detection method in the cluster area. The middle panel displays the average number of UDG-like objects in the background images scaled to the area of cluster 15. The right panel displays the difference between the UDG candidates in the cluster and background. The background is subtracted from the UDG candidates. In a few bins there are more galaxies in the background, resulting in negative values.

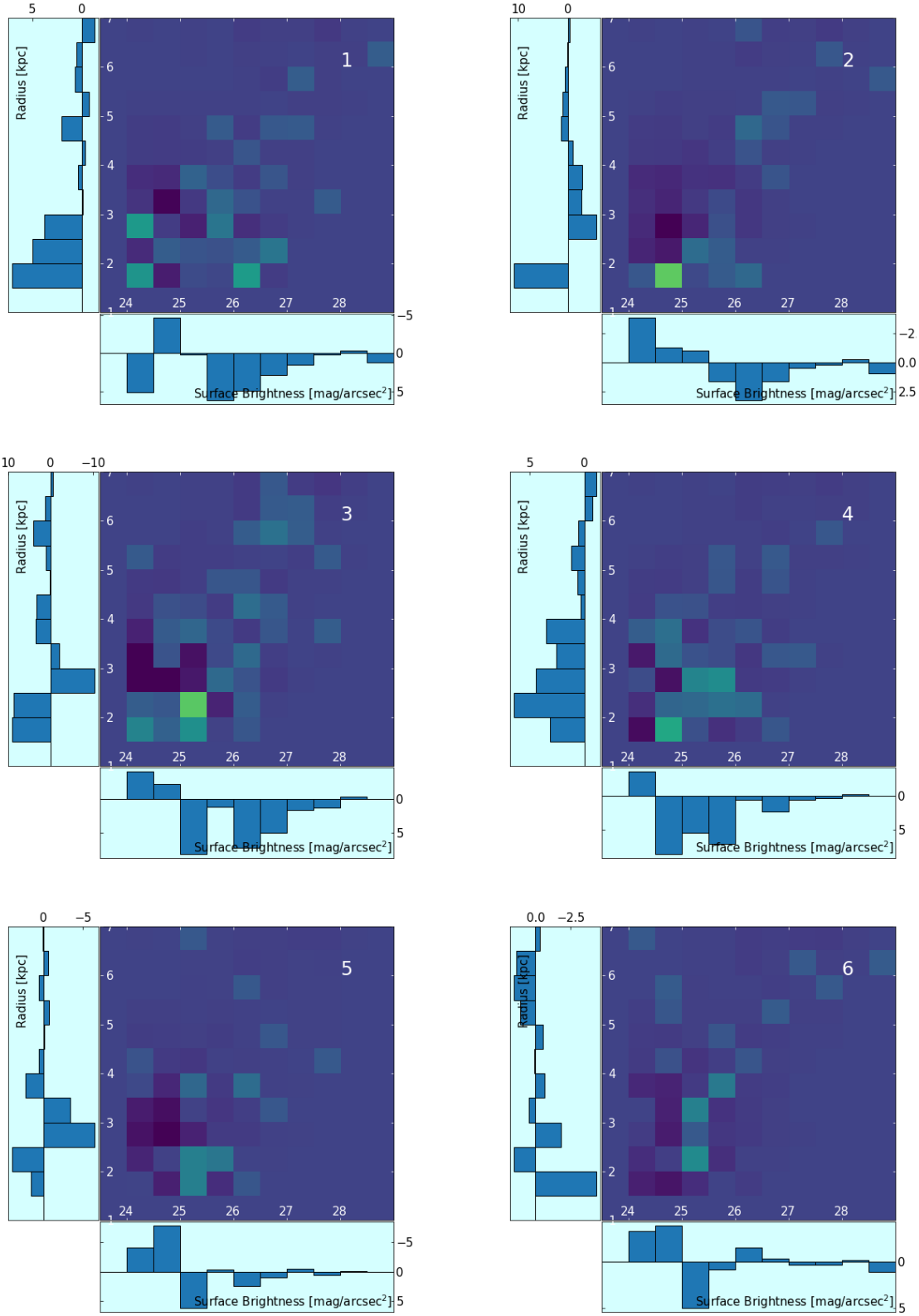

Figure 3.13: These two dimensional plots replicate the right panel of Figure 3.12 for each cluster, showing where there is an excess of cluster UDG candidates compared to the background. The histograms on the vertical and horizontal axes measure the radius and surface brightness distributions of the cluster UDG candidates after subtracting the background sources. The radius histograms display positive counts toward the left and the surface brightness histograms display positive counts downward. Clusters 1-6 are displayed on this page, clusters 7-16 are displayed on the subsequent pages.

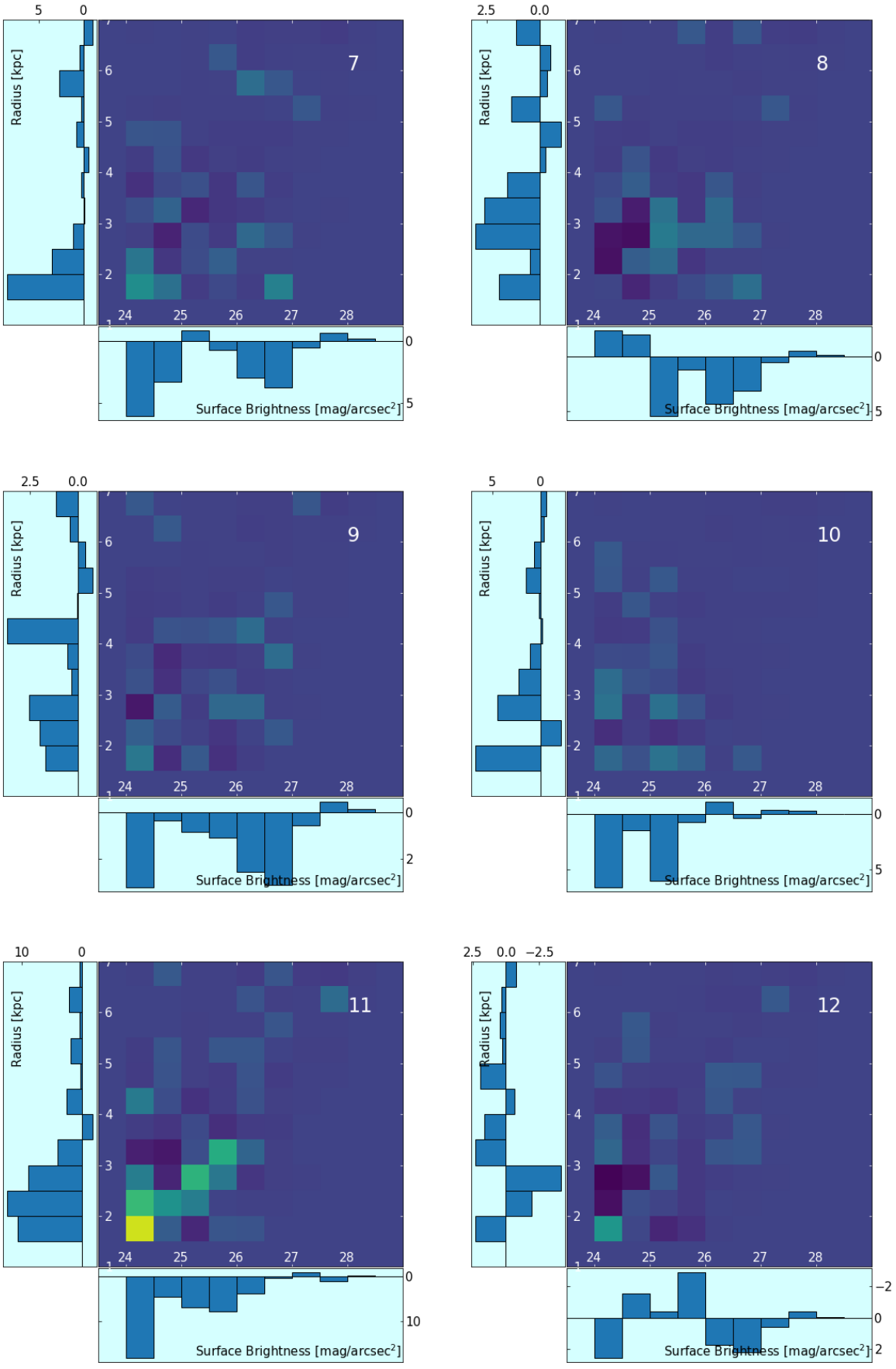

Figure 3.14: (Continued) Two dimensional plots of clusters 7-12 with two one dimensional histograms of the radius and surface brightness.

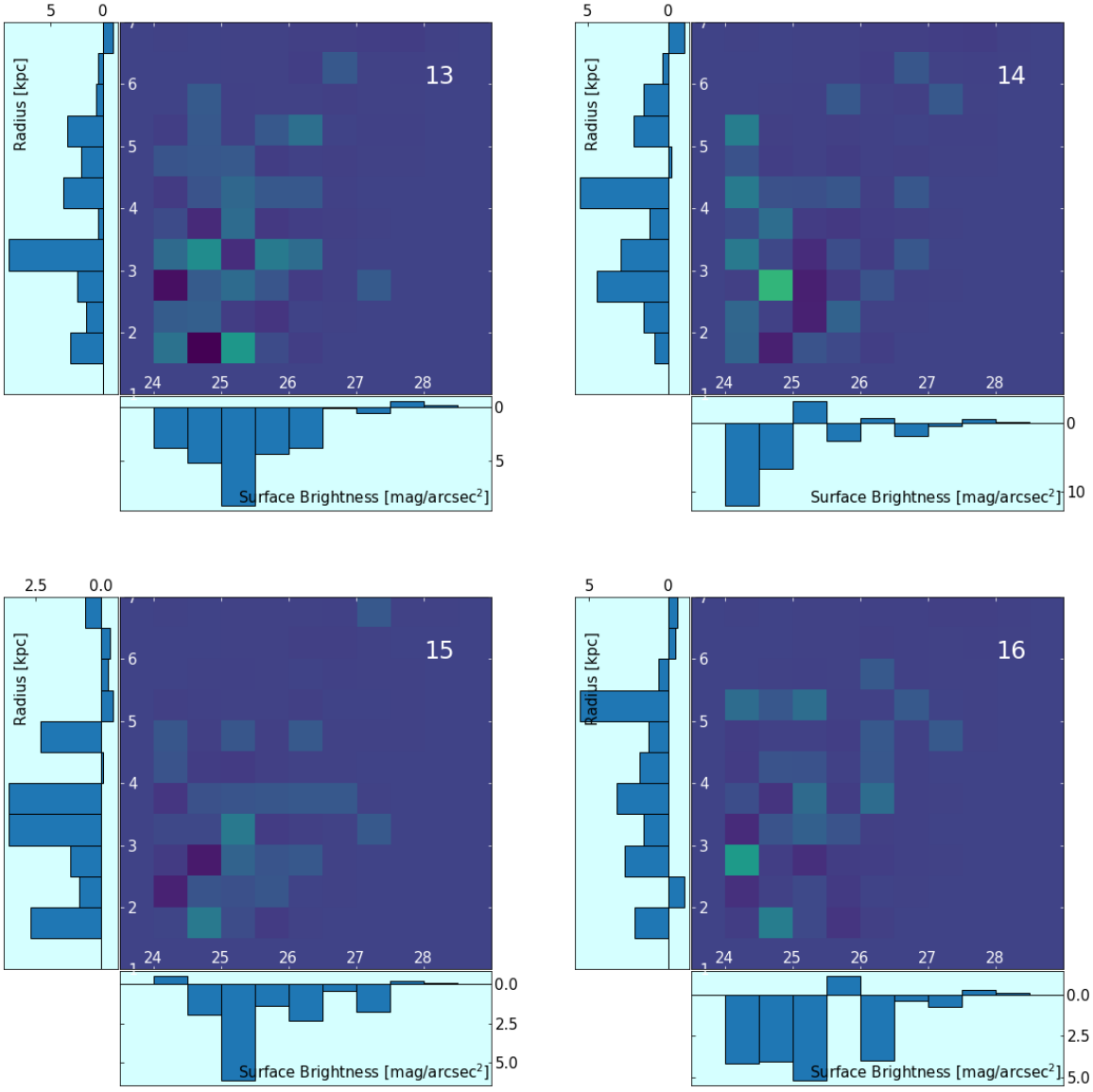

Figure 3.15: (Continued) Two dimensional plots of clusters 13-16 with two one dimensional histograms of the radius and surface brightness.

3.2.1 Cumulative Properties

We accumulate the properties of all the UDG candidates in our 16 clusters into a single set. Analyzing all the UDG candidates as a whole improves the quality of the results as the sample is much larger. The difference in redshift may be an indication of different stages in UDG evolution, and furthermore, these UDG candidates may have different properties. However, the 16 clusters in our sample only span a small redshift range, $0.09 < z < 0.15$. The evolutionary effect over this small redshift range is likely to be quite small (see also Section 3.3 and Figure 3.19), therefore we group our UDG candidates together and perform analysis on the whole candidate sample. The background UDG-like properties are determined using average values scaled to the cluster size. Subsequently, we do not compare UDG candidates to background sources directly, but, rather their averaged properties.

The radius, surface brightness and Sérsic index of all the UDG candidates, background sources and the difference are plotted in Figures 3.16, 3.17 and 3.18 respectively. The top panel compares the UDG candidate properties to the background and the bottom panel displays the difference between the candidates and the background. In the radius and surface brightness plots we see very low or negative counts in the difference plots. These negative counts arise when flattening the continuous background distribution into a 1-d histogram and subtracting from discrete candidate counts, see Section 3.2 above. This results in a histogram which does not reflect the sample in its entirety. Here, the excess of the background sample can be seen when the background distribution exceeds in counts above the UDG counts. This difference can clearly be seen in the bottom panel of Figures 3.16, 3.17 and 3.18, where the counts become negative.

The radius distribution of the UDG candidates and the background follows the same overall trend, decreasing counts as the radius increases. The number of candidates exceeds the background in all bins except the largest radius bin, $6.5 < r_e < 7.0$ kpc. In the difference plot we can clearly see the number of UDG candidates in each radius bin after the background subtraction. The number of UDG candidates once again peaks at low radii. The counts become level at 3 kpc and remain constant until 6 kpc.

The surface brightness distribution shows an overall decrease from brighter to fainter sources for both the background and UDG candidates. In the difference plot we see the counts drop in bin $24.5\,\mathrm{mag/arcsec^2}$ and peak at bin $25.0\,\mathrm{mag/arcsec^2}$. This may potentially be a binning effect; between $24\,\mathrm{mag/arcsec^2}$ and $26.5\,\mathrm{mag/arcsec^2}$ the bins all have approximately 30 counts except bin $24.5\,\mathrm{mag/arcsec^2}$ and $25\,\mathrm{mag/arcsec^2}$. The average of these two neighbouring bins is similar to the ~ 30 average source count. This may suggest that our UDGs are equally likely to have any surface brightness within this range.

The cumulative Sérsic index distribution of the background clearly shows a significant number of background sources with very low indices. Whereas the UDG candidates peak at $n \sim 1$, which is an exponential profile and consistent with previous research, displayed in Table 1.1 and discussed in Section 1.3.1. Both the background and the UDG candidates have a steep drop in counts toward the higher Sérsic values, with the cluster candidates consistently having more counts. The difference plot clearly displays the negative first bin. The difference between the UDG candidates and background sources are clear. The large counts at Sérsic index, $n \sim 1$ can easily be seen, and indicates UDGs are likely to have exponential profiles. Whereas, a large number of the UDG-like background sources have Sérsic indices, $n \lesssim 0.5$.

There are several limiting factors affecting our candidate UDGs, namely the completeness limit, GALFIT model uncertainties and large background correction. The uncertainties of converged GALFIT models are the least impactful on our final results, each galaxy is visually inspected and the inaccurate models are removed. However, the model uncertainties of the GALFIT models that did not converge will have a significant impact on the final number of UDGs in our clusters. The surface brightness limit restricts the number of UDG candidates we can detect, while the large background subtraction removes potential candidates to account for the foreground and background UDG-like sources. The effect of the background on the largest and faintest sources is somewhat mitigated as the background is deficient of these galaxies and therefore affirms UDG overdensities in clusters (see Section 3.2). The completeness limit of the IAC data implies that we only observe very few of the largest and faintest sources, thus, we cannot effectively study them in great detail. Therefore, the GALFIT model uncertainties, completeness limit and large background subtraction have a substantial effect on our UDG samples in each cluster and limit the number of UDG candidates we observe. However, the properties of our UDG candidates are still observed given these limitations. Therefore, these results reflect the population of UDGs in these clusters and indicate a lower limit to the number of UDG candidates in these clusters.

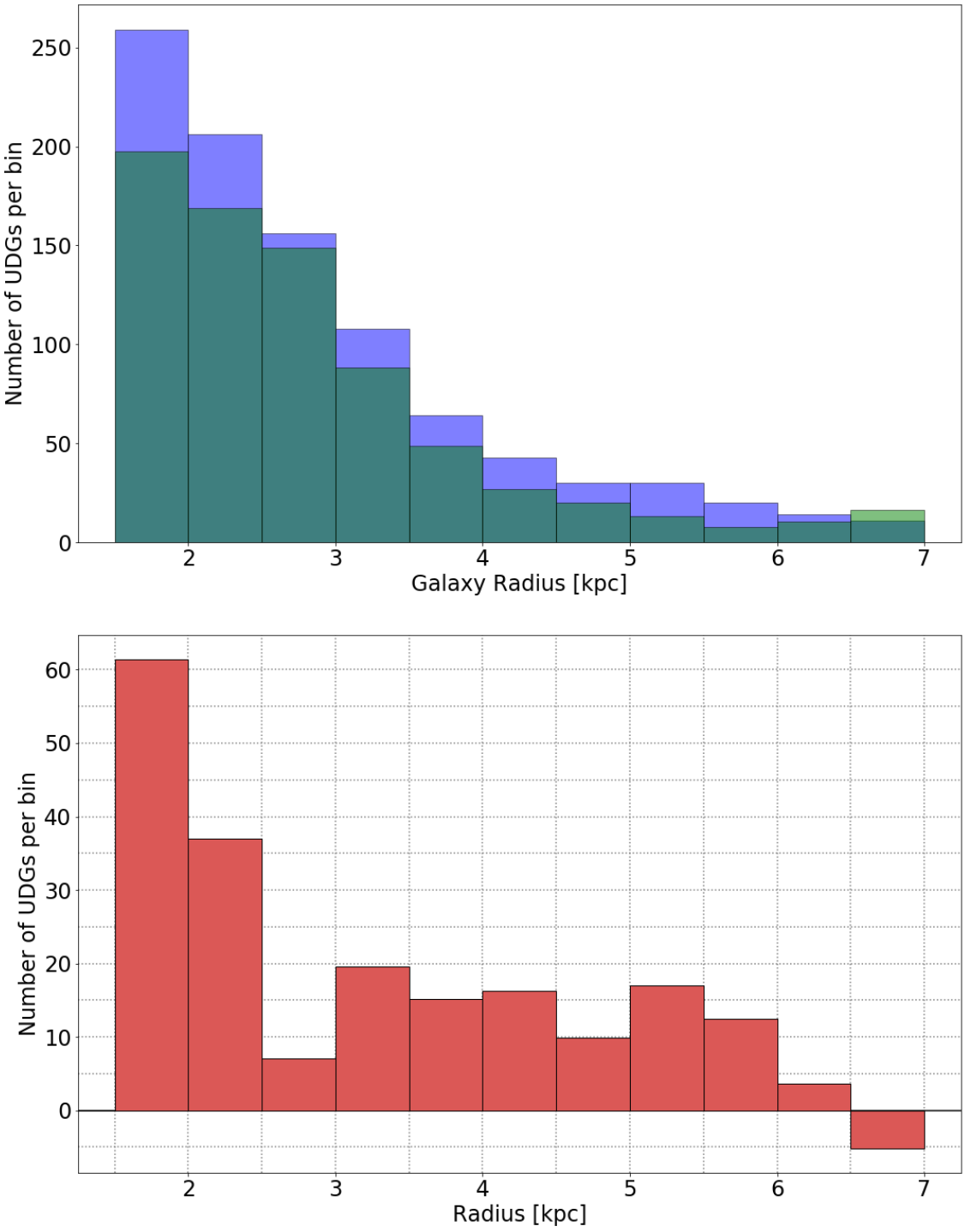

Figure 3.16: Histogram of the radius of the total UDG counts, combining the UDG candidates all the clusters. In the top panel the blue histogram displays the UDG candidates before background subtraction and the green plot displays the total number of background sources. The bottom panel shows the difference between the number of UDG candidates and background sources with respect to their radius.

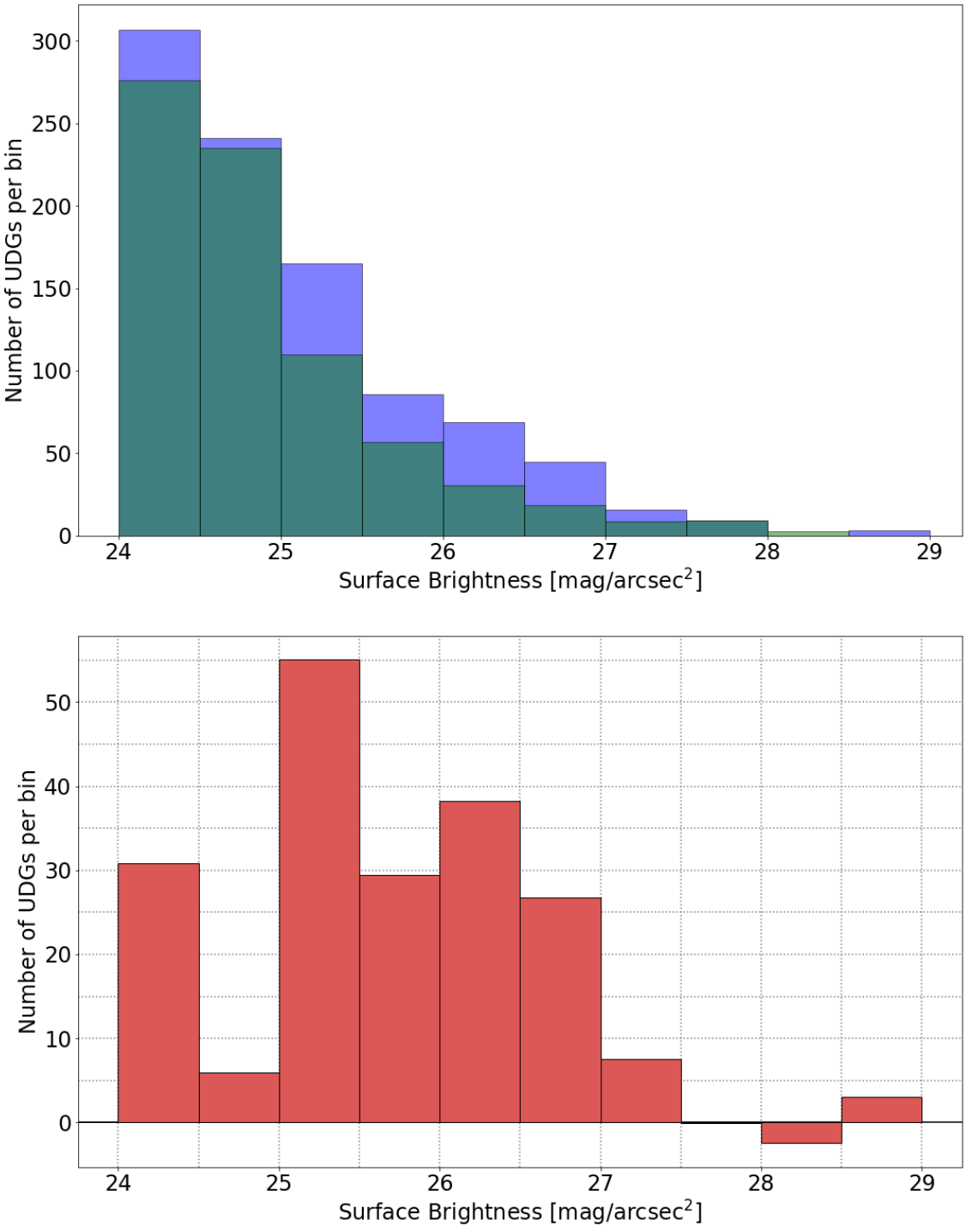

Figure 3.17: Histogram of the surface brightness of the total UDG counts, combining the UDG candidates all the clusters. In the top panel the blue histogram displays the UDG candidates before background subtraction and the green plot displays the total number of background sources estimated over the total cluster area. The bottom panel shows the difference between the number of UDG candidates and background sources with respect to their surface brightness.

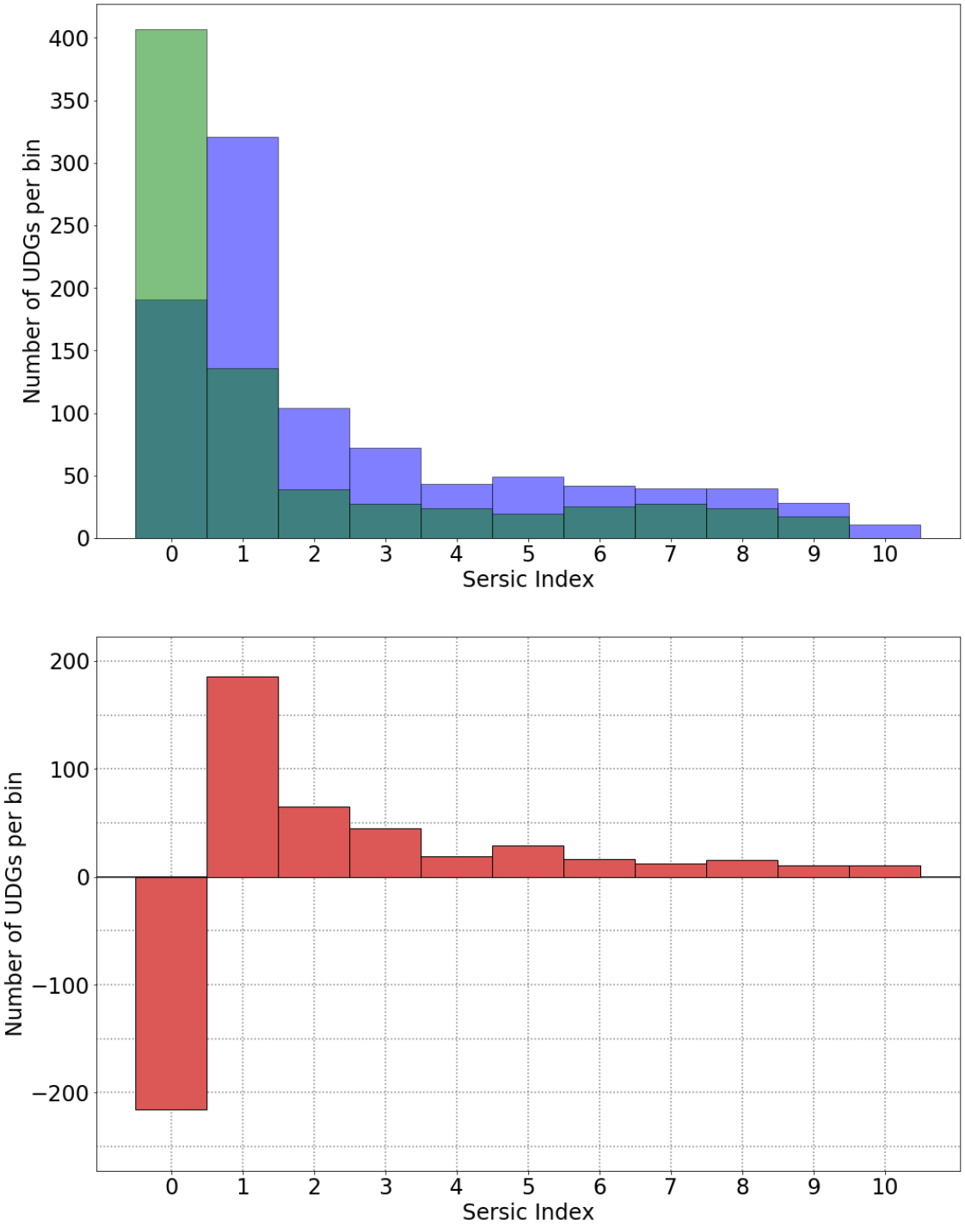

Figure 3.18: Histogram of the Sérsic indices of the total UDG counts, combining the UDG candidates all the clusters. In the top panel the blue histogram displays the UDG candidates before background subtraction and the green plot displays the total number of background sources estimated for the total area. The bottom panel shows the difference between the number of UDG candidates and background sources with respect to their Sérsic indices.

3.3 Effects of the Cluster Environment

The effect of the cluster environment on the formation and evolution of UDGs is particularly interesting. As mentioned in Section 1.2.1 in the introduction, this environment is quite hostile and the cluster's tidal fields are expected to destroy diffuse and extended sources like UDGs. However, the abundances measured recently, Table 1.1 in the introduction, indicate that they are able to survive in these extreme environments. Studying the properties of UDGs and their host clusters, particularly redshift and cluster halo mass, may yield information on UDG evolution. We investigate these cluster properties and their respective UDG numbers. The final UDG candidate count per cluster in our sample after background subtraction is displayed in Table 2.6.

The number of UDG candidates vs. redshift is shown in Figure 3.19. The colour indicates the richness of each cluster; low richness are shown in red, while high richness are shown in purple. The error-bars are calculated by the root-sum of the Poisson errors and the standard deviation of the background counts. The spread in UDG numbers across the redshift range at different levels of richness indicate that the number of observed candidates are not directly effected by the richness, nor the redshift. However, the redshift range, $0.09 < z < 0.15$, is quite small and paired with a sample of only 16 clusters may not be sufficient to determine any redshift relationship. The average number of UDG candidates per cluster is 14.0 with a standard deviation of 10.8. The large standard deviation results from having a wide range of UDG counts: $\sim$ 41 in our richest cluster, and negative (background subtracted) counts in our poorest. In previous studies of UDGs in clusters, displayed in Table 1.1, the number of UDGs are spread from only a handful in some clusters to a few hundreds in others. The techniques and telescopes used to find and measure the properties of these UDGs are quite varied. This makes comparing different clusters and different surveys without bias very difficult, however I compare in more detail where possible below.

UDG candidate numbers per cluster are then plotted as a function of their respective cluster's halo masses in Figure 3.20. The colour indicates the redshift of each cluster; low-redshift clusters are red, while higher-redshift clusters are shown in purple. Once again the error-bars are calculated by the root-sum of the Poisson errors and the standard deviation of the background. A caveat is that there is a large amount of intrinsic scatter in the mass-richness relation and this contribution as well as the uncertainties on the cluster masses are not taken into account in the fit. Most of the UDG counts are positive, only 2 clusters have negative counts. The negative counts indicate the background UDG-like sources in the same effective area are more numerous than UDG candidates. The data can be seen to follow a trend, from low UDG numbers at low cluster halo mass to higher numbers in cluster halos with more mass. Much of this trend seems to be driven by the most massive cluster. This indicates the importance of having a large sample with a broad range of redshifts and cluster halo masses. The solid black line is a best fit power-law regression curve, $N \propto M^{1.11 \pm 0.25}$; the negative values have been ignored for the fit. To create the best fit lines we use a generic power-law model and the Model function in the IMFIT package (Erwin, 2014) in Python (Van Rossum & Drake Jr, 1995). The green dotted line excludes the richest cluster, which shows a flatter trend and higher error, $N \propto M^{0.56 \pm 0.53}$. To test the robustness of the determined power-law I applied a bootstrap resampling test to the clusters with positive UDG numbers. I resampled the 14 data points randomly 1000 times with replacement and determined the median power-law, $N \propto M^{1.05 \pm 0.45}$. Figure 3.21 displays the distribution of the resampled power-law exponents. The bootstrap resampled power-law is indicated by the blue dotted line in Figure 3.20. This result agrees within the uncertainty of our best fit power-law and indicates that the power-law is not entirely driven by the most massive cluster. The error bar of the resampled power-law may be large, however, there is still a clear agreement with our best fit power-law. This indicates that our best fit power-law slope is significant and the relation is robust.

Figure 3.22 compares the UDG candidates in our cluster sample to the UDGs numbers found in other clusters with respect to the cluster's halo masses, listed in Table 1.1. We apply a brighter surface brightness criteria, therefore we cannot directly compare their numbers. However, our number of UDG candidates and halo masses lie within a similar region as the previous reseach. We see that the power-law determined by van der Burg et al. (2016), $N \propto M^{0.93 \pm 0.16}$, is similar to the power-law of our brighter UDG candidates. This may indicate that the number of UDGs within a cluster follow the same relation with cluster halo mass as our UDG candidates. We examine the van der Burg et al. (2016) UDGs more closely in Section 3.3.1 below.

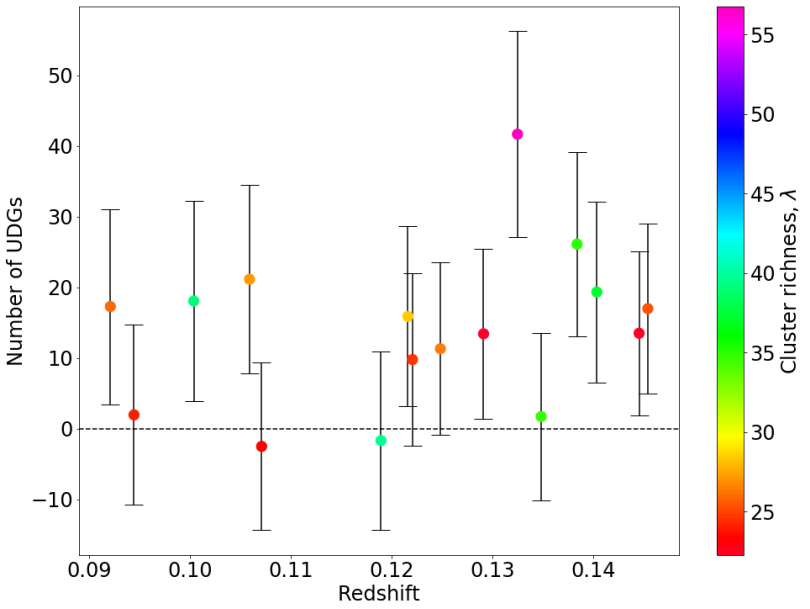

Figure 3.19: The number of UDG candidates as a function of redshift are shown. The RedMaPPer cluster richnesses are discerned by the colour bar. The error-bars indicate the root-sum square of the Poisson error on the UDG sample and standard deviation of the background.

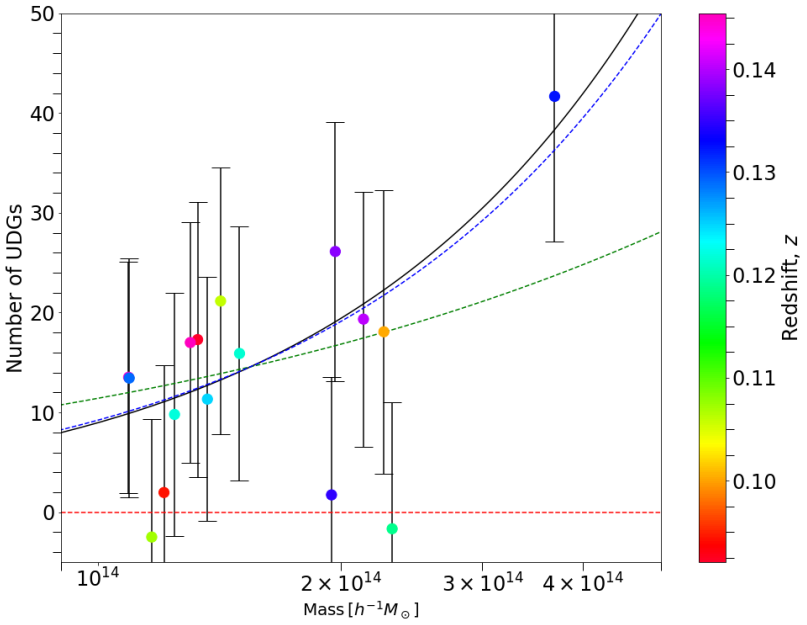

Figure 3.20: The number of UDG candidates vs. cluster halo mass are plotted. The redshift of the clusters are discerned by the colour bar. The error-bars indicate the root sum square of the Poisson error on the UDG sample and standard deviation of the background. The black solid line indicates the best fit regression curve, $N \propto M^{1.11 \pm 0.25}$, the negative values have been ignored for the fit. The green dotted line excludes the richest cluster as well as the negative values, $N \propto M^{0.56 \pm 0.53}$. The blue dotted line is the median bootstrap resampled best fit curve, excluding the negative values, $N \propto M^{1.05 \pm 0.45}$.

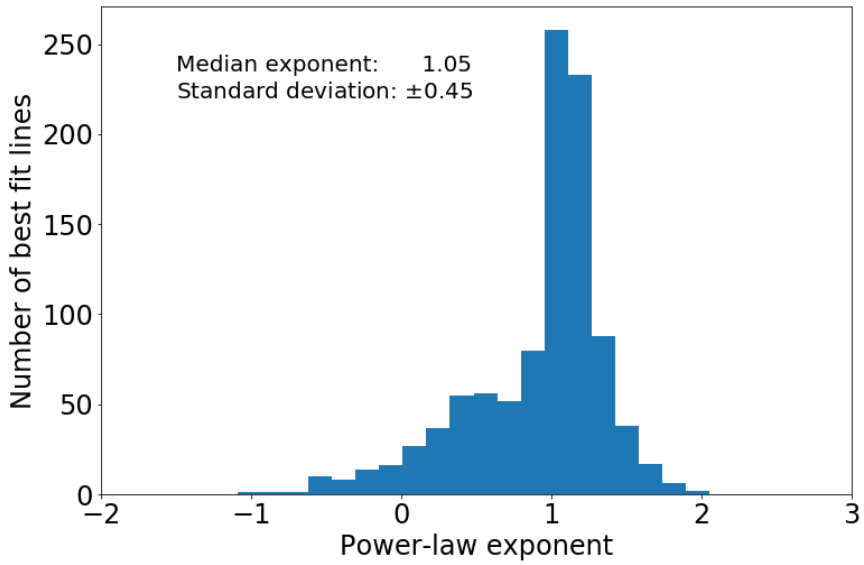

Figure 3.21: Histogram displaying the distribution of power-law exponents from the bootstrap resampling test. The median exponent is 1.05 with a standard deviation of 0.45.

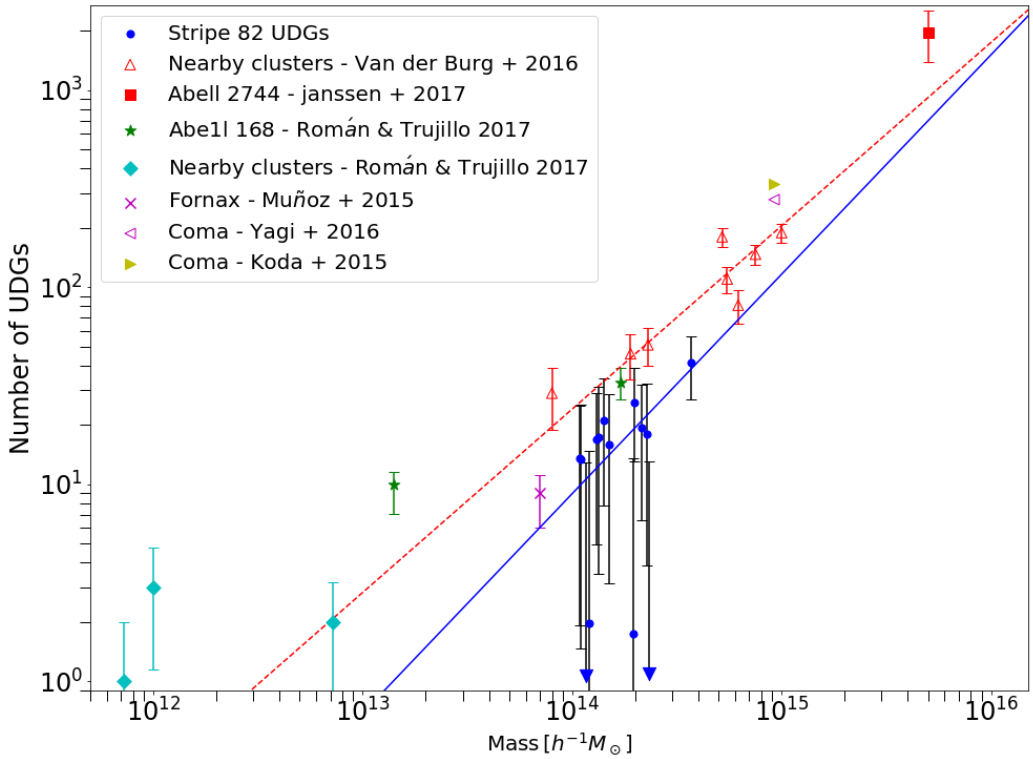

Figure 3.22: The number of UDG candidates vs. cluster halo mass, comparing previous research (listed in Table 1.1) to our Stripe 82 clusters. The solid blue line indicates our best fit power law regression curve, $N \propto M^{1.11 \pm 0.25}$, we have excluded the clusters with negative UDG counts. The red dotted line is the van der Burg et al. (2016) best fit power law, $N \propto M^{0.93 \pm 0.16}$. The blue downward arrows indicate the two UDGs which have negative UDG numbers.

3.3.1 Comparison to Van der Burg et al. (2016)

The nearby clusters investigated by van der Burg et al. (2016) have a similar halo mass range to our cluster sample and it's the largest sample currently available in the literature. To compare the UDGs, their properties and the cluster properties directly between the two studies is not a fair comparison, as the methods employed are somewhat different. However, we make this comparison and highlight differences in the methods in an effort to understand the similarities and differences in the results. We use Figure 3.23, which is identical to Figure 3.22 with our UDG candidates and the van der Burg et al. (2016) UDGs only, to make this comparison. There may be differences in the UDG selection, as well as a systematic difference in halo mass on the x-axis.

Van der Burg et al. (2016) used data collected in the Multi-Epoch Nearby Cluster Survey with MegaCam on the Canadian French Hawaii Telescope (Sand et al., 2011). Identifying clusters in the redshift range $0.044 < z < 0.063$, which is less distant than any of our clusters ($0.09 < z < 0.15$). Van der Burg et al. (2016) use the r-band to identify their UDGs, while we used the g-band. The MegaCam data reaches a 50% completeness limit at an approximate central surface brightness in the r-band of $\mu_0(r) \sim 25.2\,\mathrm{mag/arcsec^2}$. The IAC Legacy project reaches a 50% completeness limit in the g-band at $\mu_e(g) = 26\,\mathrm{mag/arcsec^2}$, which is equivalent to a central surface brightness of $\mu_0(g) \sim 24.2\,\mathrm{mag/arcsec^2}$. By using different wavelength bands we may select slightly different sources. We used effective surface brightness to identify our UDG candidates, whereas van der Burg et al. (2016) used the mean effective surface brightness to identify their UDGs. The mean effective surface brightness criteria they use is $24\,\mathrm{mag/arcsec^2} < <\mu_e(r)> < 26.5\,\mathrm{mag/arcsec^2}$, which is equivalent to a central surface brightness of $22.9\,\mathrm{mag/arcsec^2} < \mu_0(r) < 25.4\,\mathrm{mag/arcsec^2}$. The average $g-r$ colour of 9 typical UDGs in their clusters approximates to $< g - r > \simeq 0.60$. Therefore, we can expect the g-band to be ~ 0.6 mag fainter and the central surface brightness criteria in the g-band to be $23.5\,\mathrm{mag/arcsec^2} < \mu_0(g) < 26.0\,\mathrm{mag/arcsec^2}$. Our sample does not have a maximum surface brightness limit, however our 50% completeness limit is comparatively lower than the 50% limit in the MegaCam data used by van der Burg et al. (2016). Therefore we have a few fainter candidates than van der Burg et al. (2016), however van der Burg et al. (2016) observe more fainter UDGs.

The methods implemented to differentiate the UDGs from the background sources are also quite different. We remove background sources by discarding all sources beyond the red sequence of each cluster. Van der Burg et al. (2016) uses a method which weights each source in the cluster's field, thereby effectively considering galaxies with colours different from the clusters red sequence. This allows van der Burg et al. (2016) to potentially detect higher numbers of UDGs. Previous research has shown that UDGs in clusters are typically red in colour and generally follow the cluster's red sequence. Therefore, we are more likely to detect typical red UDGs.

Our cluster halo masses, M_{200}, are calculated with the cluster mass-richness relation (Simet et al., 2018) using the cluster richness, λ, determined in the RedMaPPer catalogue (Rykoff et al., 2014). Van der Burg et al. (2016) use the M_{200} cluster mass determined by Sifón et al. (2015) using the σ_{200} - M_{200} relation described in Evrard et al. (2008). Sifón et al. (2015) use the clusters dynamics to determine its properties, whereas the mass-richness relation we used relies on weak-lensing. Given the different methods, there could be a systematic offset in the halo masses of our clusters compared to the van der Burg et al. (2016) clusters.

The number of UDG candidates in our sample increase as a power-law with respect to cluster halo mass, $N \propto M^{1.11 \pm 0.25}$. Van der Burg et al. (2016) report a similar power-law relationship, $N \propto M^{0.93 \pm 0.16}$. Regardless of the differences between the UDG candidates in our sample and the van der Burg et al. (2016) UDGs we still find a similar relationship between UDG numbers and the cluster halo mass. This indicates that the number of galaxies identified by each study may be similarly affected by their host clusters halo mass, with rich, more massive clusters having higher numbers of dwarf galaxies and UDGs.

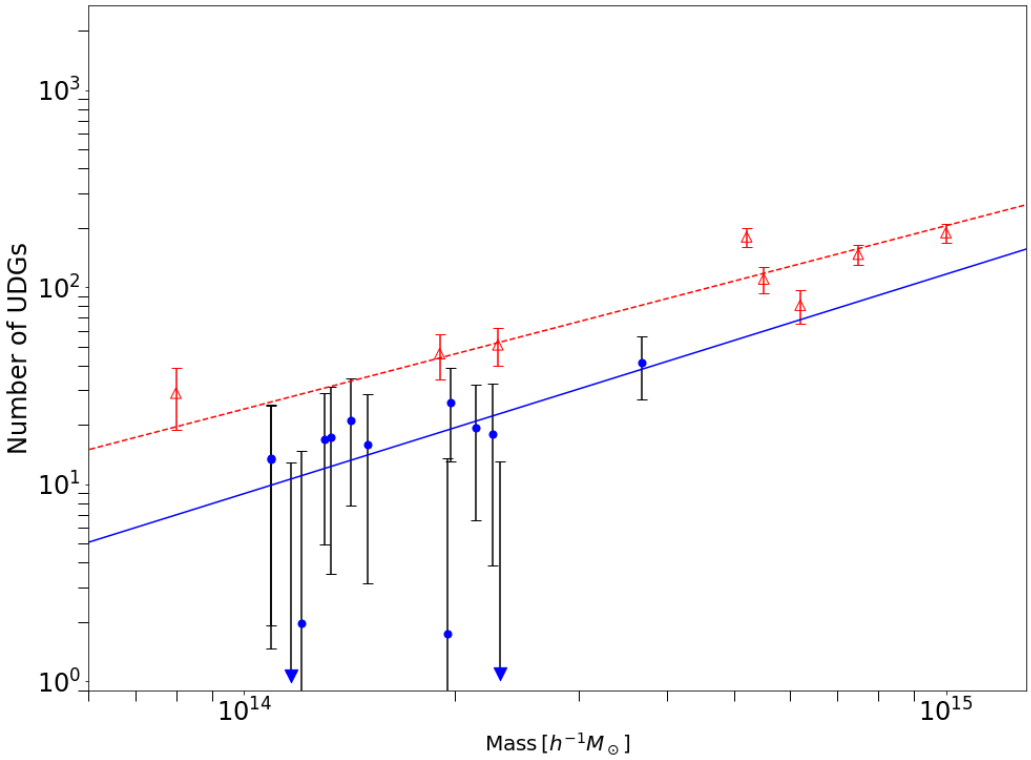

Figure 3.23: The number of UDG candidates vs. cluster halo mass, comparing van der Burg et al. (2016) in red to our Stripe 82 clusters in blue. The solid blue line indicates our best fit power law regression curve, $N \propto M^{1.11 \pm 0.25}$, we have excluded the clusters with negative UDG counts. The red dotted line is the van der Burg et al. (2016) best fit power law, $N \propto M^{0.93 \pm 0.16}$. The blue downward arrows indicate the two UDGs which have negative UDG numbers.

Chapter 4

Conclusions

The aim of this thesis is to identify and characterize large and faint galaxies in clusters to better understand the effects of the cluster environment on galaxy formation. I use data from the IAC Stripe 82 legacy project in conjunction with the RedMaPPer cluster catalogue to find all the low surface brightness galaxies in 16 low redshift clusters at z < 0.15 within the Stripe 82 region. To distinguish the large and faint galaxies from the rest of the galaxy population in the clusters, we selected all sources within the r_{200m} radius of each cluster and applied a color cut to identify galaxies on the red sequence. GALFIT was used to model each of the sources. We applied cuts to the properties of the sources to select the LSB and UDG galaxies in the clusters. Contamination from background sources was estimated by comparing the sample to a similarly selected galaxy population from five random field areas in Stripe 82. This is the largest sample of clusters that has been uniformly searched for UDGs to date.

We find 941 galaxies satisfying our criteria, $r_e \gtrsim 1.5\,\mathrm{kpc}$ and $\mu_0(g) \gtrsim 24\,\mathrm{mag/arcsec^2}$, in the 16 Stripe 82 clusters. Of these, 165 are classified as UDGs following van Dokkum et al. (2015). After taking into account that many of these are likely in the foreground/background we compared our candidates to field galaxies and conclude the following:

1. Investigating the individual distributions of the galaxy properties within each cluster (Section 3.1) shows:
   - UDG candidates do not have a preferred spatial location within the clusters. We find that our UDG candidates do not avoid the central 300 kpc region in cluster, as seen in previous work (van Dokkum et al., 2015).
   - The number of UDG candidates decreases as galaxy radius (r_e) increases. The surface brightness ($\mu_e(g)$) follows a similar trend, decreasing UDG candidate numbers as surface brightness values increases. The change in slope of the radius distributions with redshift indicates that we find more smaller radii candidates in low redshift clusters than the higher redshift clusters.
   - A large number of candidates have exponential light profiles, with the median Sérsic index over all 16 clusters $n = 1.28$. Previously reported UDG Sérsic indices ($n \sim 1$) indicates that our UDG candidates have similar light profiles to UDGs in the literature.
2. Investigating the distributions of our total UDG candidate sample (Section 3.1.5) shows that the average axis ratio of our candidates is <b/a>=0.52 and their distribution is spread near-evenly, from highly elongated sources to circular sources. The van Dokkum et al. (2015) average axis ratio is <b/a>$\sim$0.7, and is more concentrated around this value. The axis ratio of our UDG candidates which satisfy the van Dokkum et al. (2015) surface brightness cut have a similar distribution to the van Dokkum et al. (2015) UDGs for small galaxies ($r_e \sim 1.5\,\mathrm{kpc}-2.5\,\mathrm{kpc}$). The distributions of both samples approach axis ratios of b/a ~ 1 for sources which are close to the radius criteria, $r_e \gtrsim 1.5\,\mathrm{kpc}$. As the resolution limit is approached sources appear to be rounder and more point-like. The larger candidates are more elongated, which is also true for the van Dokkum et al. (2015) UDGs.
3. The galaxies we have identified in this thesis span the space between the normal galaxies identified in the SDSS survey and extreme UDGs with very low SB as defined by van Dokkum et al. (2015). We see that UDGs are simply an extension of the global galaxy population, the faintest and most diffuse galaxies.

4. The surface brightness values of LSB galaxies in the Pegasus cluster, Cancer constellation and low density regions of the Great Wall (O'Neil et al. 1997a, see Section 3.1.6) follow a similar trend to our UDG candidates: a larger number of brighter sources at small radii and fewer at larger radii, even though these LSB galaxies are much bluer than both our sample and the van Dokkum et al. (2015) UDGs. There are a small number of redder LSB galaxies in their survey that are likely to be older. This potentially implies an evolutionary scenario, where larger LSB galaxies evolve to UDGs.

5. Comparing the property distributions of the UDG candidates and background (Section 3.2) show:

   - At large radii and faint surface brightness UDG candidates are easily visible above the background. The background distributions are more concentrated toward the smaller and brighter region, with very low counts at the large and faint end. This clearly shows the properties of our UDG candidates are distinct from the average properties of galaxies satisfying the same broad colour, surface brightness and radius cuts in the field. This region where the candidates in the clusters are consistently above the background is also where the UDGs which satisfy the van Dokkum et al. (2015) criteria are found.
   - The radius distributions of the UDG candidates and the background follow the same overall trend, decreasing counts as the radius increases. However, between 3 kpc and 6 kpc the counts become level.
   - The surface brightness of the UDG candidates and the background follow the same overall trend, decreasing counts from brighter to fainter sources. However, the UDG candidates appear to consistently have the same counts above the background, suggesting that our UDGs are equally likely to have any surface brightness within this range.
   - The Sérsic indices of the UDG candidates peak at n$\sim$1, which is an exponential profile and consistent with previous research. In contrast, the background distribution clearly shows a significant number of sources with much lower indices.

6. The spread in UDG numbers across the redshift range at different levels of richness indicate that the number of observed candidates is not directly affected by the the redshift over the relatively narrow redshift range probed here.

7. The number of UDG candidates as a function of cluster halo mass is best fit with the power-law $N \propto M^{1.05\pm0.45}$, , determined through bootstrap resampling. This is comparable to the power-law determined by van der Burg et al. (2016), $N \propto M^{0.93\pm0.16}$. This indicates that the number of galaxies in both studies may be similarly affected by their host clusters halo mass, with richer, more massive clusters having higher numbers of dwarf galaxies and UDGs.

4.1 Outlook

In this thesis I examine the properties of UDG candidates in the cluster environment. The effect of redshift and the cluster environment on UDG candidate counts are also investigated. The techniques I have used can be easily applied to searching for UDG candidates uniformly in different extended source surveys.

There are several limitations in this study, which include the depth of the data and the number of clusters we were able to examine. To gain a better understanding of the impact the cluster environment has on galaxy formation requires a larger sample of clusters with deeper image depth. The larger data set will provide a cluster sample with a more varied cluster halo masses. Subsequently, the relationship between cluster halo mass and UDG candidate numbers can then be better studied for a larger range of cluster halo masses. A study including nearby clusters may also provide more detailed information on the evolutionary effects on individual galaxies. To understand the effect of redshift on the number of UDG candidates in clusters requires much deeper data. The low surface brightness of UDG candidates and the limited depth observable with current surveys, like SDSS, makes the study of faint high redshift sources very difficult. The Large Synoptic Survey Telescope (LSST) is currently being built in northern Chile (Ivezić et al., 2019) and will start operation in 2022. The primary mirror will have an effective size of 6.5m. The main project of the LSST is a deep-wide-fast photometric survey covering an 18,000 deg^2 region in the u,g,r,i,z and y bands. This survey is expected to reach a 5σ depth of 26.1, 27.4, 27.5, 26.8, 26.1 and 24.9 mags in the u, g, r, i, z and y respectively for point sources. This is $\sim$2 mags deeper than the corresponding bands in the deep IAC Stripe 82 data at 3σ. The deeper image depth of the LSST will allow for observations of fainter UDG candidates as well as candidates at higher redshifts.

Simulations of UDG formation indicate that internal processes are a major contributing factor in the formation and evolution of UDG candidates. Gas outflows in UDGs are expected to be caused by star formation and more specifically supernovae. The removal of the gas quenches the star formation and results in a passively evolving stellar population. These internal processes effect the formation of field UDGs, while environmental processes like stripping and tidal expansion probably affect UDGs within clusters as well.

Previous works have reported that UDGs avoid the central cluster region. In future, we can explore this in more depth by investigating the UDG density as a function of cluster radius. This will provide information on the preferred and avoided regions with respect to cluster radius. To understand the internal processes of UDGs requires observations of UDG candidates in the field. This can be done by investigating prospective nearby UDG candidates with spectroscopic and photometric measurements, to obtain morphological properties, metal abundances and their distances. This may provide an insight into their formation mechanisms and how they differ from cluster UDG candidates.

References

Abazajian K. N., et al., 2009, The Astrophysical Journal Supplement Series, 182, 543

Abraham R. G., van Dokkum P. G., 2014, Publications of the Astronomical Society of the Pacific, 126, 55

Aihara H., et al., 2011, The Astrophysical Journal Supplement Series, 193, 29

Amorisco N. C., Loeb A., 2016, mnras, 459, L51

Barnabè M., Czoske O., Koopmans L. V. E., Treu T., Bolton A. S., 2011, mnras, 415, 2215

Beasley M. A., Romanowsky A. J., Pota V., Navarro I. M., Martinez Delgado D., Neyer F., Deich A. L., 2016, apj, 819, L20

Bell E. F., McIntosh D. H., Katz N., Weinberg M. D., 2003, The Astrophysical Journal Supplement Series, 149, 289

Bellazzini M., Belokurov V., Magrini L., Fraternali F., Testa V., Beccari G., Marchetti A., Carini R., 2017, mnras, 467, 3751

Bennett C. L., et al., 2013, apjs, 208, 20

Berrier J. C., Stewart K. R., Bullock J. S., Purcell C. W., Barton E. J., Wechsler R. H., 2009, apj, 690, 1292

Bertin E., 2011, in Evans I. N., Accomazzi A., Mink D. J., Rots A. H., eds, Vol. 442, Astronomical Data Analysis Software and Systems XX. p. 435

Bertin E., Arnouts S., 1996, Astronomy and Astrophysics Supplement Series, 117, 393

Bertin E., Mellier Y., Radovich M., Missonnier G., Didelon P., Morin B., 2002, in Bohlender D. A., Durand D., Handley T. H., eds, Vol. 281, Astronomical Data Analysis Software and Systems XI. p. 228

Binggeli B., Sandage A., Tammann G. A., 1985, The Astronomical Journal, 90, 1681

Binney J., Tremaine S., 1987, Galactic dynamics

Bolton A. S., Burles S., Koopmans L. V. E., Treu T., Moustakas L. A., 2006, apj, 638, 703

Boylan-Kolchin M., Springel V., White S. D. M., Jenkins A., Lemson G., 2009, mnras, 398, 1150

Bruzual G., Charlot S., 2003, mnras, 344, 1000

Caon N., Capaccioli M., D'Onofrio M., 1993a, mnras, 265, 1013

Caon N., Capaccioli M., D'Onofrio M., 1993b, mnras, 265, 1013

Cappellari M., et al., 2011, mnras, 413, 813

Cappellari M., et al., 2013, mnras, 432, 1709

Carleton T., Errani R., Cooper M., Kaplinghat M., Peñarrubia J., Guo Y., 2019, mnras, 485, 382

Chan T. K., Kereš D., Wetzel A., Hopkins P. F., Faucher-Giguère C. A., El-Badry K., Garrison-Kimmel S., Boylan-Kolchin M., 2018, mnras, 478, 906

Chilingarian I. V., Zolotukhin I. Y., 2012, mnras, 419, 1727

Chilingarian I. V., Melchior A.-L., Zolotukhin I. Y., 2010, mnras, 405, 1409

Cohen Y., et al., 2018, apj, 868, 96

Conroy C., Gunn J. E., White M., 2009, apj, 699, 486

Conselice C. J., Wilkinson A., Duncan K., Mortlock A., 2016, apj, 830, 83

Courteau S., de Jong R. S., Broeils A. H., 1996, apjl, 457, L73

Danieli S., van Dokkum P., 2019, apj, 875, 155

Danieli S., van Dokkum P., Conroy C., Abraham R., Romanowsky A. J., 2019, apj, 874, L12

Di Cintio A., Brook C. B., Dutton A. A., Macciò A. V., Obreja A., Dekel A., 2017, mnras, 466, L1

Di Cintio A., Brook C. B. A., Dutton A. A., Macciò A. V., Obreja A., Dekel A., 2019, in Highlights on Spanish Astrophysics X. pp 116–121

Dressler A., 1980, apj, 236, 351

Dressler A., 1986, apj, 301, 35

Erwin P., 2014, Imfit: A Fast, Flexible Program for Astronomical Image Fitting (ascl:1408.001)

Evrard A. E., et al., 2008, apj, 672, 122

Ferrarese L., Merritt D., 2000, apjl, 539, L9

Fliri J., Trujillo I., 2016, mnras, 456, 1359

Gallagher John S. I., Hunter D. A., 1984, araa, 22, 37

Gallagher J. S. I., Hunter D. A., Tutukov A. V., 1984, apj, 284, 544

Gao L., Navarro J. F., Frenk C. S., Jenkins A., Springel V., White S. D. M., 2012, mnras, 425, 2169

Geach J. E., Murphy D. N. A., Bower R. G., 2011, mnras, 413, 3059

Gladders M. D., Yee H. K. C., 2000, aj, 120, 2148

Haines C. P., et al., 2013, apj, 775, 126

Hubble E. P., 1926, apj, 64, 321

Hubble Classification 2016, Hubble's Galaxy Classification Scheme, http://astro.physics.uiowa.edu/ITU/labs/foundational-labs/classifying-galaxies/part-1-hubbles-tuning-fork.html

Impey C., Bothun G., 1997, araa, 35, 267

Ivezić Ž., et al., 2019, apj, 873, 111

Janssens S., Abraham R., Brodie J., Forbes D., Romanowsky A. J., van Dokkum P., 2017, apj, 839, L17

Jiang F., Dekel A., Freundlich J., Romanowsky A. J., Dutton A. A., Macciò A. V., Di Cintio A., 2019, mnras, 487, 5272

Kauffmann G., et al., 2003, mnras, 341, 33

Kirby E. N., Cohen J. G., Guhathakurta P., Cheng L., Bullock J. S., Gallazzi A., 2013, apj, 779, 102

Koda J., Yagi M., Yamanoi H., Komiyama Y., 2015, apj, 807, L2

Kormendy J., 1977, apj, 218, 333

Kraan-Korteweg R. C., Tammann G. A., 1979, Astronomische Nachrichten, 300, 181

Lee M. G., Kang J., Lee J. H., Jang I. S., 2017, apj, 844, 157

Liddle A. R., Lyth D. H., 2000, Cosmological Inflation and Large-Scale Structure

Lintott C. J., et al., 2008, mnras, 389, 1179

Lotz J. M., et al., 2017, apj, 837, 97

Lupton R., 2005, Transformations between SDSS magnitudes and other systems, https://www.sdss.org/dr13/algorithms/sdssUBVRITransform/#Lupton2005

Martínez-Delgado D., et al., 2016, aj, 151, 96

McConnachie A. W., 2012, aj, 144, 4

Messier C., 1781, Technical report, Catalogue des Nébuleuses et des Amas d'Étoiles (Catalog of Nebulae and Star Clusters)

Mihos J. C., et al., 2015, apj, 809, L21

Moore B., Katz N., Lake G., Dressler A., Oemler A., 1996, nat, 379, 613

Moore B., Lake G., Katz N., 1998, apj, 495, 139

Muñoz R. P., et al., 2015, apjl, 813, L15

NASA/WMAP 2012, Timeline of the Universe, https://map.gsfc.nasa.gov/media/060915/index.html

Navarro J. F., Frenk C. S., White S. D. M., 1996, apj, 462, 563

Nelson D., et al., 2018, mnras, 475, 624

O'Neil K., Bothun G. D., Cornell M. E., 1997a, The Astronomical Journal, 113, 1212

O'Neil K., Bothun G. D., Schombert J., Cornell M. E., Impey C. D., 1997b, The Astronomical Journal, 114, 2448

Okabe N., Futamase T., Kajisawa M., Kuroshima R., 2014, apj, 784, 90

Opik E., 1922, apj, 55, 406

Patterson R. J., Thuan T. X., 1996, apjs, 107, 103

Pedregosa F., et al., 2011, Journal of Machine Learning Research, 12, 2825

Peebles P. J. E., 1980, The large-scale structure of the universe

Peebles P. J., Ratra B., 2003, Reviews of Modern Physics, 75, 559

Peng C. Y., Ho L. C., Impey C. D., Rix H.-W., 2002, aj, 124, 266

Peng C. Y., Ho L. C., Impey C. D., Rix H.-W., 2010, aj, 139, 2097

Persic M., Salucci P., Stel F., 1996, mnras, 283, 1102

Popesso P., Biviano A., Böhringer H., Romaniello M., Voges W., 2005, aap, 433, 431

Press W. H., Schechter P., 1974, apj, 187, 425

Prugniel P., Simien F., 1996, aap, 309, 749

Ratra B., Vogeley M. S., 2008, pasp, 120, 235

Riess A. G., et al., 2016, apj, 826, 56

Román J., Trujillo I., 2017a, mnras, 468, 703

Román J., Trujillo I., 2017b, mnras, 468, 4039

Rong Y., Guo Q., Gao L., Liao S., Xie L., Puzia T. H., Sun S., Pan J., 2017, mnras, 470, 4231

Rubin V. C., Ford W. K. J., Thonnard N., 1978, apjl, 225, L107

Rubin V. C., Ford W. K. J., Thonnard N., 1980, apj, 238, 471

Rubin V. C., Burstein D., Ford W. K. J., Thonnard N., 1985, apj, 289, 81

Ruiz-Lara T., et al., 2018, mnras, 478, 2034

Rykoff E. S., et al., 2012, apj, 746, 178

Rykoff E. S., et al., 2014, apj, 785, 104

Sand D. J., et al., 2011, apj, 729, 142

Schlafly E. F., Finkbeiner D. P., 2011, apj, 737, 103

Sérsic J. L., 1963, Boletin de la Asociacion Argentina de Astronomia La Plata Argentina, 6, 41

Sersic J. L., 1968, Atlas de Galaxias Australes

Shu F. H., 1970a, apj, 160, 89

Shu F. H., 1970b, apj, 160, 99

Shu F. H., Stachnik R. V., Yost J. C., 1971, apj, 166, 465

Sifón C., Hoekstra H., Cacciato M., Viola M., Köhlinger F., van der Burg R. F. J., Sand D. J., Graham M. L., 2015, aap, 575, A48

Sifón C., van der Burg R. F. J., Hoekstra H., Muzzin A., Herbonnet R., 2018, mnras, 473, 3747

Simet M., McClintock T., Mandelbaum R., Rozo E., Rykoff E., Sheldon E., Wechsler R. H., 2018, mnras, 480, 5385

Skrutskie M. F., et al., 2006, aj, 131, 1163

Spergel D. N., et al., 2003, apjs, 148, 175

Stetson P. B., 1987, Publications of the Astronomical Society of the Pacific, 99, 191

Tammann G. A., 1980, in Tarenghi M., Kjaer K., eds, ESA Workshop on Dwarf Galaxies. p. 3

Taylor E. N., et al., 2011, mnras, 418, 1587

Tonnesen S., Bryan G. L., van Gorkom J. H., 2007, apj, 671, 1434

Toomre A., 1977, araa, 15, 437

Tortora C., Napolitano N. R., Romanowsky A. J., Capaccioli M., Covone G., 2009, mnras, 396, 1132

Tremaine S., et al., 2002, apj, 574, 740

Trujillo I., Roman J., Filho M., Sánchez Almeida J., 2017a, apj, 836, 191

Trujillo I., Roman J., Filho M., Sánchez Almeida J., 2017b, apj, 836, 191

Tully R. B., Fisher J. R., 1977, aap, 500, 105

Van Rossum G., Drake Jr F. L., 1995, Python tutorial. Centrum voor Wiskunde en Informatica Amsterdam, The Netherlands

Vazdekis A., et al., 2015, mnras, 449, 1177

Venhola A., et al., 2017, aap, 608, A142

Wang L., Dutton A. A., Stinson G. S., Macciò A. V., Penzo C., Kang X., Keller B. W., Wadsley J., 2015, mnras, 454, 83

White S. D. M., Rees M. J., 1978, mnras, 183, 341

Yagi M., Koda J., Komiyama Y., Yamanoi H., 2016, The Astrophysical Journal Supplement Series, 225, 11

Yegorova I. A., Salucci P., 2007, mnras, 377, 507

York D. G., et al., 2000, aj, 120, 1579

Yozin C., Bekki K., 2015, mnras, 452, 937

de Vaucouleurs G., 1959, Handbuch der Physik, 53, 275

van Dokkum P. G., Abraham R., Merritt A., Zhang J., Geha M., Conroy C., 2015, apj, 798, L45

van Dokkum P., et al., 2018, nat, 555, 629

van den Bergh S., 1959, Publications of the David Dunlap Observatory, 2, 147

van der Burg R. F. J., Muzzin A., Hoekstra H., 2016, aap, 590, A20

van der Burg R. F. J., et al., 2017, aap, 607, A79

van der Hulst J. M., Skillman E. D., Smith T. R., Bothun G. D., McGaugh S. S., de Blok W. J. G., 1993, aj, 106, 548

Chapter 5

Appendix

5.1 Cluster Red Sequences

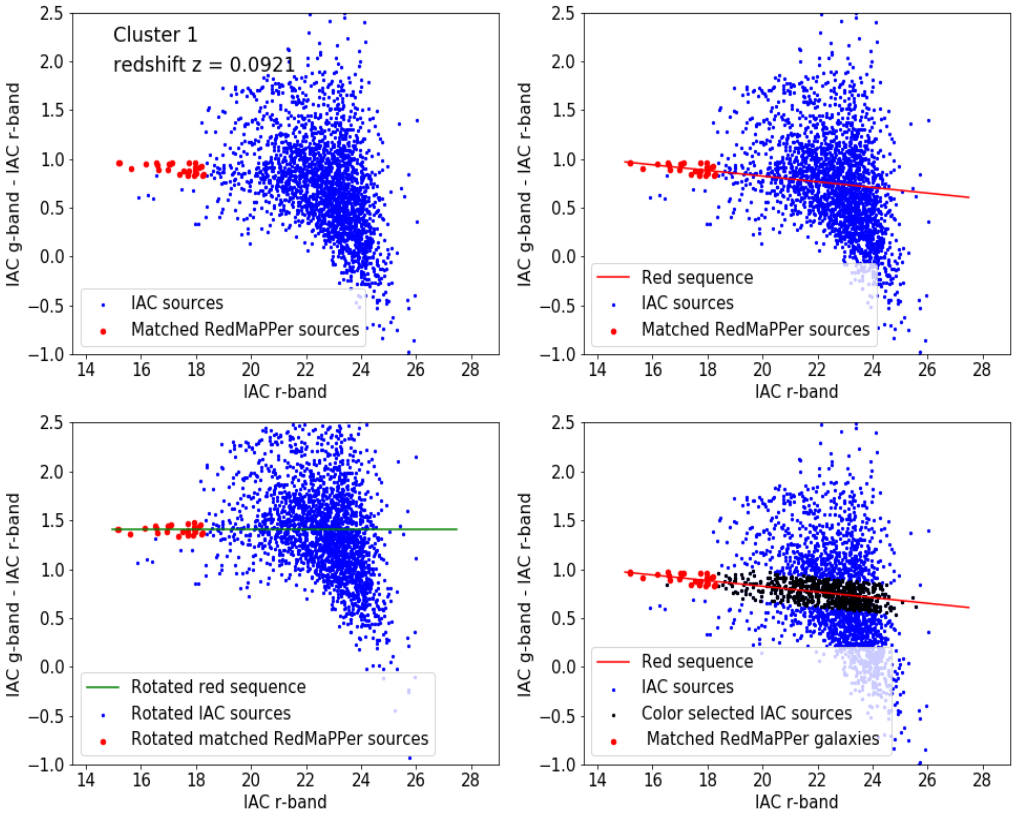

Figure 5.1: Sources in cluster 1. The red dots indicate galaxies utilized by RedMaPPer in their cluster identification (Rykoff et al., 2014). The blue dots are all the sources within the r_{200m} radius of the cluster from the deeper IAC catalogue (Fliri & Trujillo, 2016). The top-left panel displays the distribution of $g-r$ colour as a function of r-band magnitude. The top-right panel shows the red sequence identified by the red line. The bottom-left displays all the data rotated to the horizontal with the red sequence identified by green line. The bottom-right panel displays the all the sources identified as cluster members by the red sequence in black.

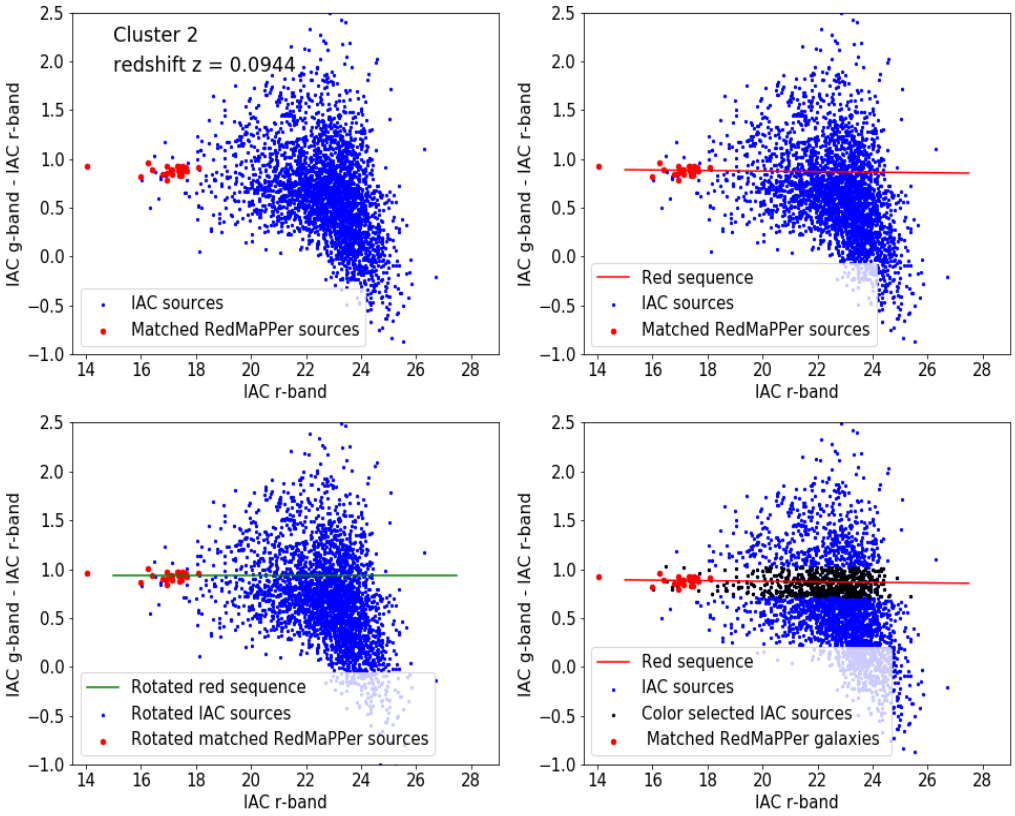

Figure 5.2: (Continued) Same as above for Sources in cluster 2.

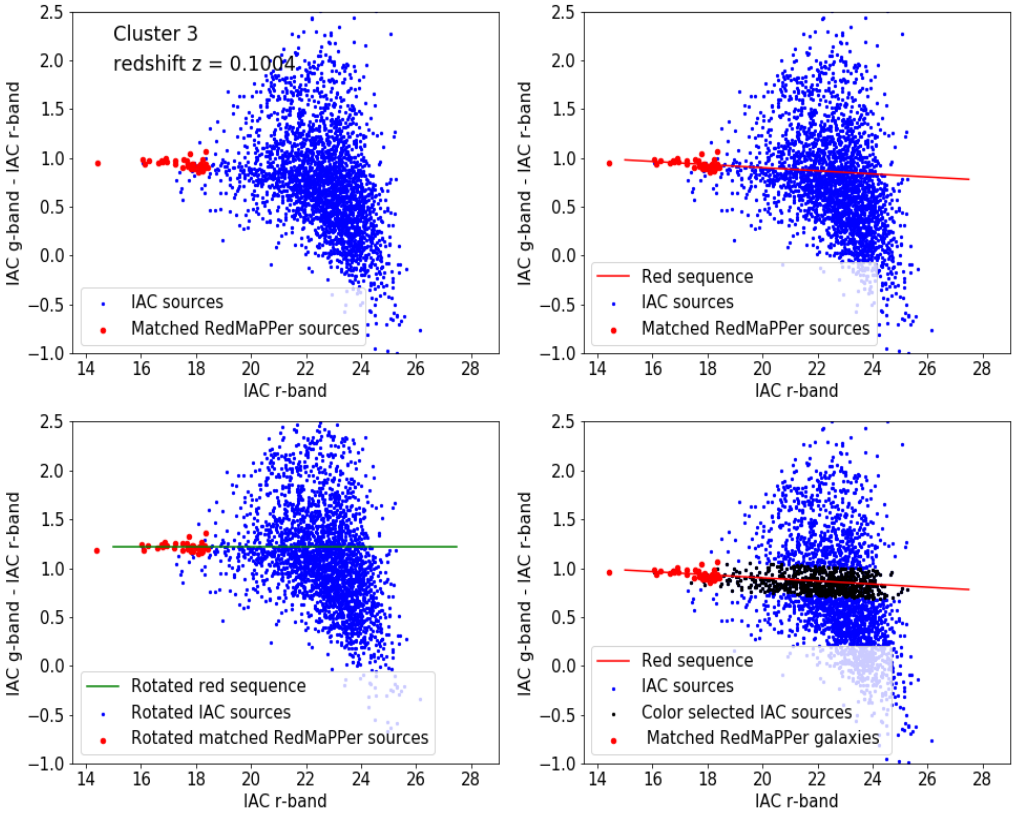

Figure 5.3: (Continued) Same as above for Sources in cluster 3.

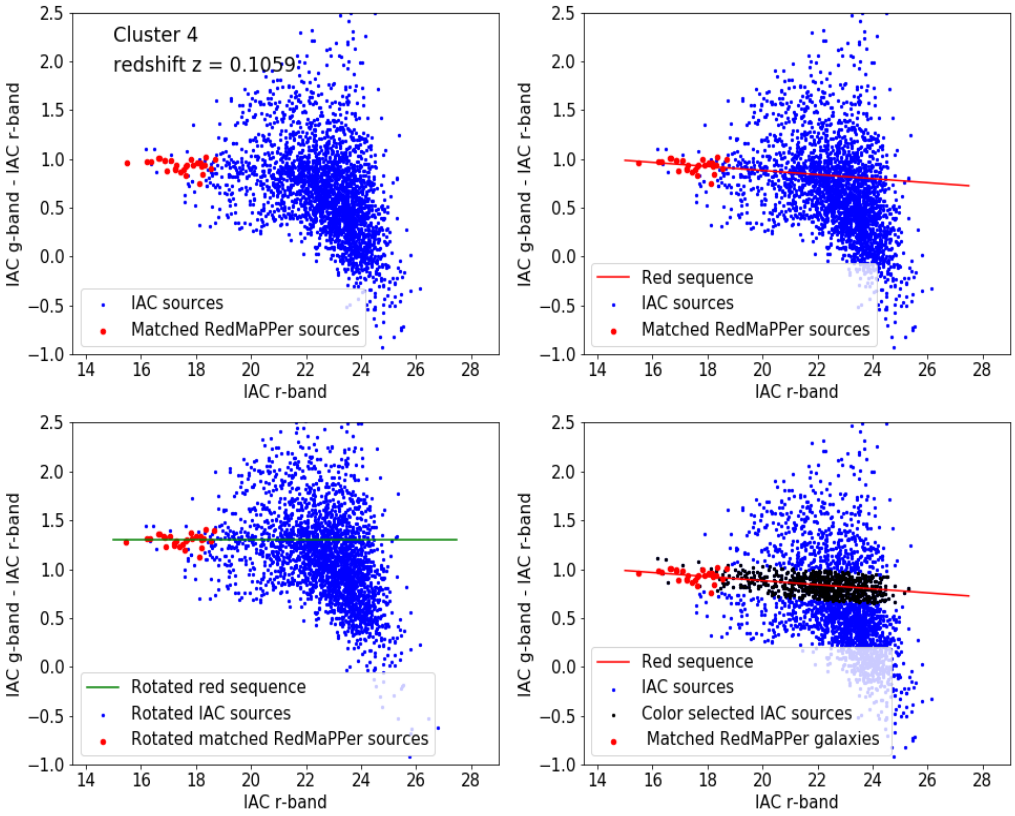

Figure 5.4: (Continued) Same as above for Sources in cluster 4.

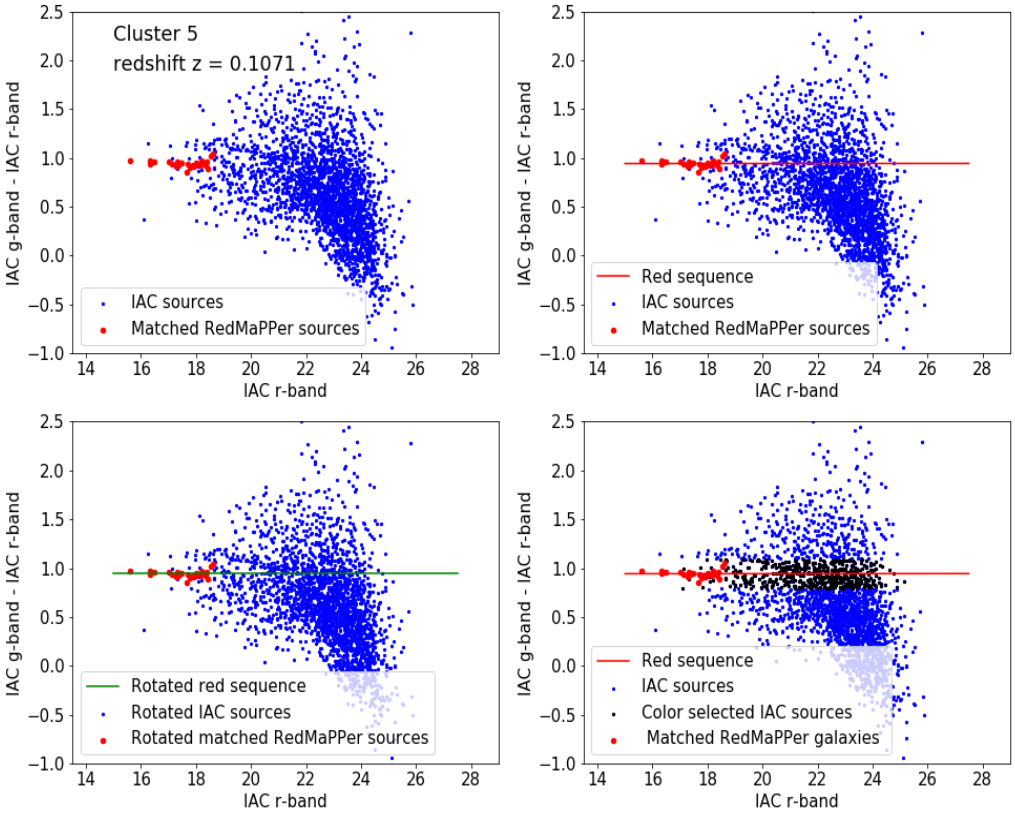

Figure 5.5: (Continued) Same as above for Sources in cluster 5.

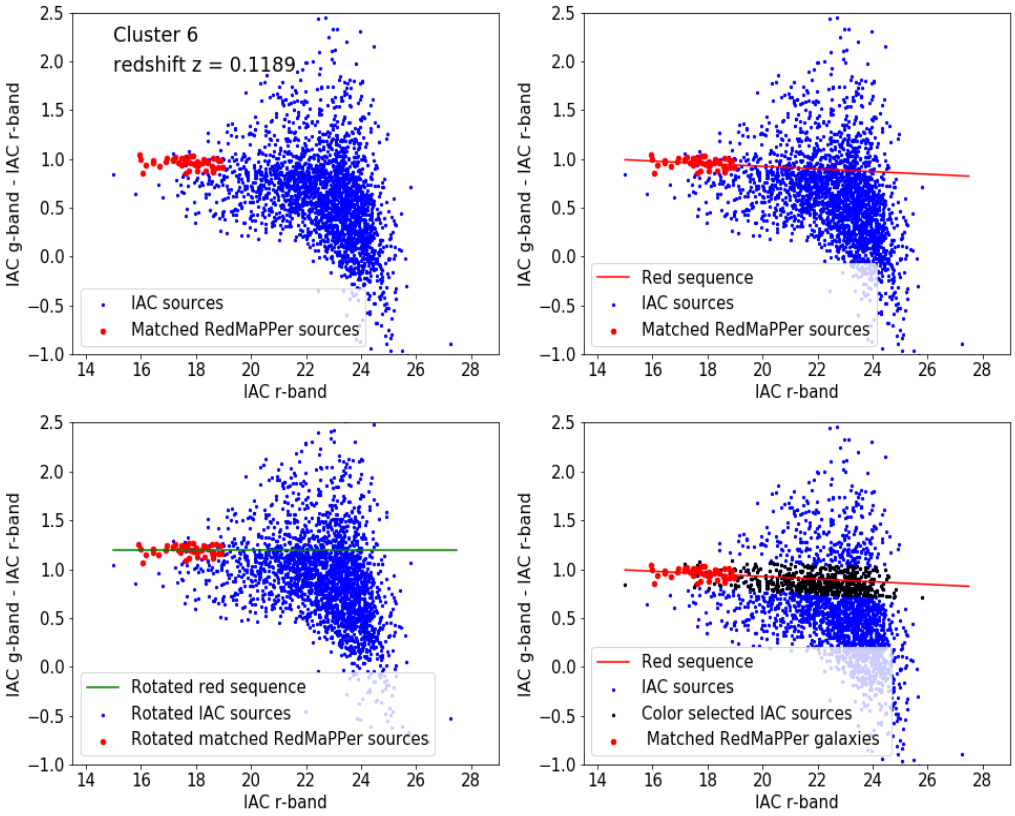

Figure 5.6: (Continued) Same as above for Sources in cluster 6.

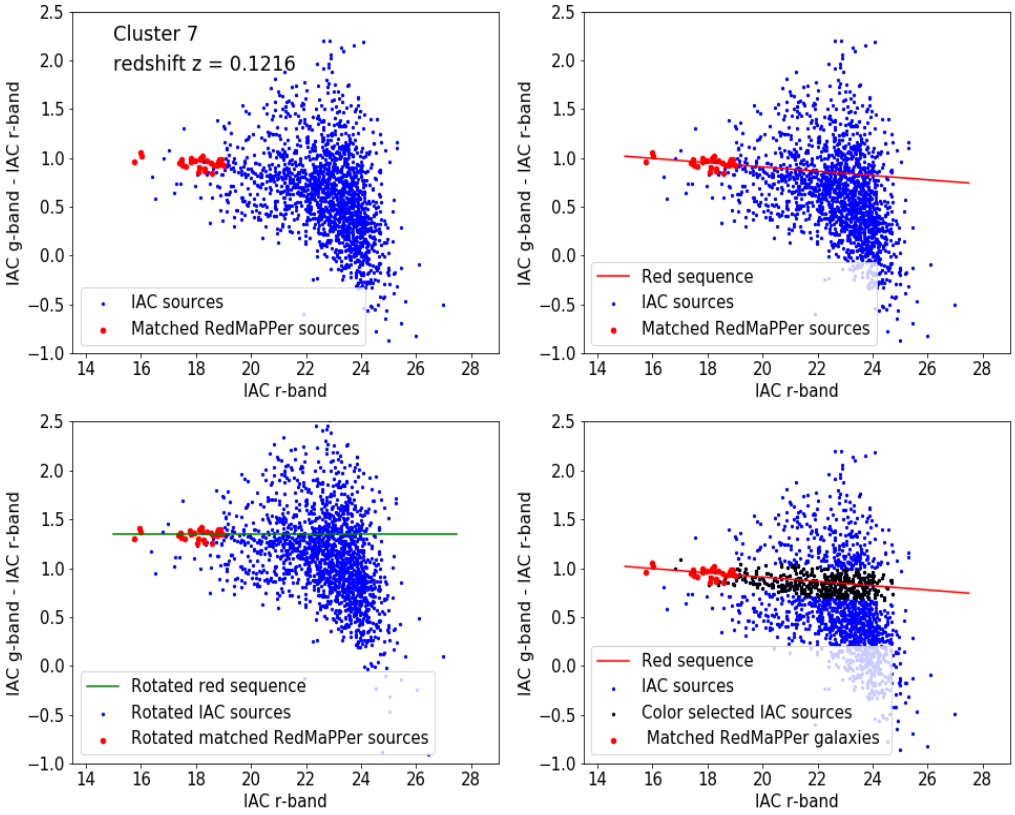

Figure 5.7: (Continued) Same as above for Sources in cluster 7.

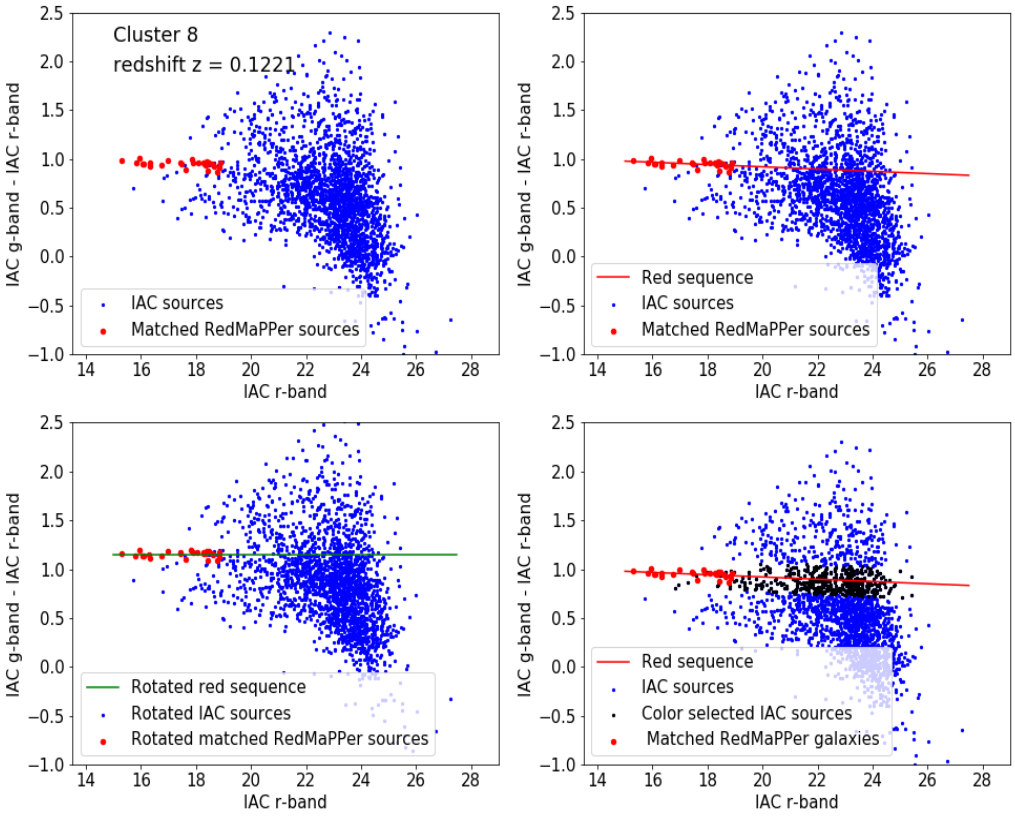

Figure 5.8: (Continued) Same as above for Sources in cluster 8.

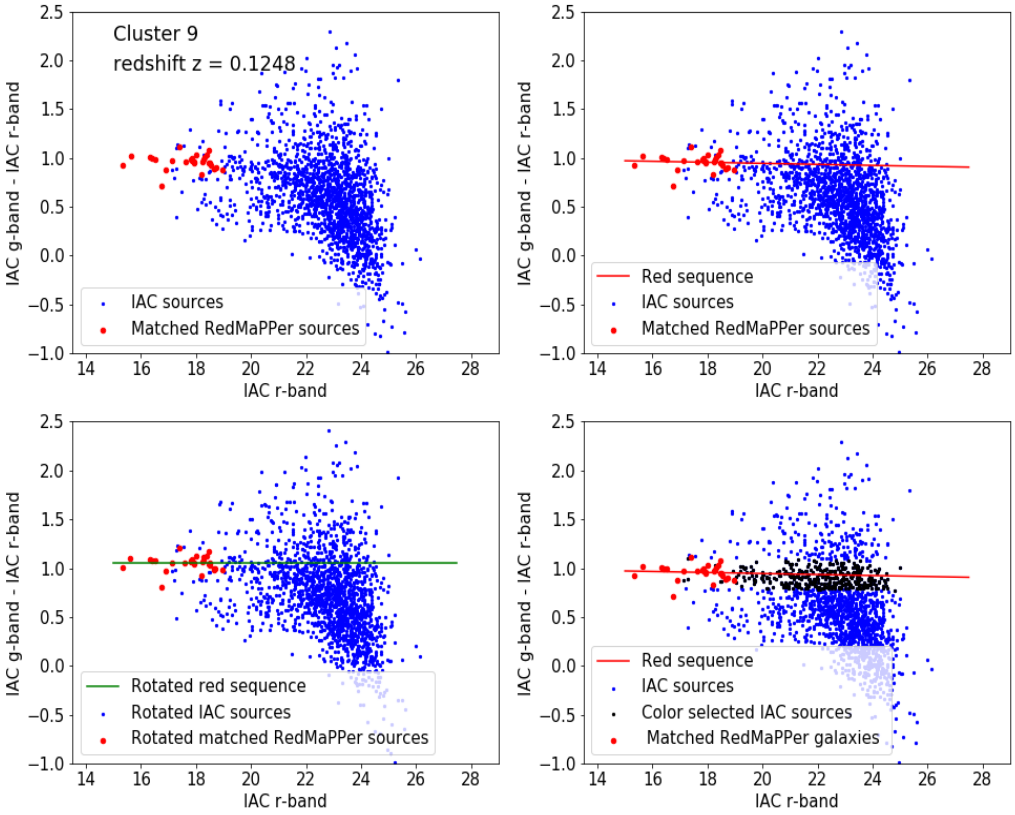

Figure 5.9: (Continued) Same as above for Sources in cluster 9.

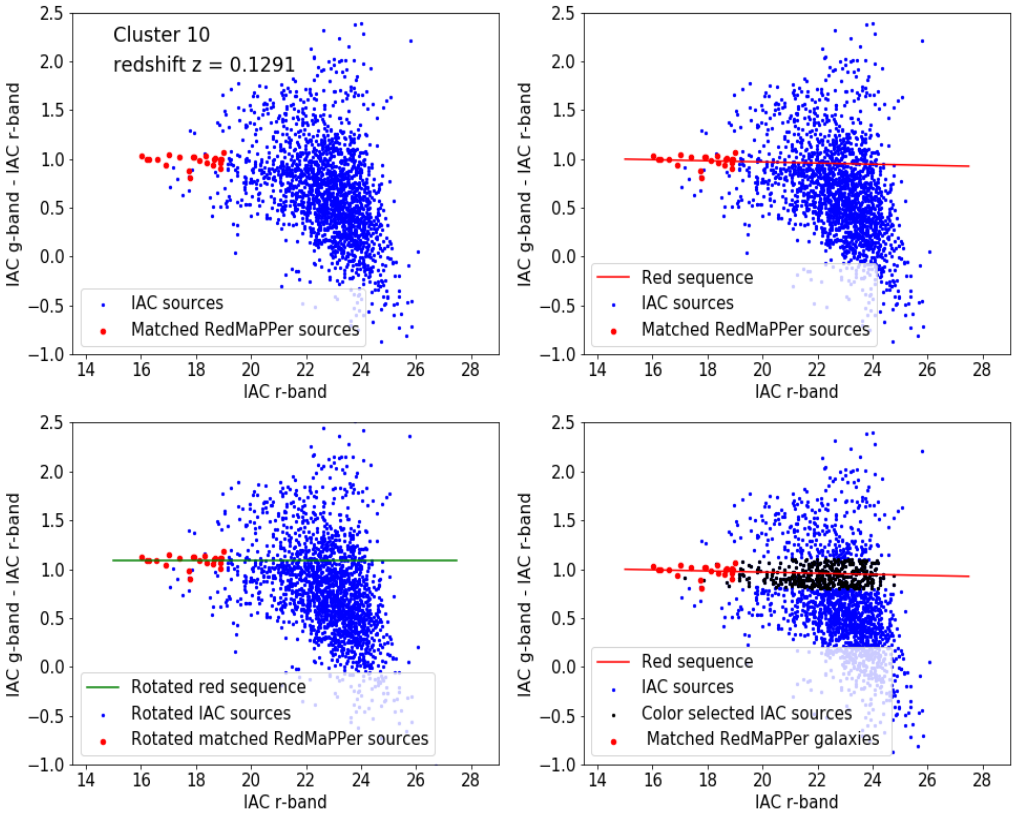

Figure 5.10: (Continued) Same as above for Sources in cluster 10.

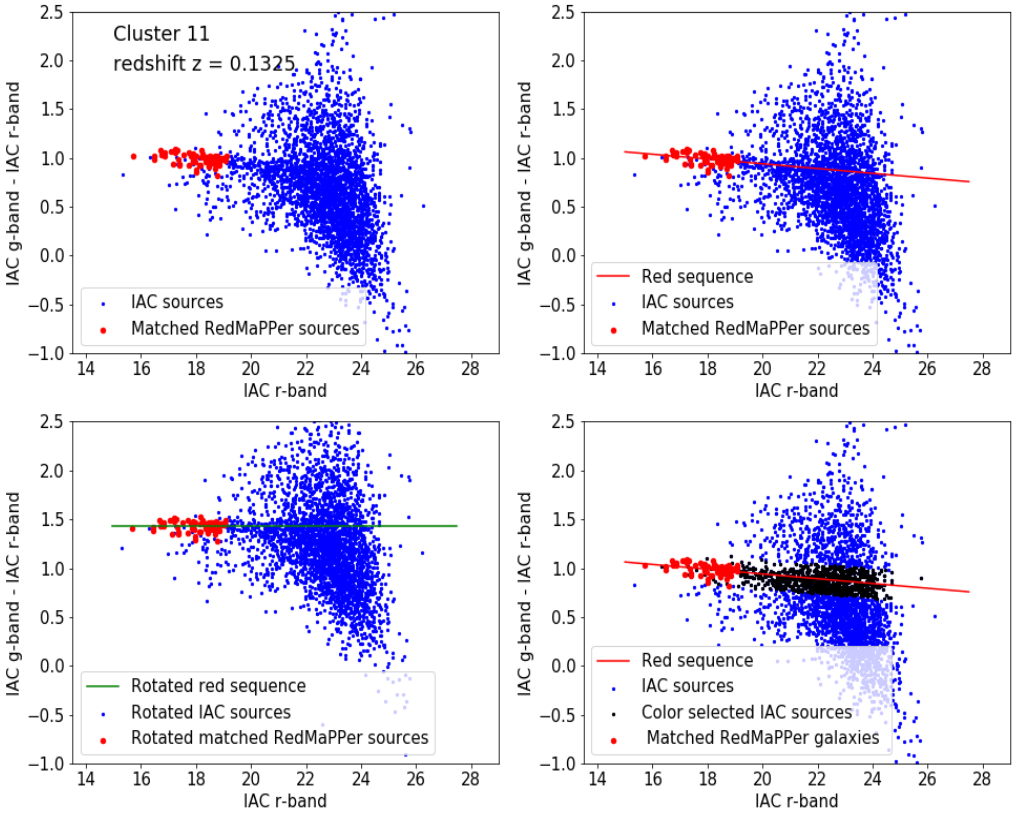

Figure 5.11: (Continued) Same as above for Sources in cluster 11.

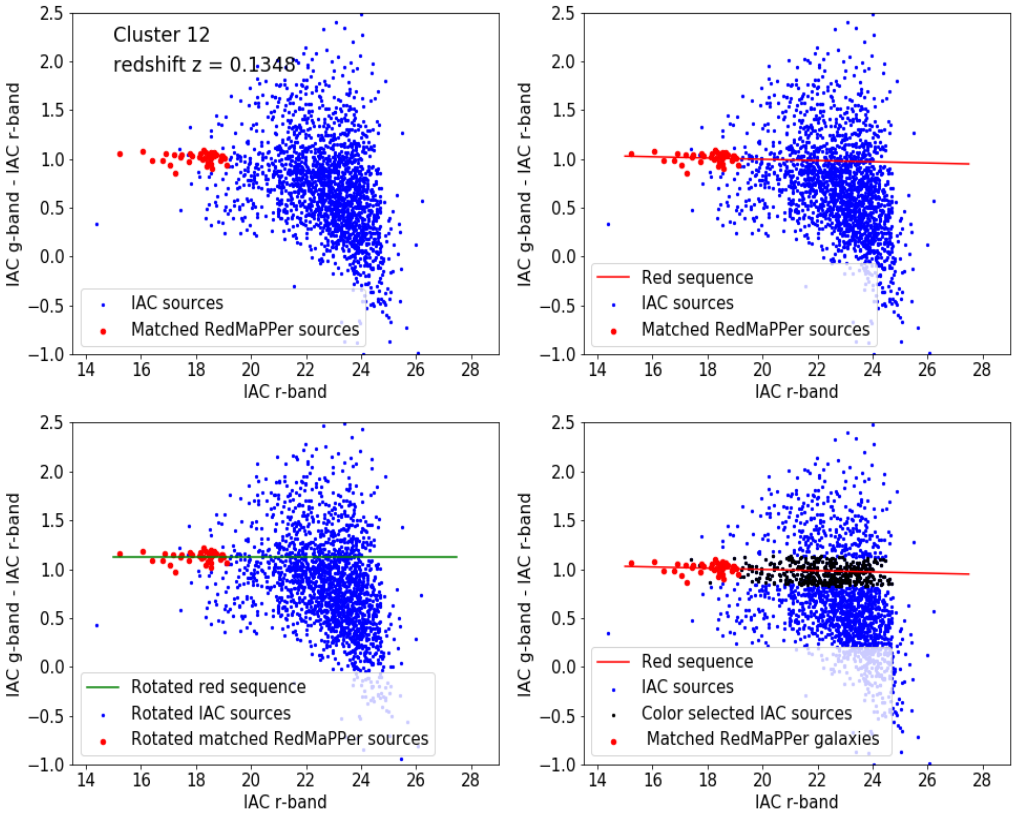

Figure 5.12: (Continued) Same as above for Sources in cluster 12.

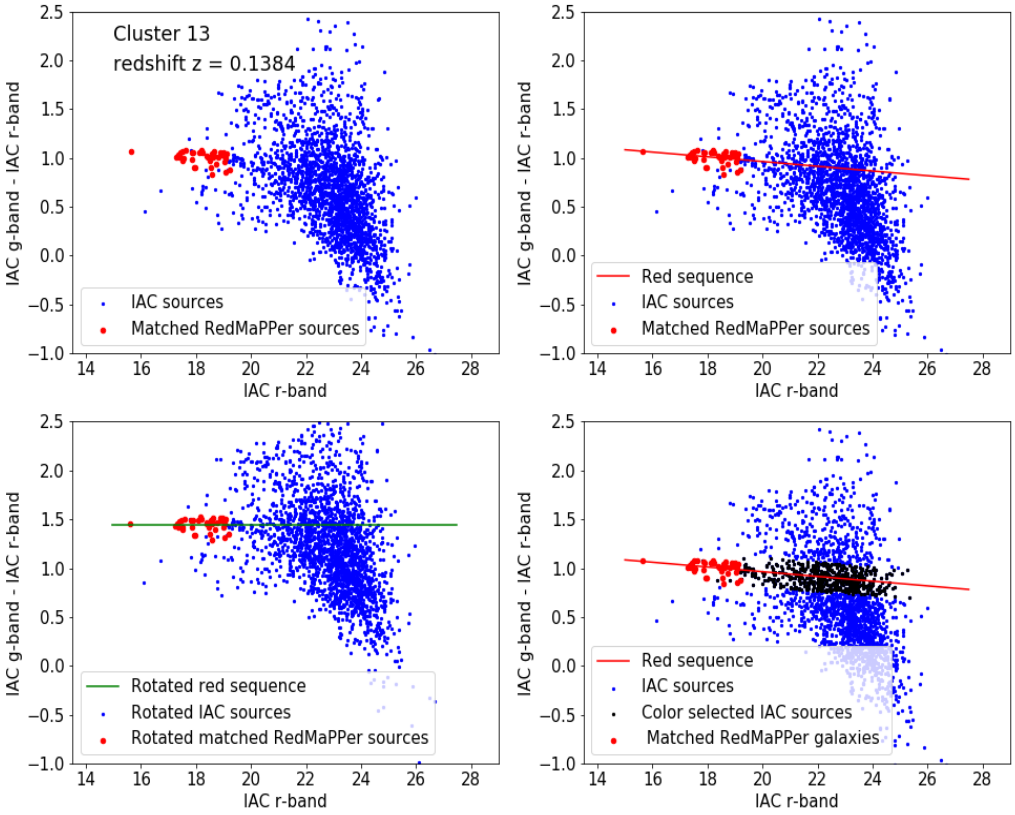

Figure 5.13: (Continued) Same as above for Sources in cluster 13.

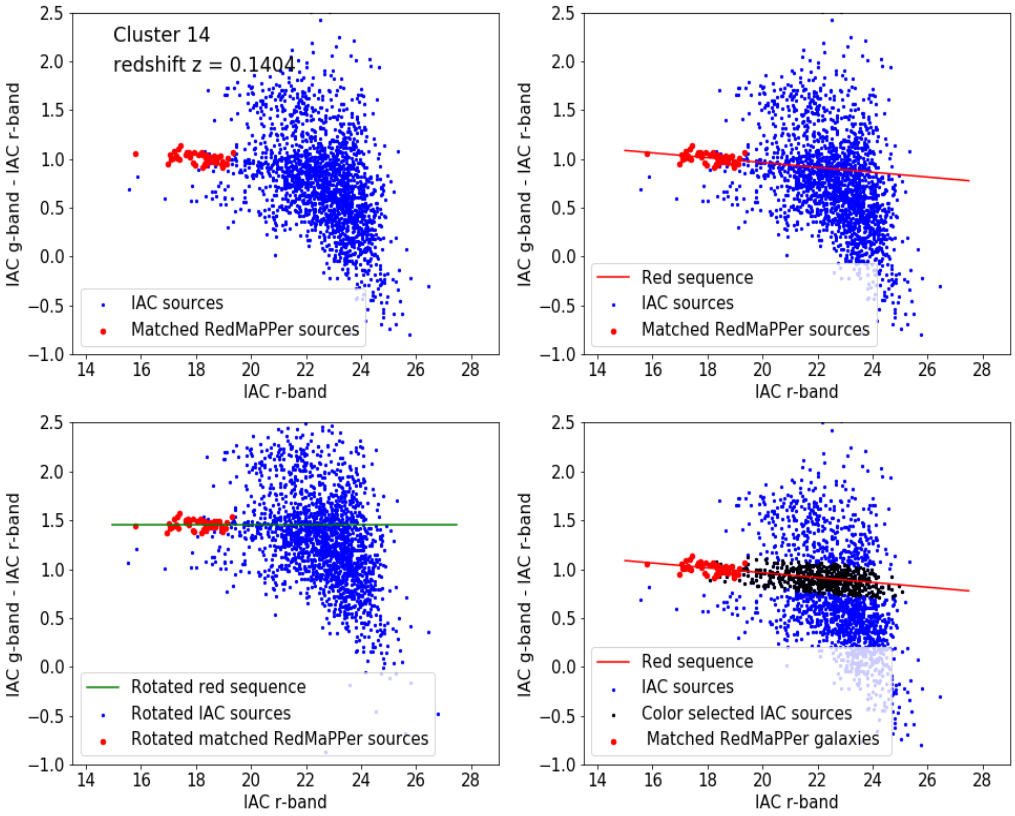

Figure 5.14: (Continued) Same as above for Sources in cluster 14.

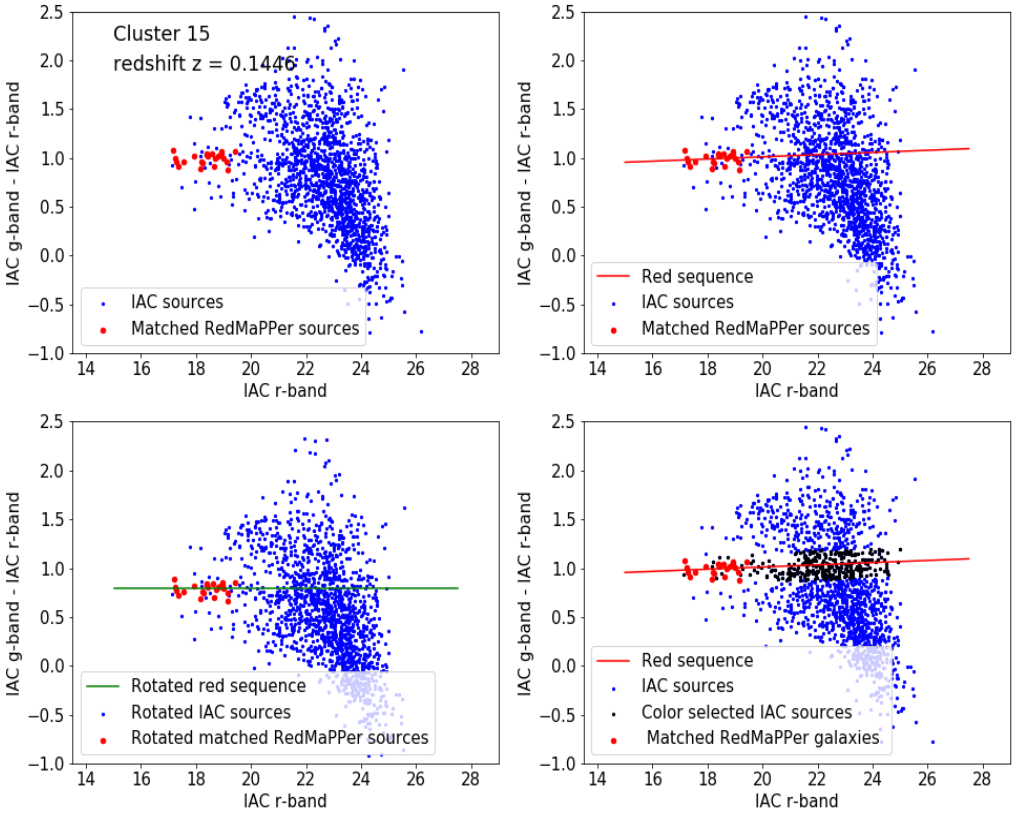

Figure 5.15: (Continued) Same as above for Sources in cluster 15.

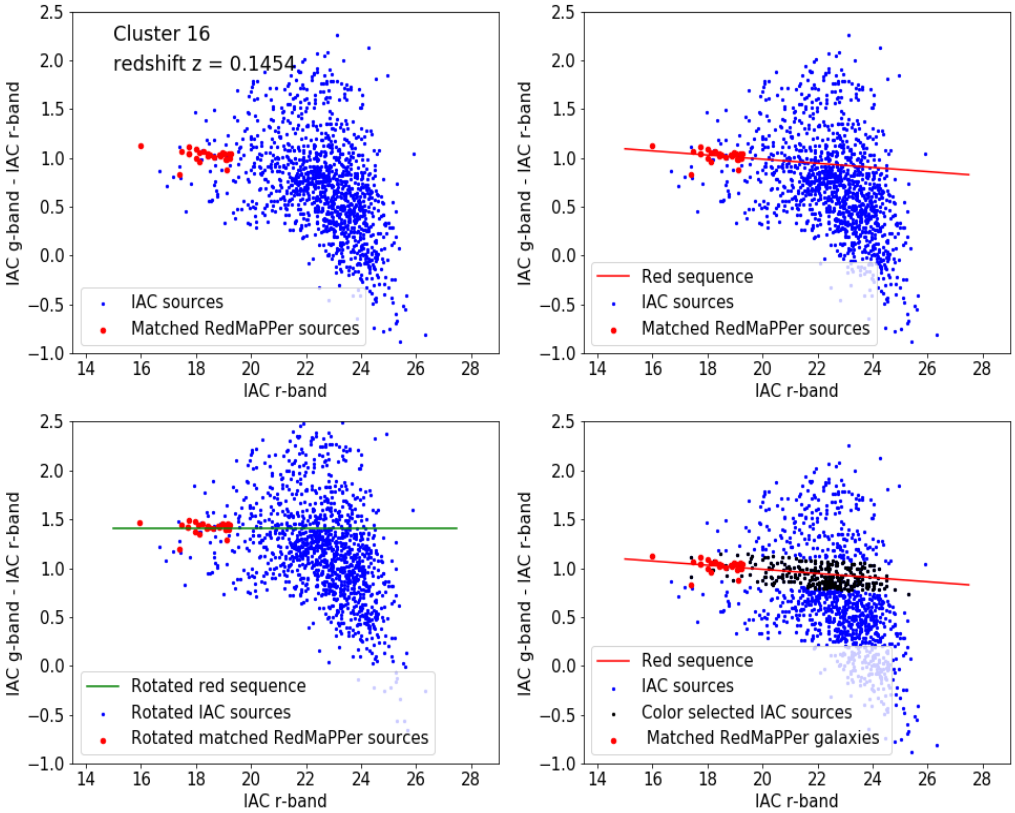

Figure 5.16: (Continued) Same as above for Sources in cluster 16.

5.2 GALFIT Model Properties, Before and After UDG Candidate Selection.

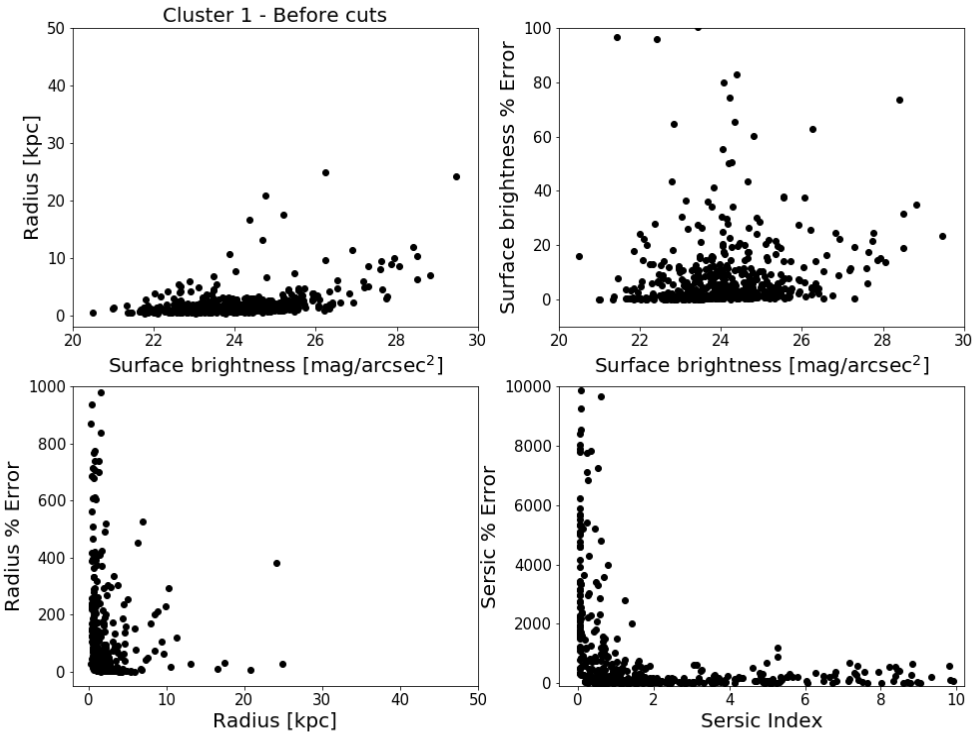

Figure 5.17: Four panel plot containing the dense region of all sources in cluster 1 modelled by GALFIT.

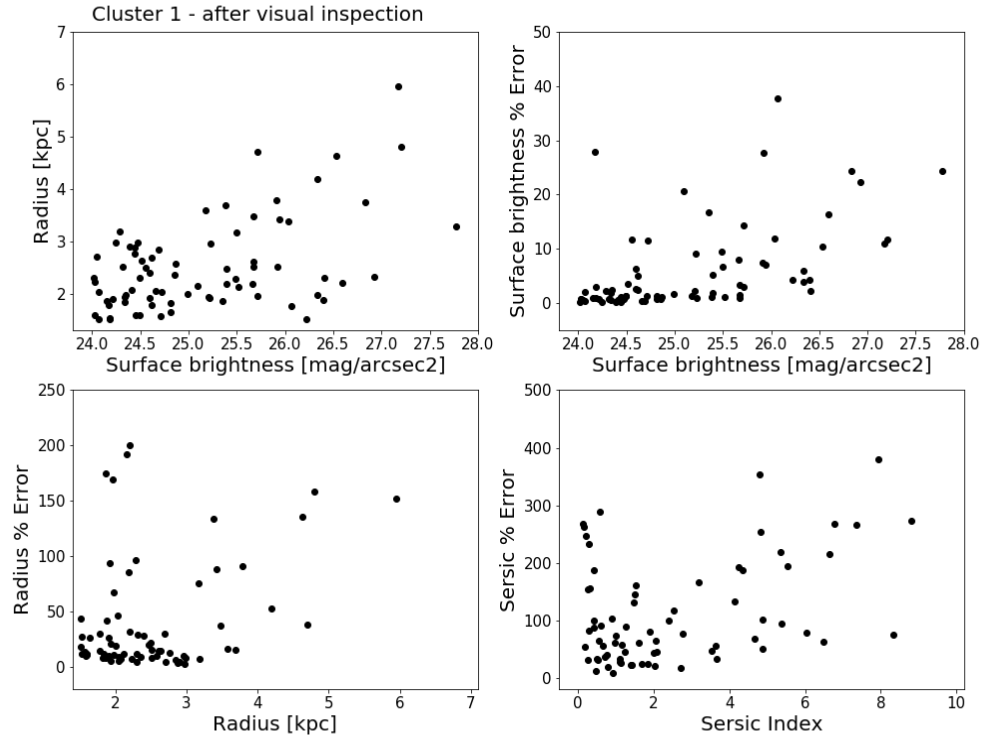

Figure 5.18: Four panel plot of the remaining sources in cluster 1 after applying the Sérsic index, radius, surface brightness cuts and visually inspection.

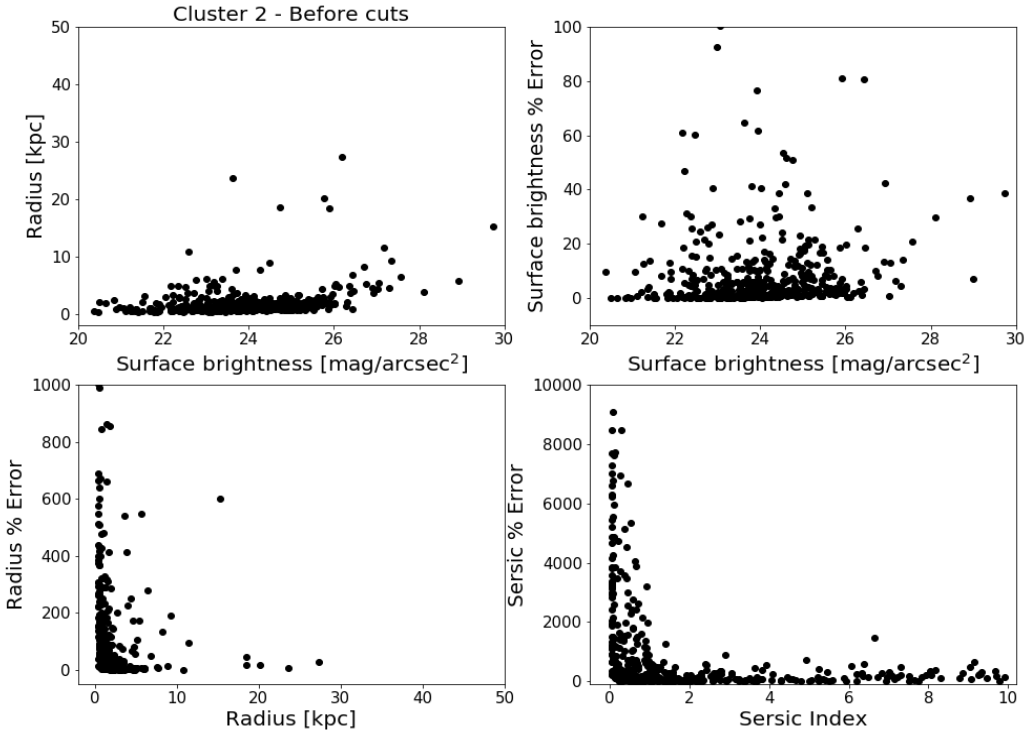

Figure 5.19: Four panel plot containing the dense region of all sources in cluster 2 modelled by GALFIT.

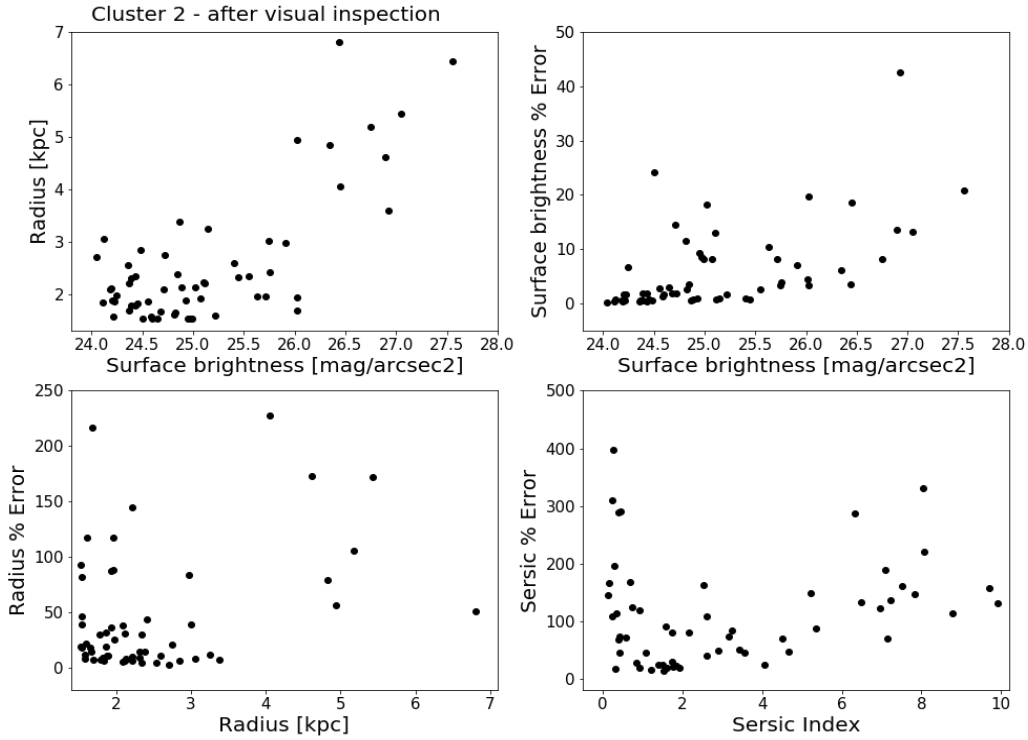

Figure 5.20: Four panel plot of the remaining sources in cluster 2 after applying the Sérsic index, radius, surface brightness cuts and visually inspection.

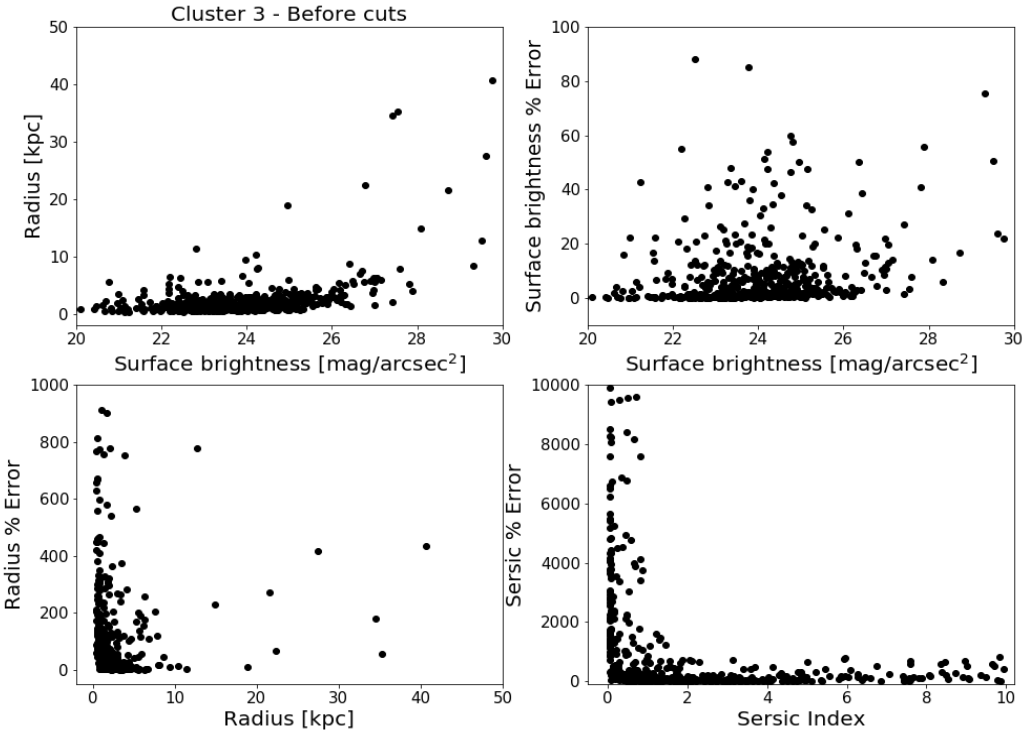

Figure 5.21: Four panel plot containing the dense region of all sources in cluster 3 modelled by GALFIT.

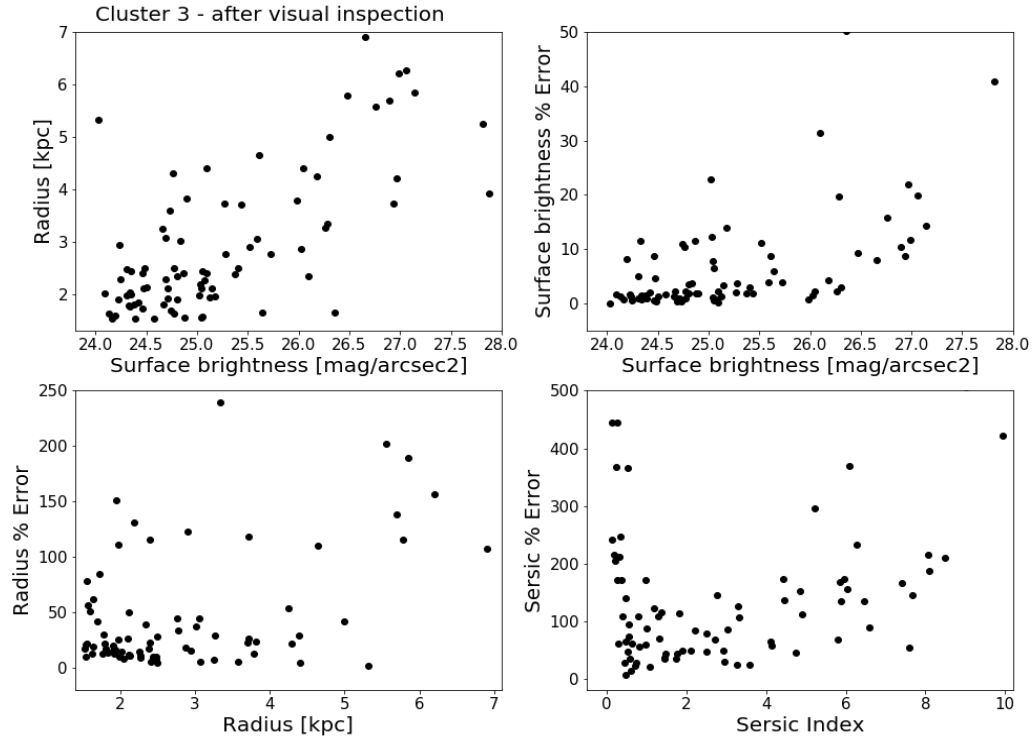

Figure 5.22: Four panel plot of the remaining sources in cluster 3 after applying the Sérsic index, radius, surface brightness cuts and visually inspection.

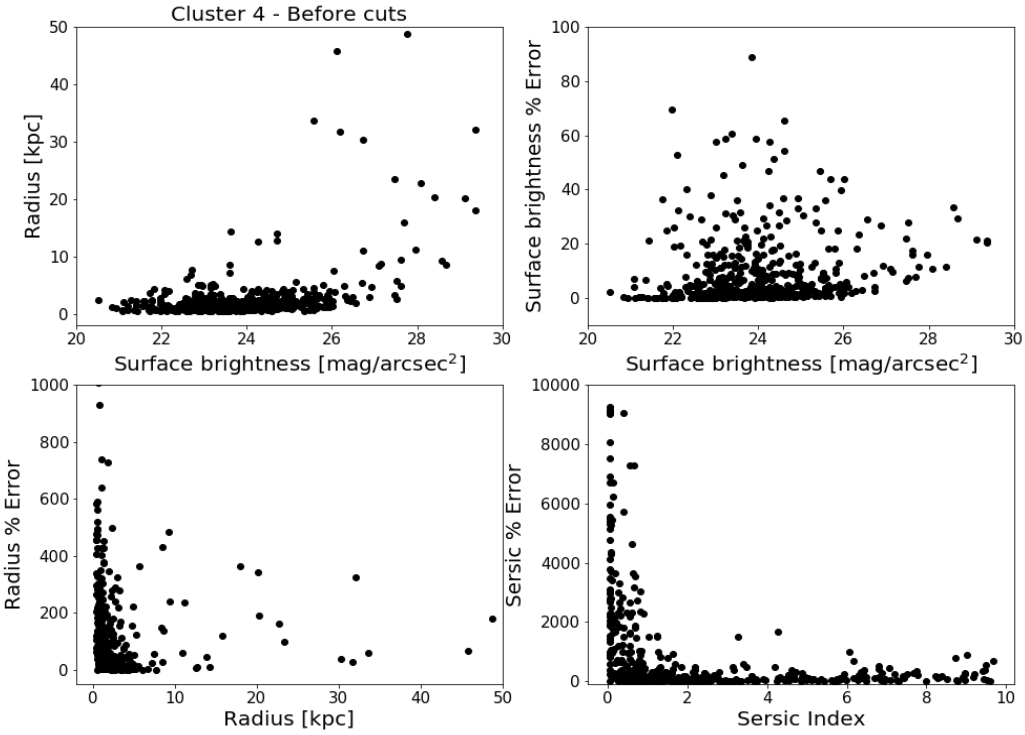

Figure 5.23: Four panel plot containing the dense region of all sources in cluster 4 modelled by GALFIT.

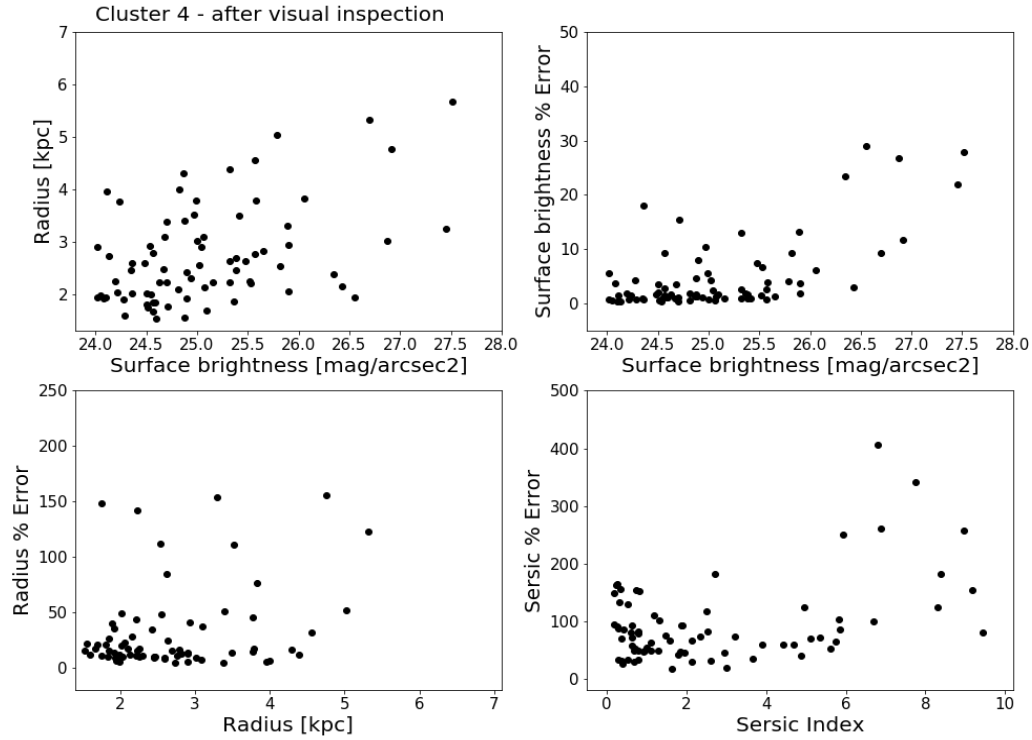

Figure 5.24: Four panel plot of the remaining sources in cluster 4 after applying the Sérsic index, radius, surface brightness cuts and visually inspection.

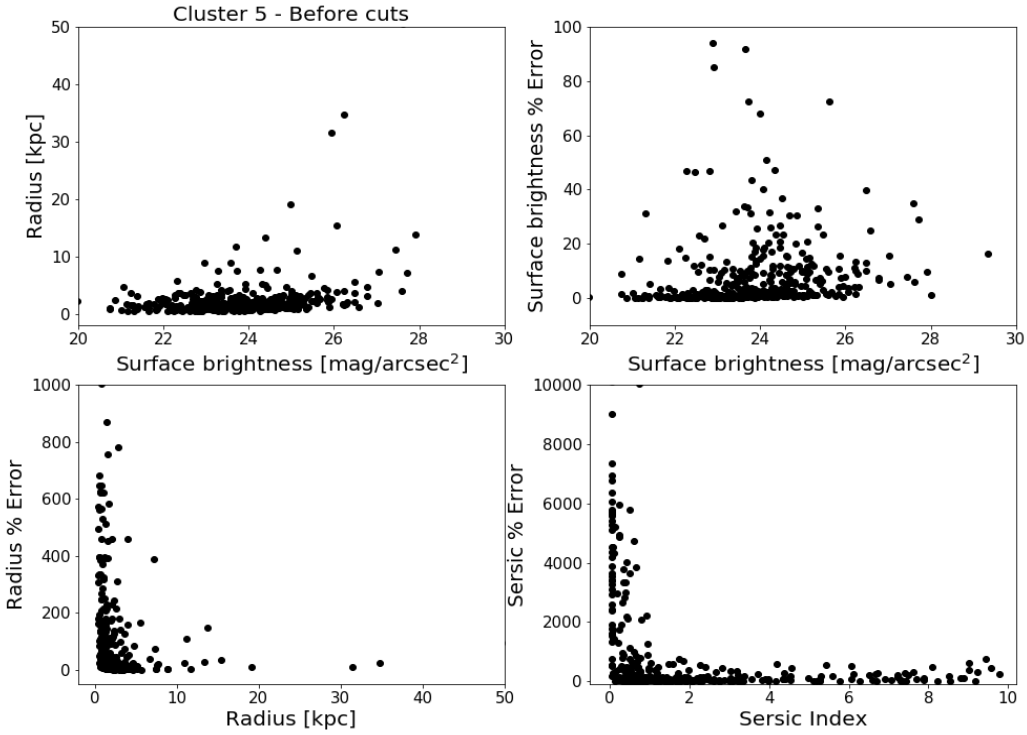

Figure 5.25: Four panel plot containing the dense region of all sources in cluster 5 modelled by GALFIT.

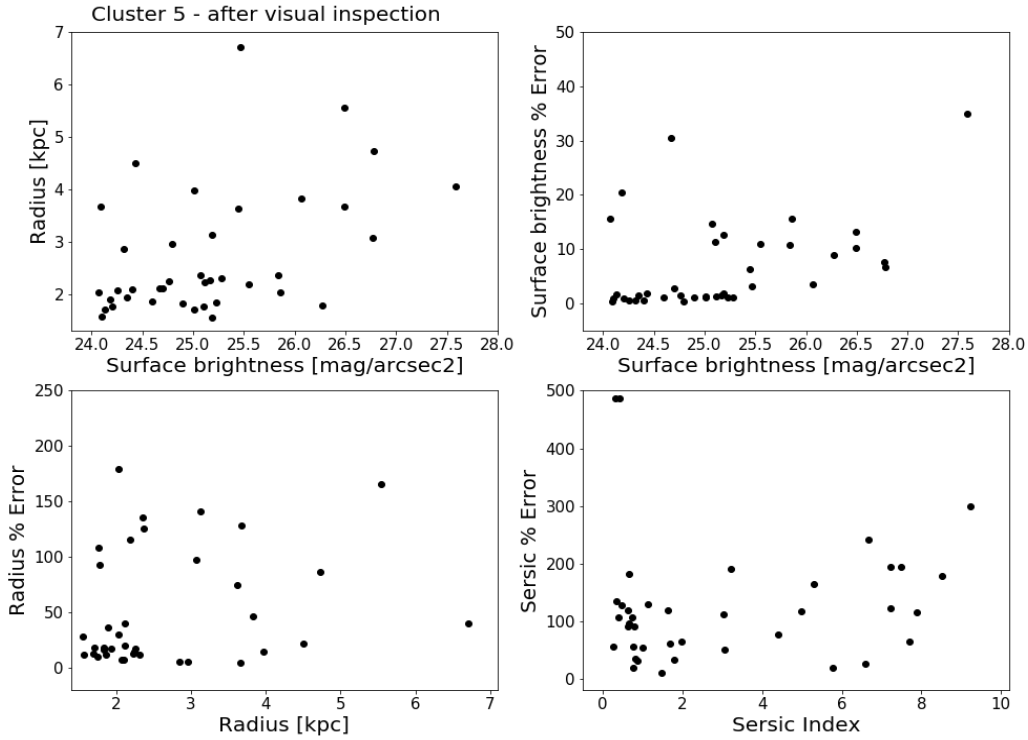

Figure 5.26: Four panel plot of the remaining sources in cluster 5 after applying the Sérsic index, radius, surface brightness cuts and visually inspection.

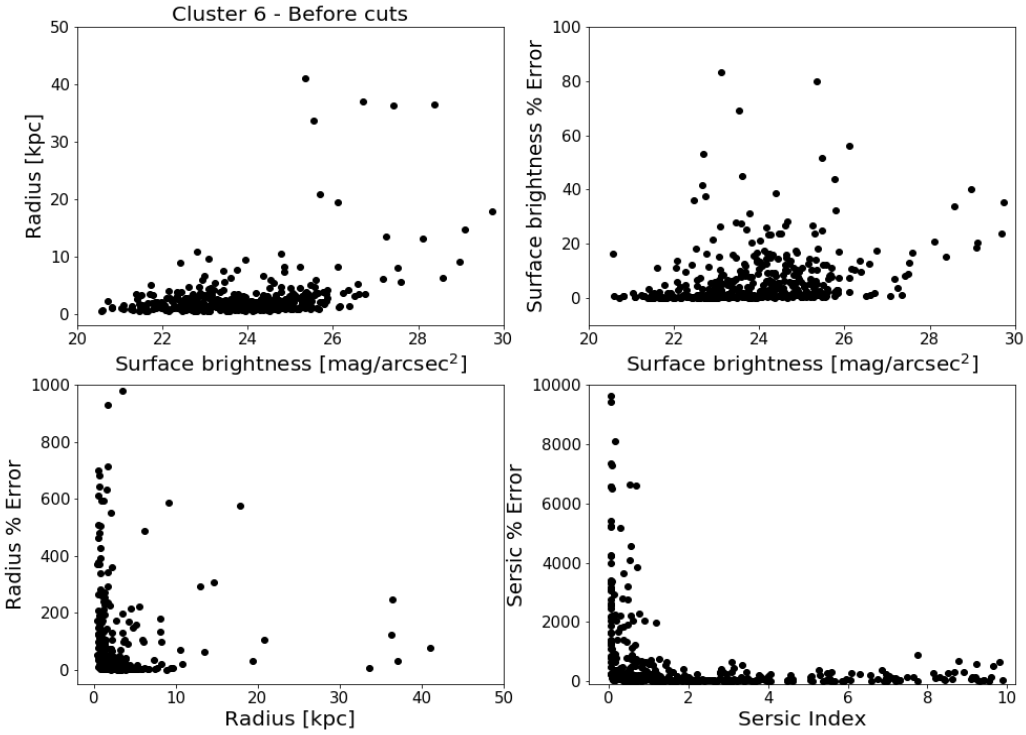

Figure 5.27: Four panel plot containing the dense region of all sources in cluster 6 modelled by GALFIT.

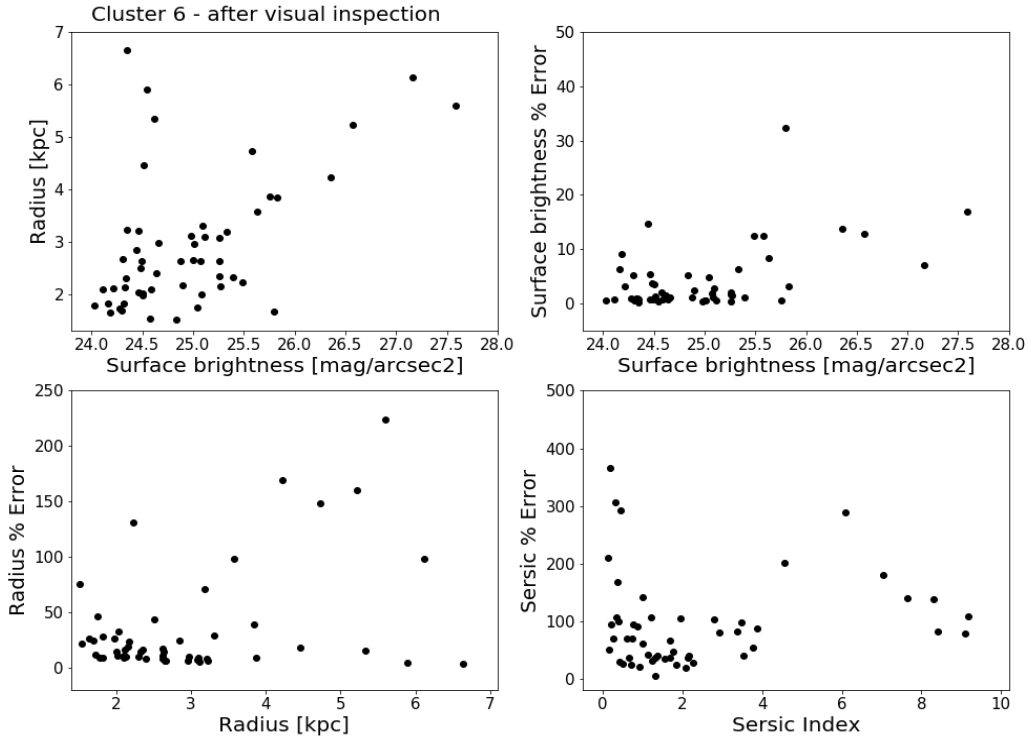

Figure 5.28: Four panel plot of the remaining sources in cluster 6 after applying the Sérsic index, radius, surface brightness cuts and visually inspection.

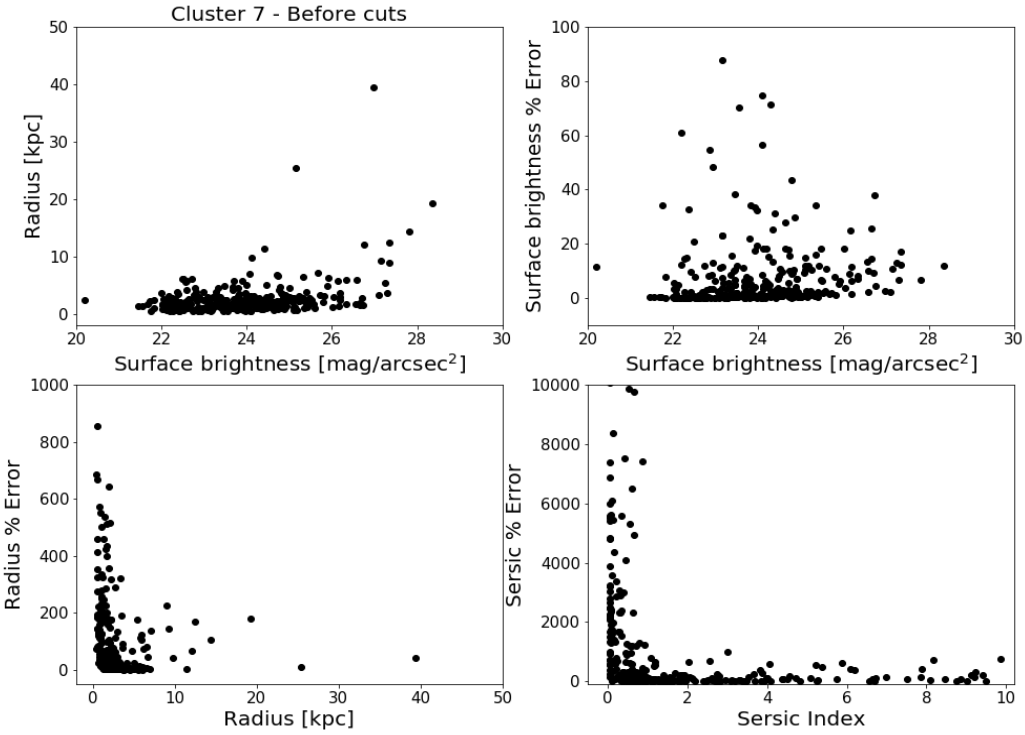

Figure 5.29: Four panel plot containing the dense region of all sources in cluster 7 modelled by GALFIT.

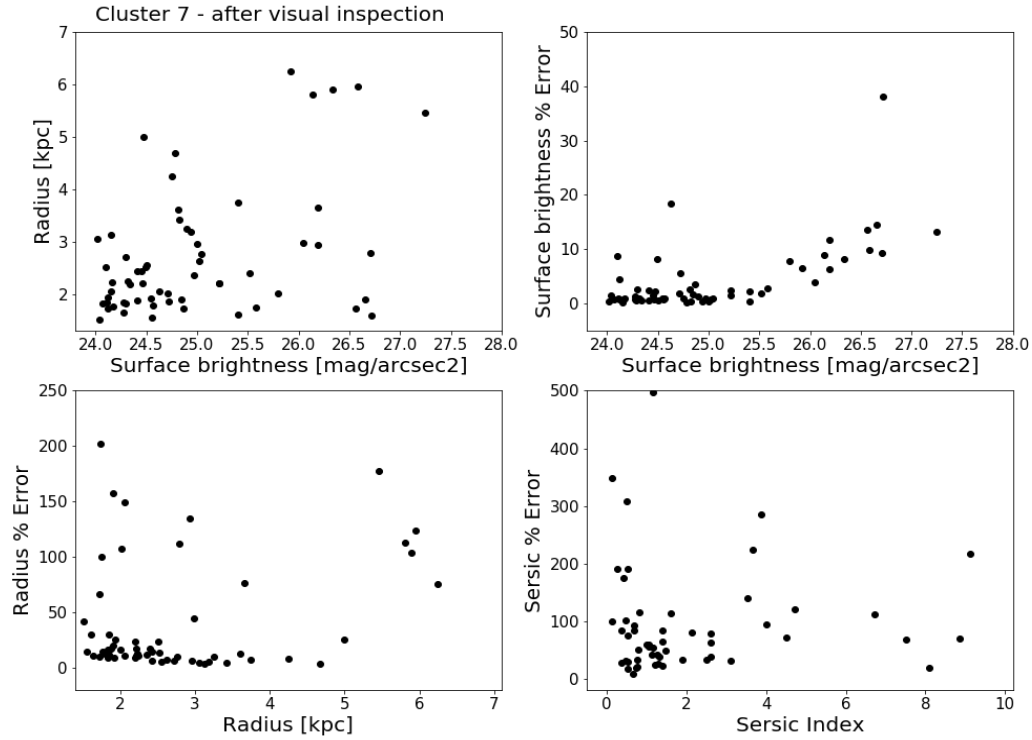

Figure 5.30: Four panel plot of the remaining sources in cluster 7 after applying the Sérsic index, radius, surface brightness cuts and visually inspection.

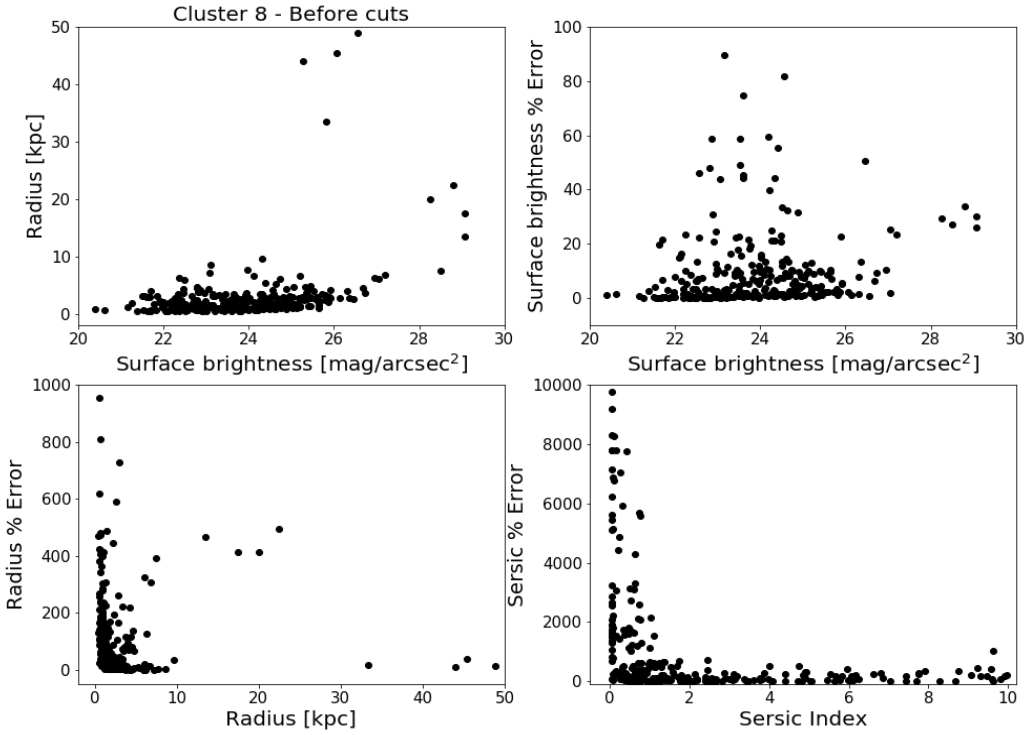

Figure 5.31: Four panel plot containing the dense region of all sources in cluster 8 modelled by GALFIT.

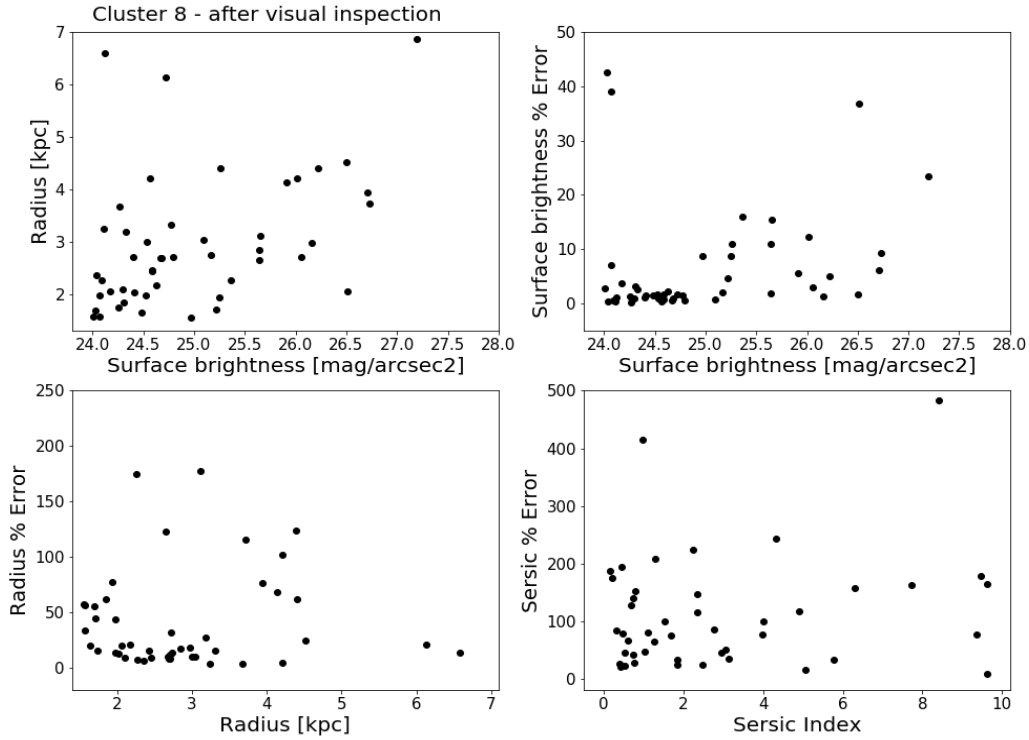

Figure 5.32: Four panel plot of the remaining sources in cluster 8 after applying the Sérsic index, radius, surface brightness cuts and visually inspection.

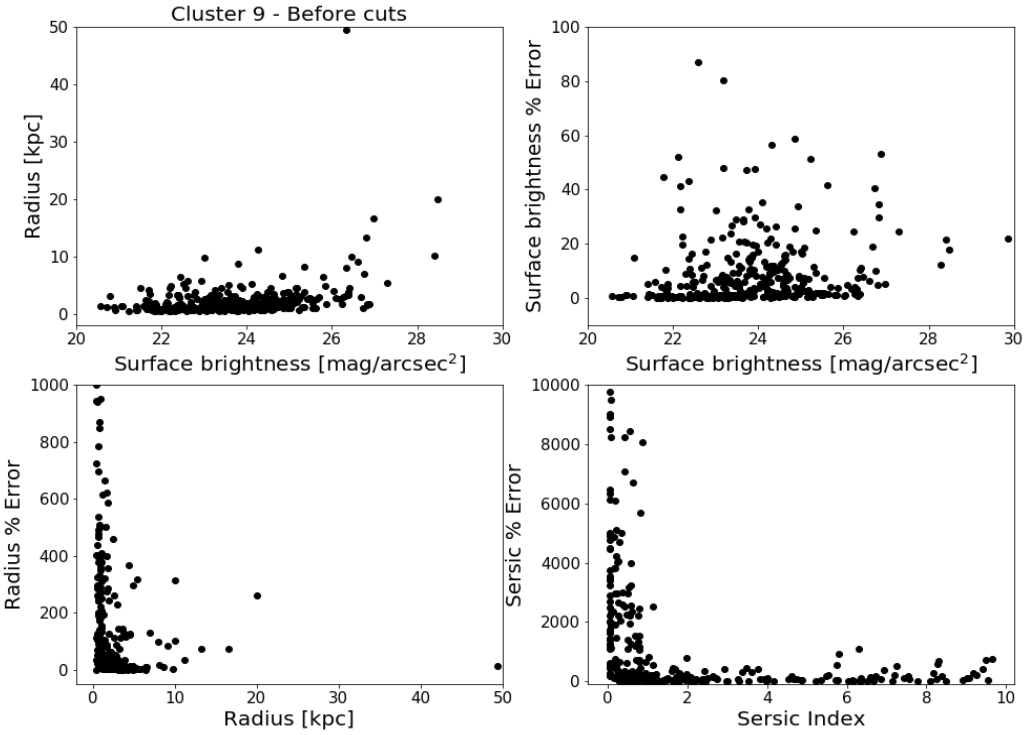

Figure 5.33: Four panel plot containing the dense region of all sources in cluster 9 modelled by GALFIT.

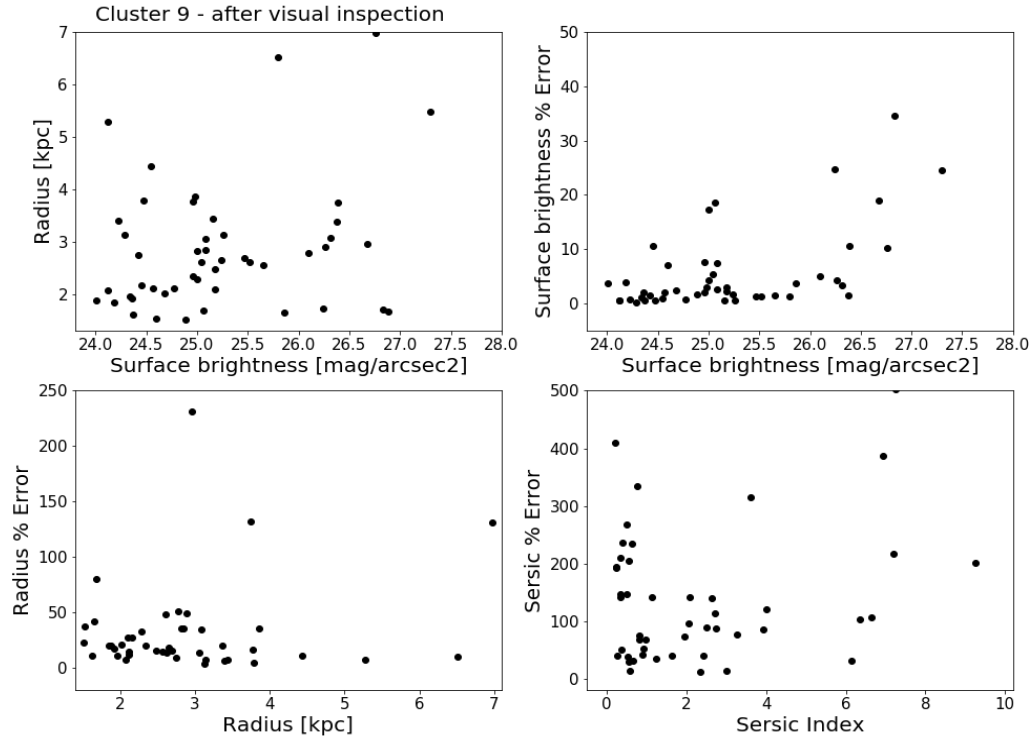

Figure 5.34: Four panel plot of the remaining sources in cluster 9 after applying the Sérsic index, radius, surface brightness cuts and visually inspection.

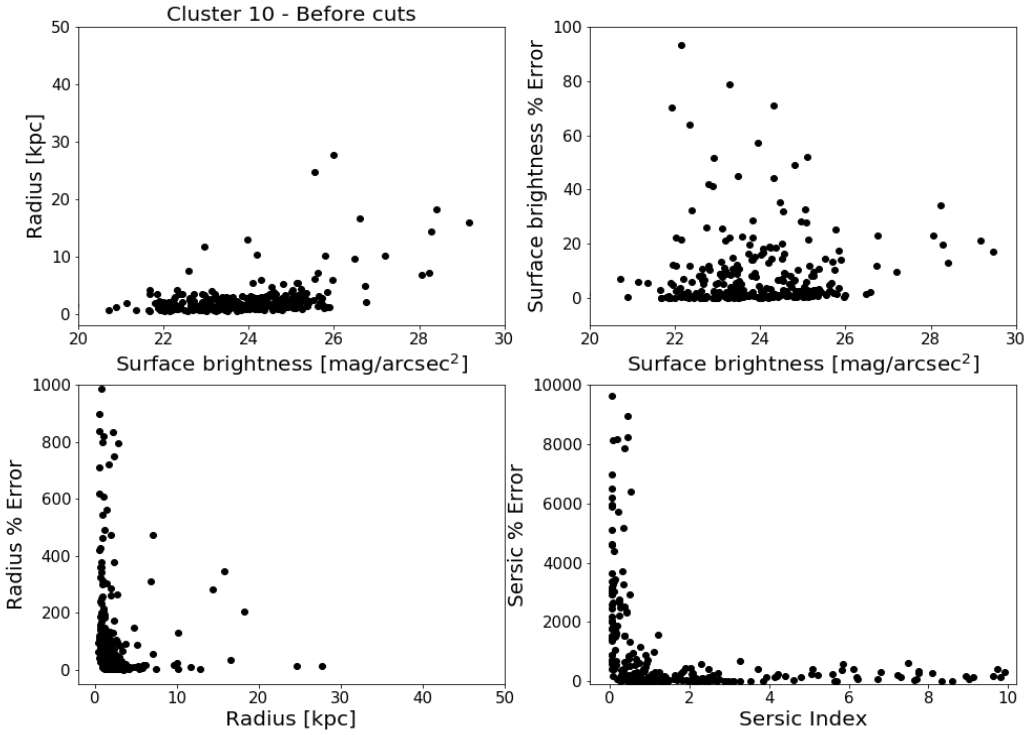

Figure 5.35: Four panel plot containing the dense region of all sources in cluster 10 modelled by GALFIT.

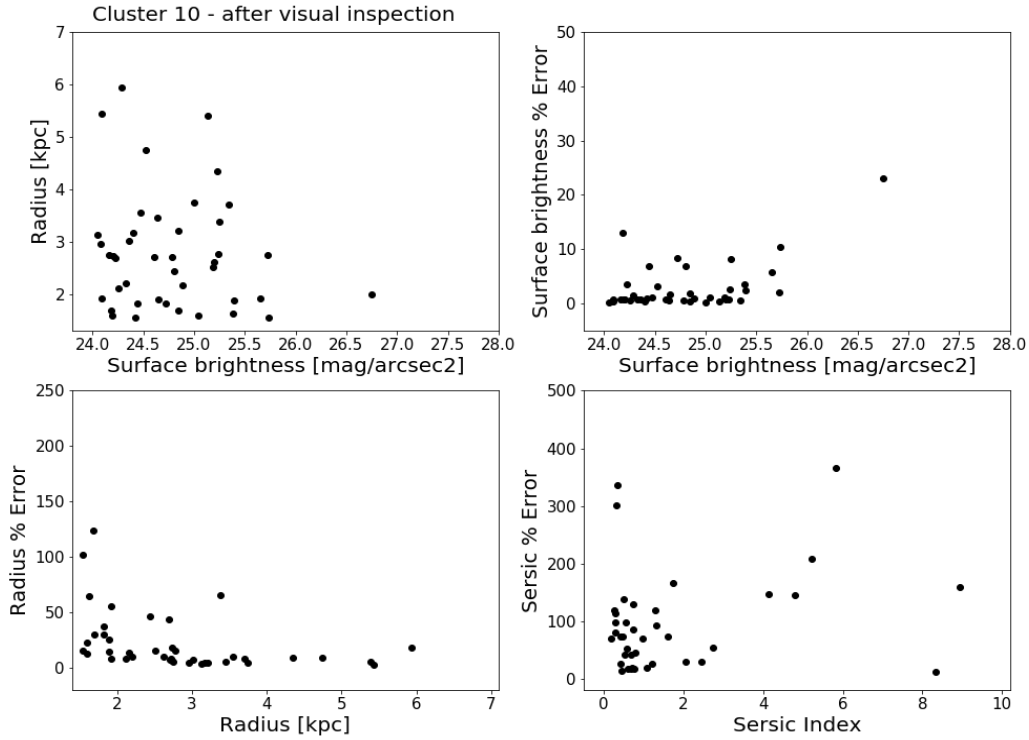

Figure 5.36: Four panel plot of the remaining sources in cluster 10 after applying the Sérsic index, radius, surface brightness cuts and visually inspection.

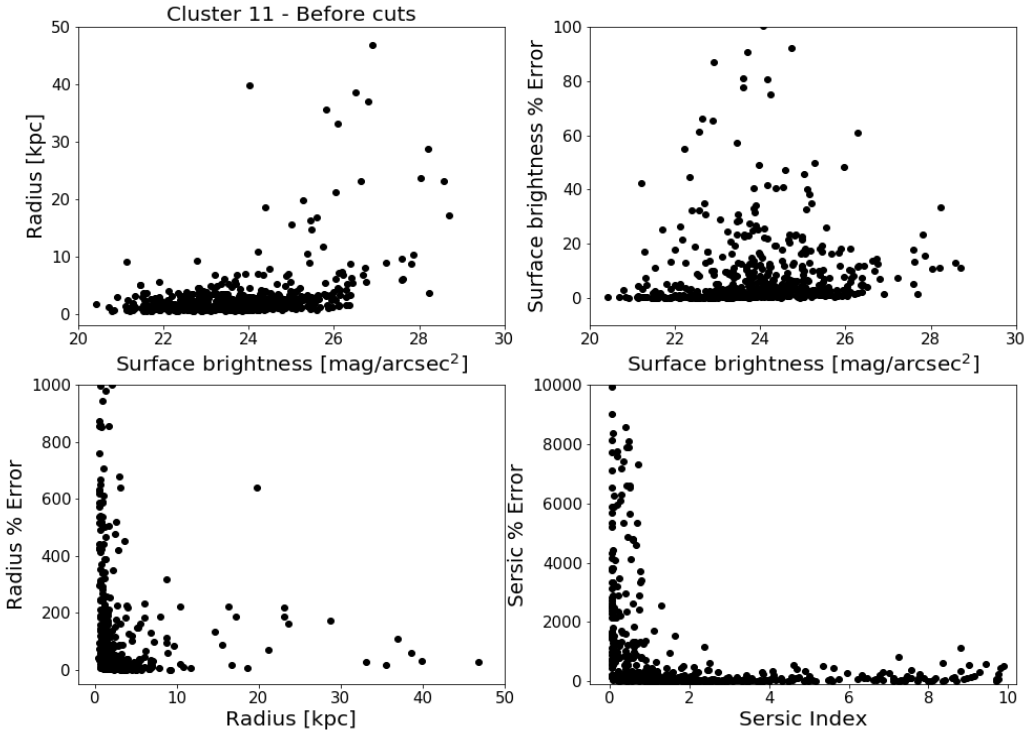

Figure 5.37: Four panel plot containing the dense region of all sources in cluster 11 modelled by GALFIT.

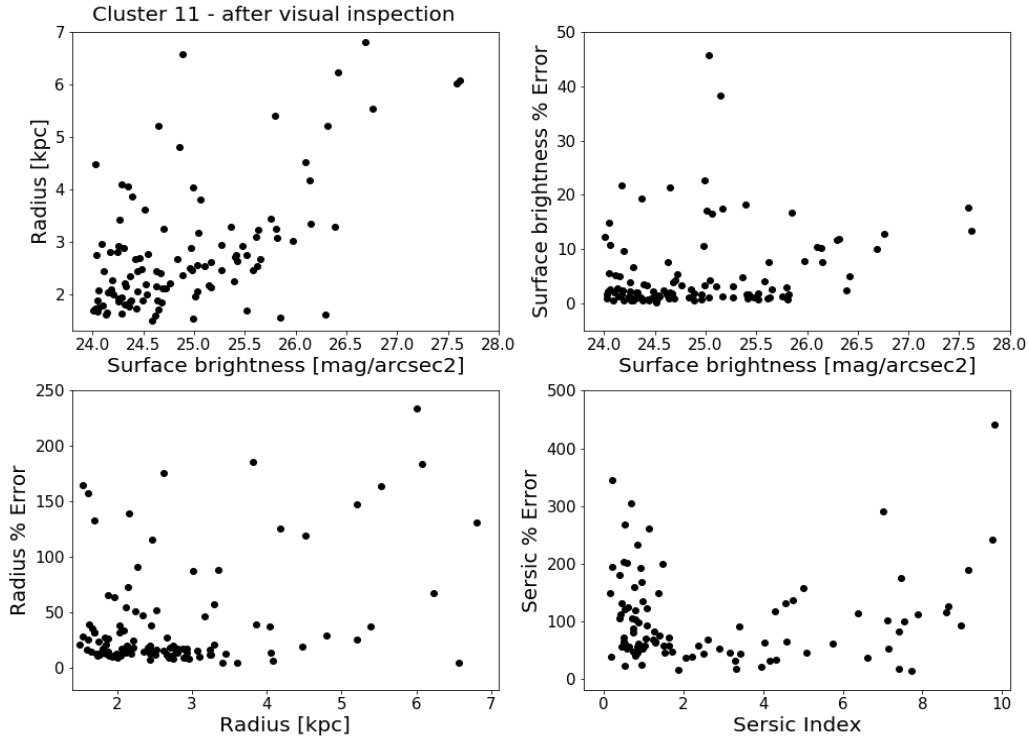

Figure 5.38: Four panel plot of the remaining sources in cluster 11 after applying the Sérsic index, radius, surface brightness cuts and visually inspection.

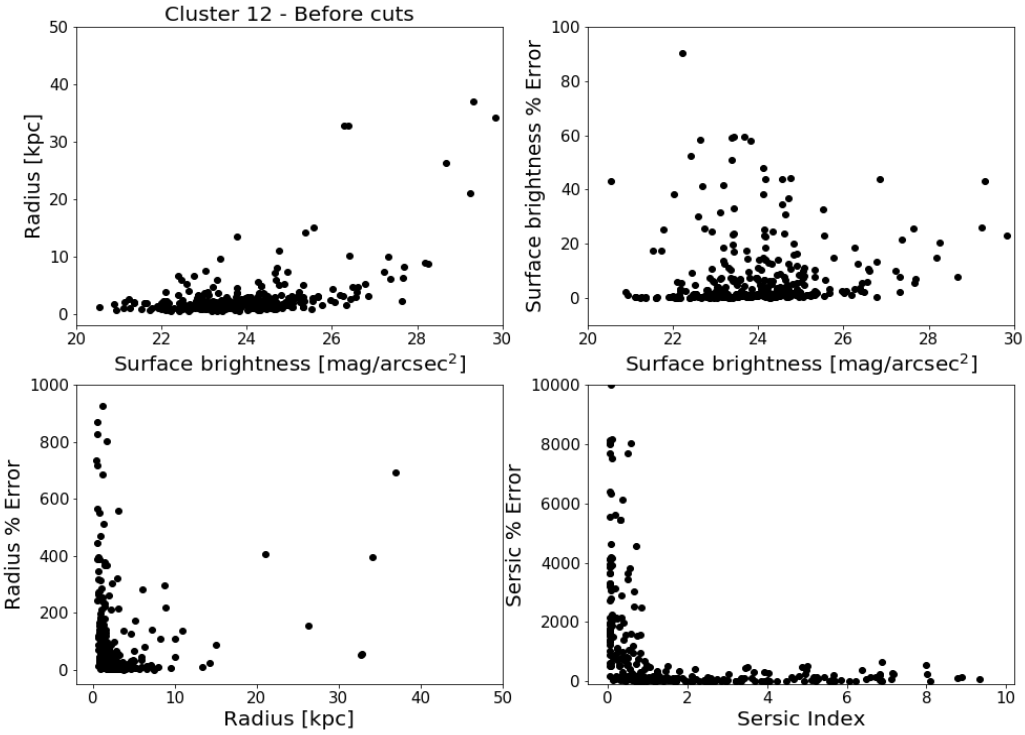

Figure 5.39: Four panel plot containing the dense region of all sources in cluster 12 modelled by GALFIT.

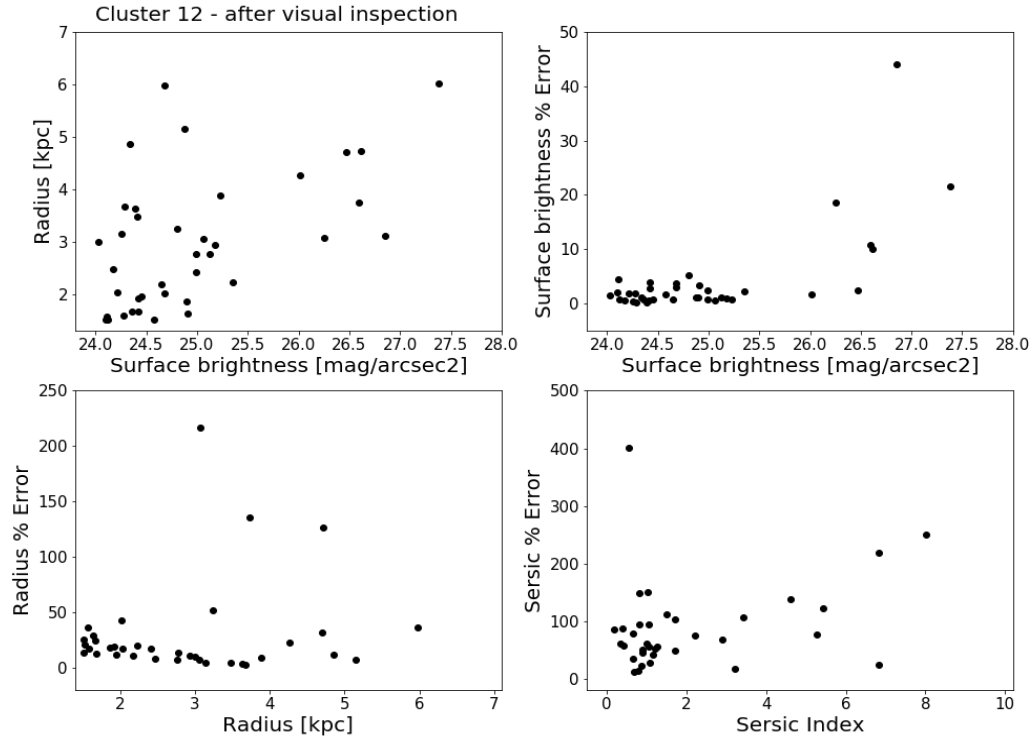

Figure 5.40: Four panel plot of the remaining sources in cluster 12 after applying the Sérsic index, radius, surface brightness cuts and visually inspection.

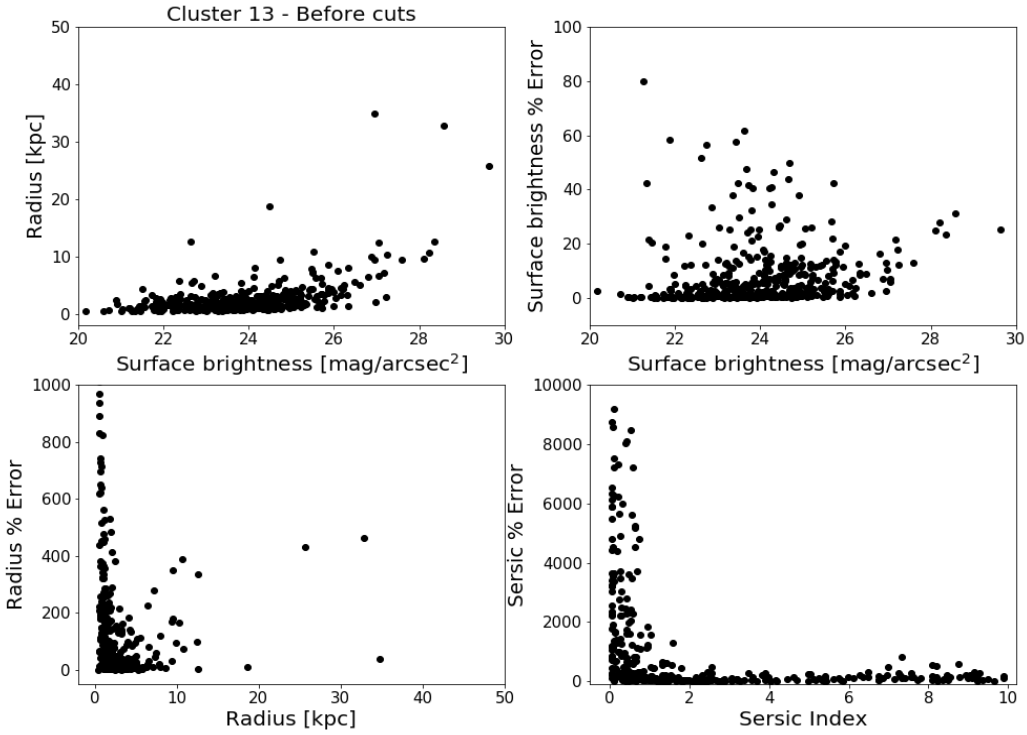

Figure 5.41: Four panel plot containing the dense region of all sources in cluster 13 modelled by GALFIT.

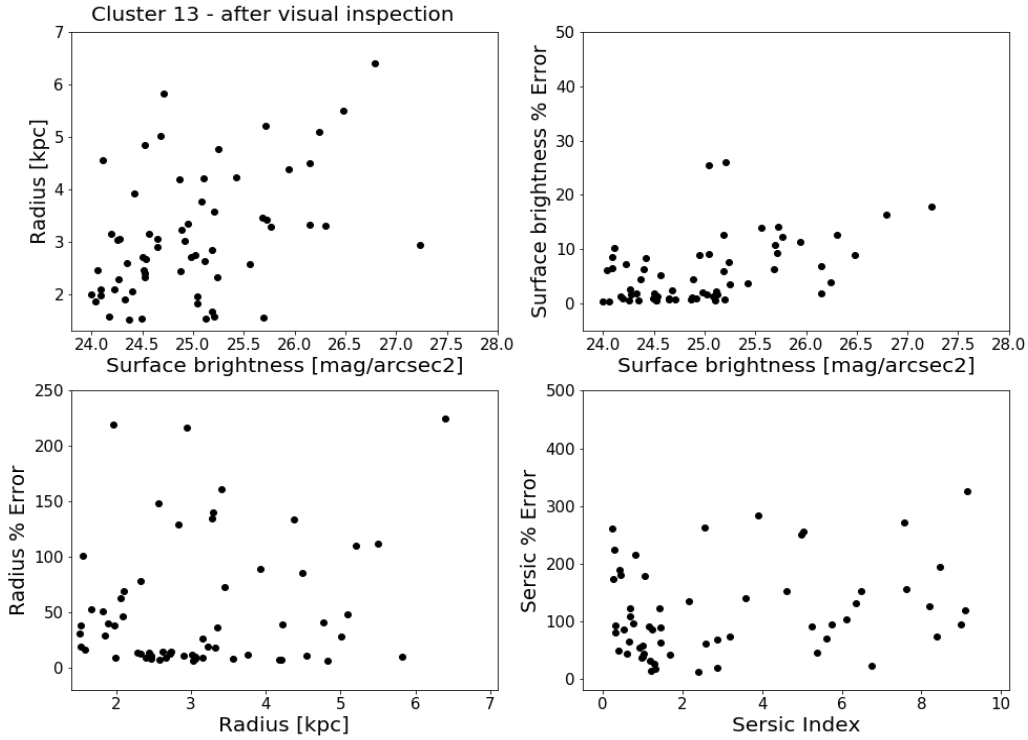

Figure 5.42: Four panel plot of the remaining sources in cluster 13 after applying the Sérsic index, radius, surface brightness cuts and visually inspection.

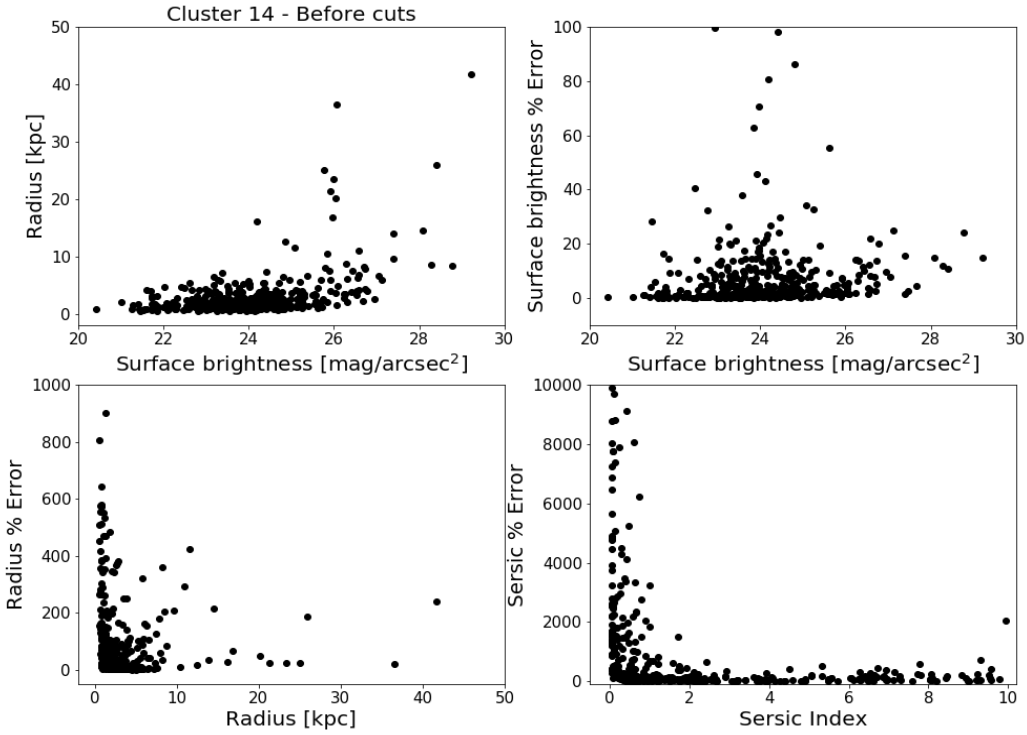

Figure 5.43: Four panel plot containing the dense region of all sources in cluster 14 modelled by GALFIT.

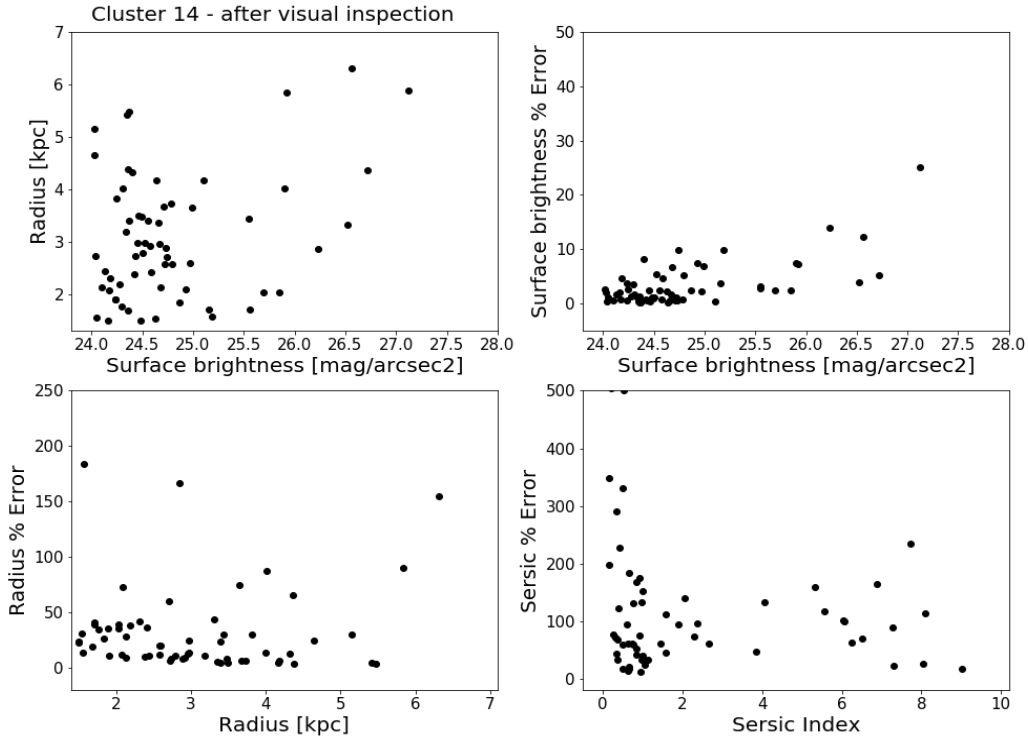

Figure 5.44: Four panel plot of the remaining sources in cluster 14 after applying the Sérsic index, radius, surface brightness cuts and visually inspection.

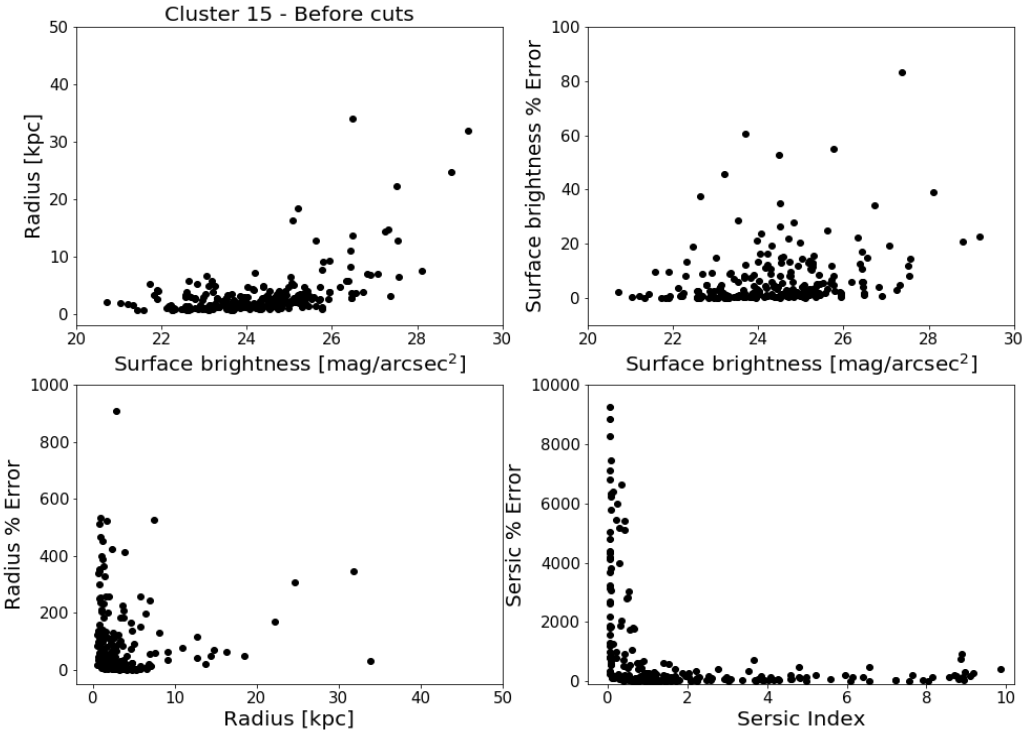

Figure 5.45: Four panel plot containing the dense region of all sources in cluster 15 modelled by GALFIT.

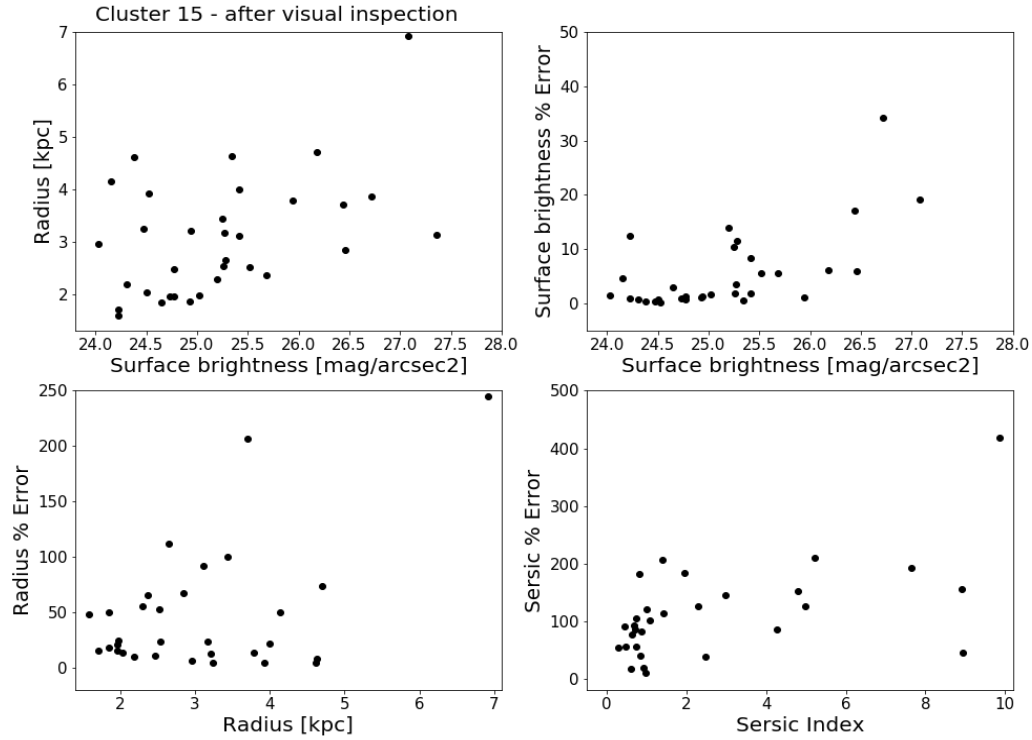

Figure 5.46: Four panel plot of the remaining sources in cluster 15 after applying the Sérsic index, radius, surface brightness cuts and visually inspection.

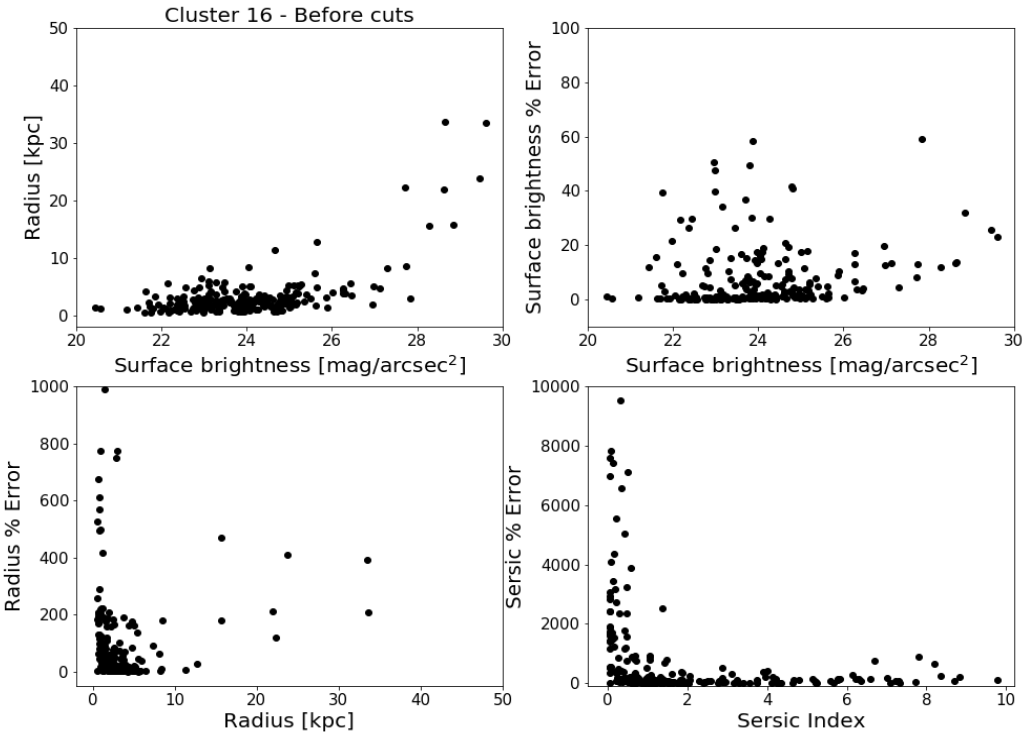

Figure 5.47: Four panel plot containing the dense region of all sources in cluster 16 modelled by GALFIT.

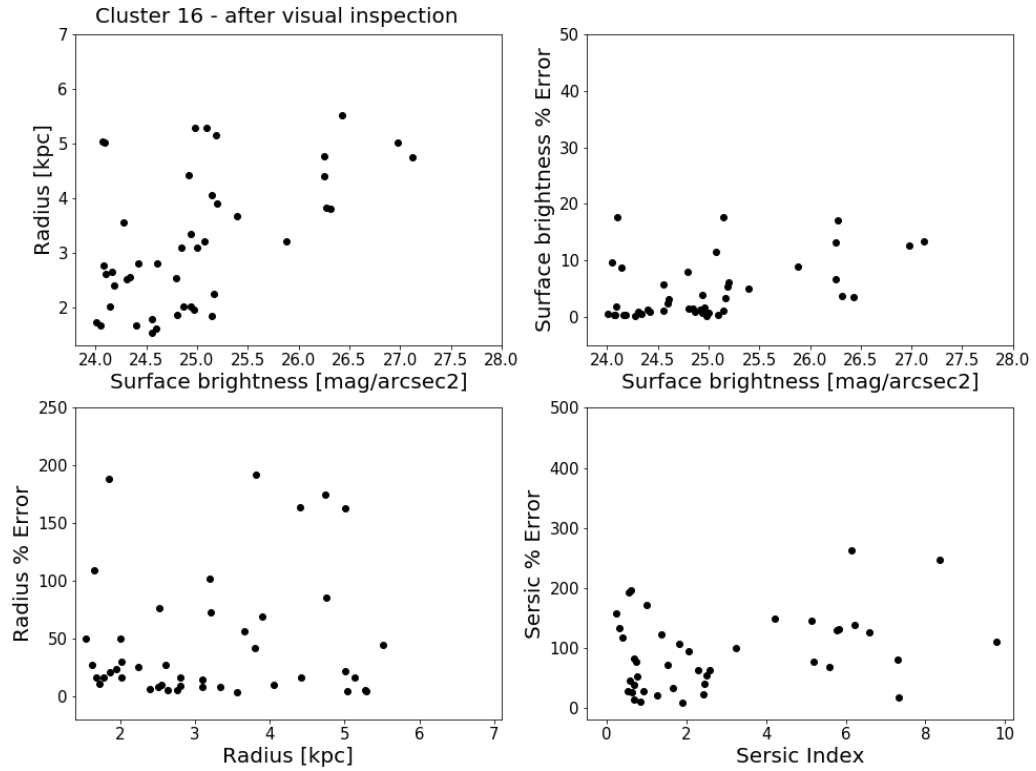

Figure 5.48: Four panel plot of the remaining sources in cluster 16 after applying the Sérsic index, radius, surface brightness cuts and visually inspection.

5.3 Coverage Correction Calculation

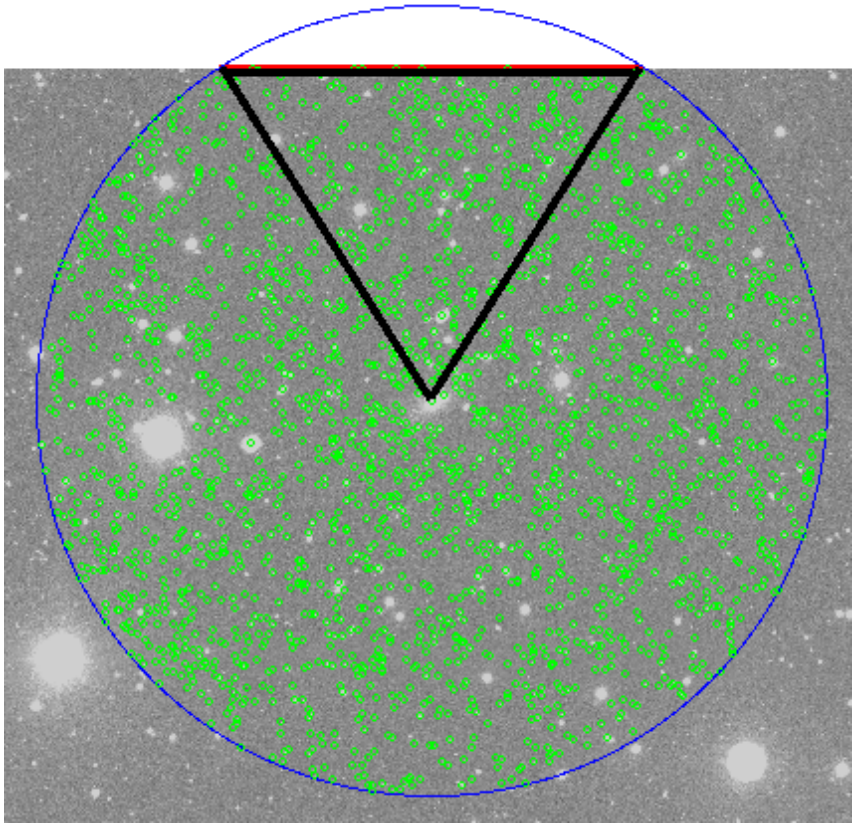

Figure 5.49: SDSS image of cluster 13. The blue circle shows the r_{200m} radius of the cluster. The green circles identify all the catalogued IAC sources in the r_{200m} radius of the cluster. The red line shows the limit of the IAC Legacy project data. The black triangle demonstrates the method used to determine the size of the missing area (equation 11).

To determine the areas of the missing segments from a cluster sector, e.g. cluster 13 as in Figure 5.49, we perform the follow steps:

1. Measure the length of the red line(l_1), distance from two points on the circumference of the missing area.

2. The angle(θ) of the segment can be calculated:

$$\theta = Sin^{-1}(\frac{l_1}{2r}) \qquad , \tag{5.1}$$

where r is the radius of the cluster.

3. The area of a segment of a circle is then:

$$\text{Area} = \frac{2}{360} \times \theta \times \text{Total Cluster Area.} \tag{5.2}$$

4. The area of the segment (point 3) is then subtracted from the area of an isosceles triangle (depicted by the black triangle in Figure 5.49) to get the final area:

$$\text{Final Area} = \text{Area} - \frac{l_1}{2}\left[r^2 - (\frac{l_1}{2}^2)\right]^{-\frac{1}{2}}. \tag{5.3}$$

5.4 Two Dimensional Binned Distributions of Radius and Surface Brightness.

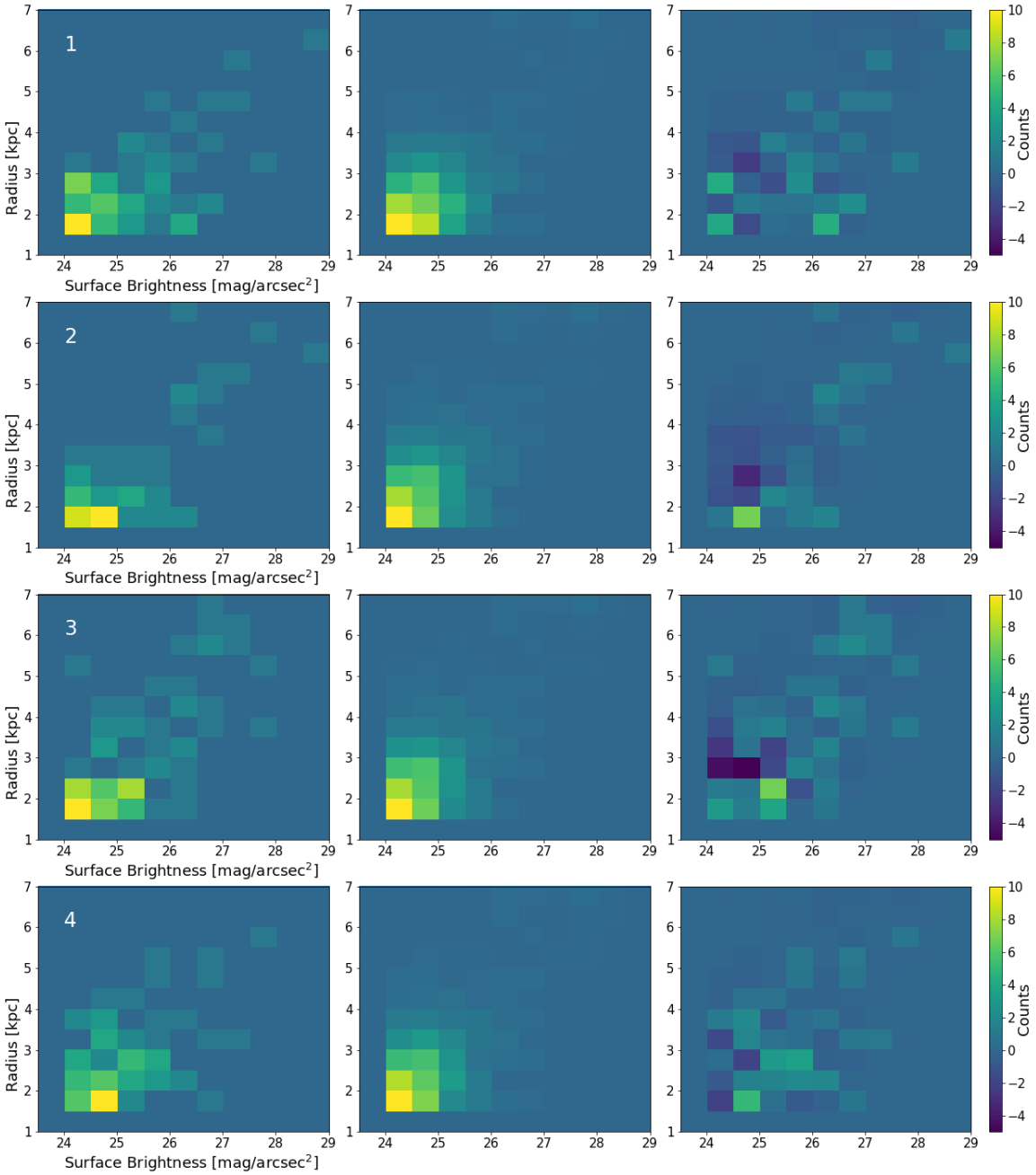

Figure 5.50: Two dimensional binned distributions of radius and surface brightness in clusters 1-4. The left panel shows the UDG candidates found with our UDG detection method in the cluster area. The middle panel displays the average number of UDG-like objects in the background images scaled to the area of the cluster. The right panel displays the difference between the UDG candidates in the cluster and background. The background is subtracted from the UDG candidates. In a few bins there are more galaxies in the background, resulting in negative values.

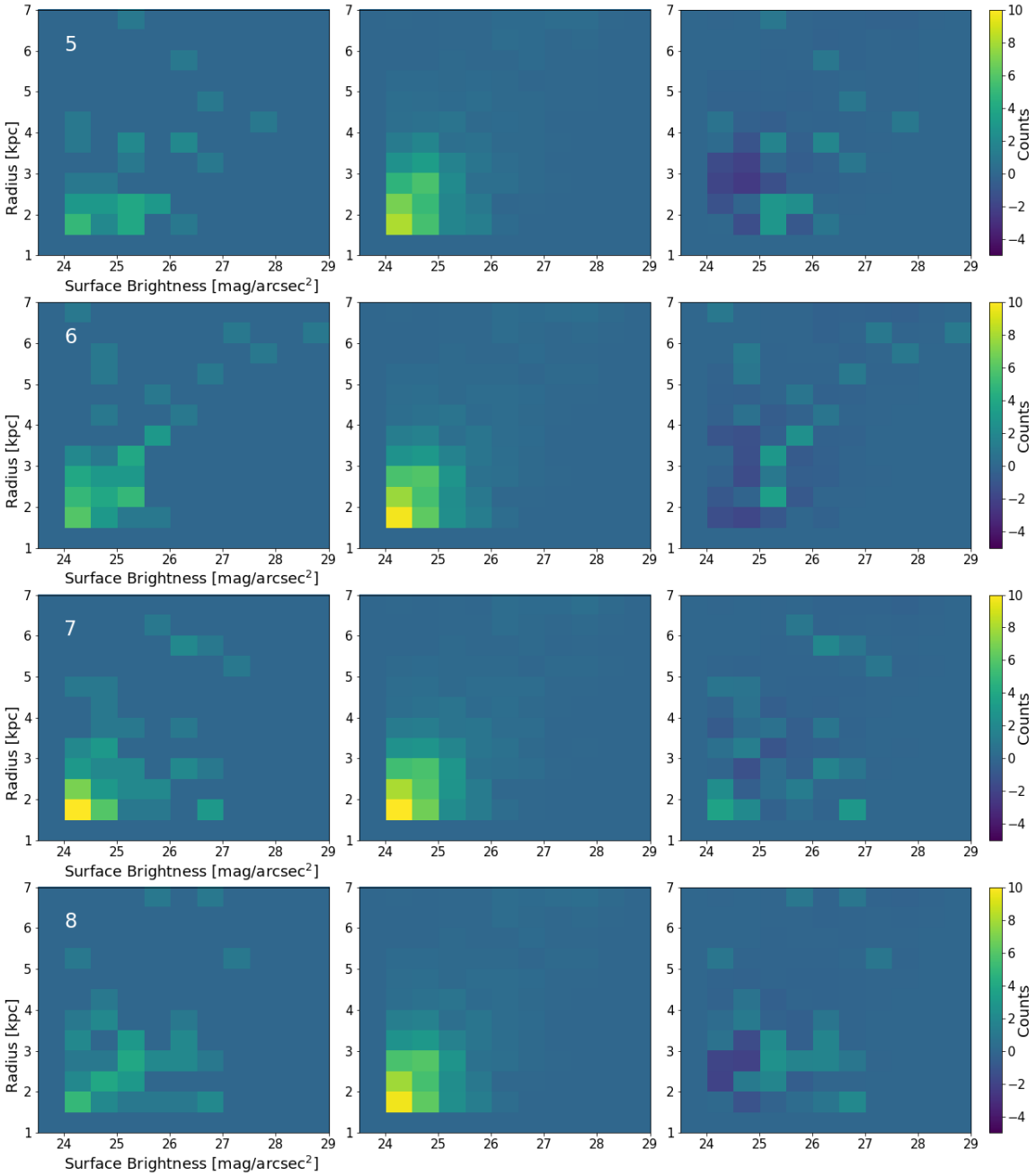

Figure 5.51: (Continued) Two dimensional binned distributions of radius and surface brightness in clusters 5-8.

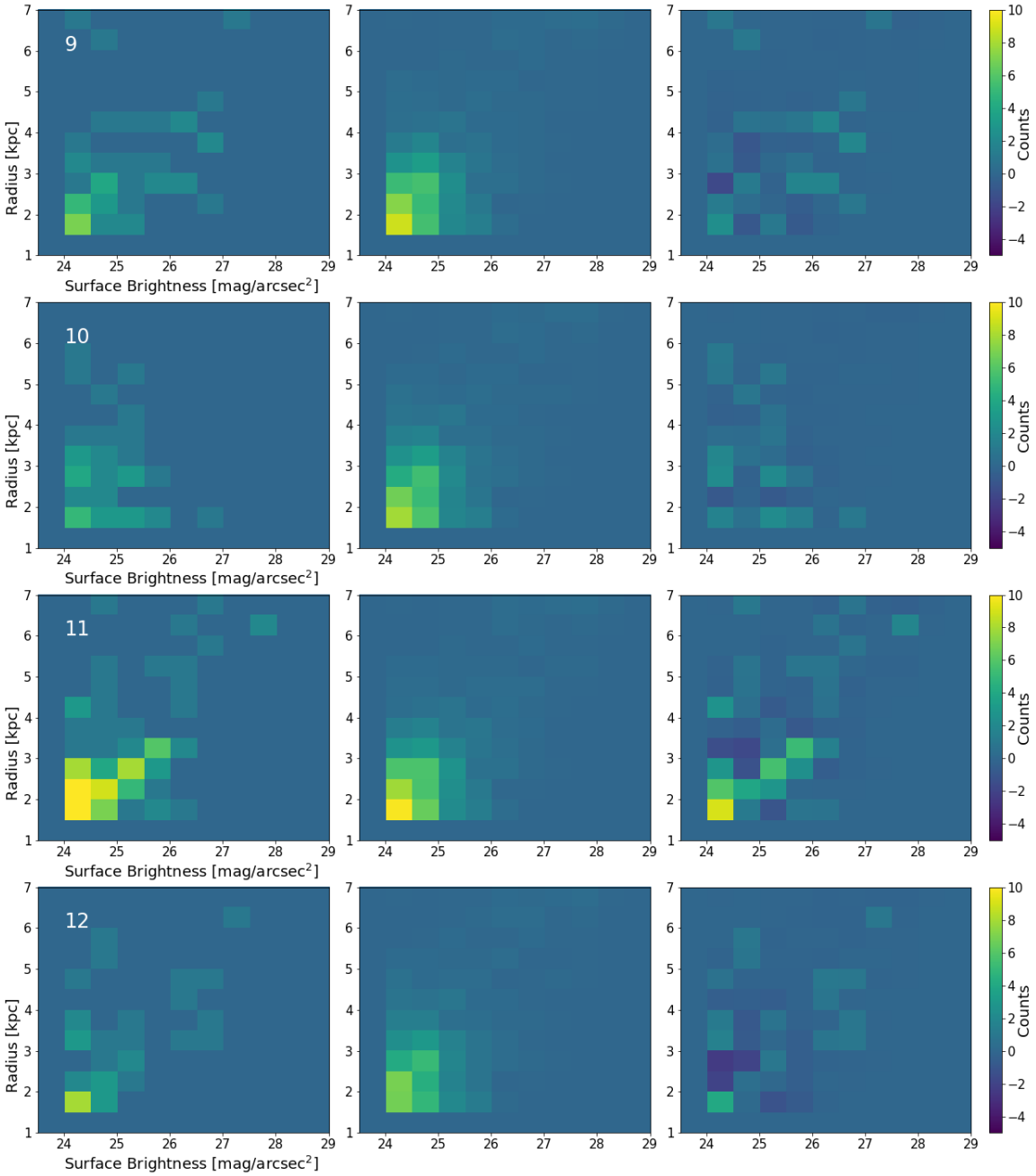

Figure 5.52: (Continued) Two dimensional binned distributions of radius and surface brightness in clusters 9-12.

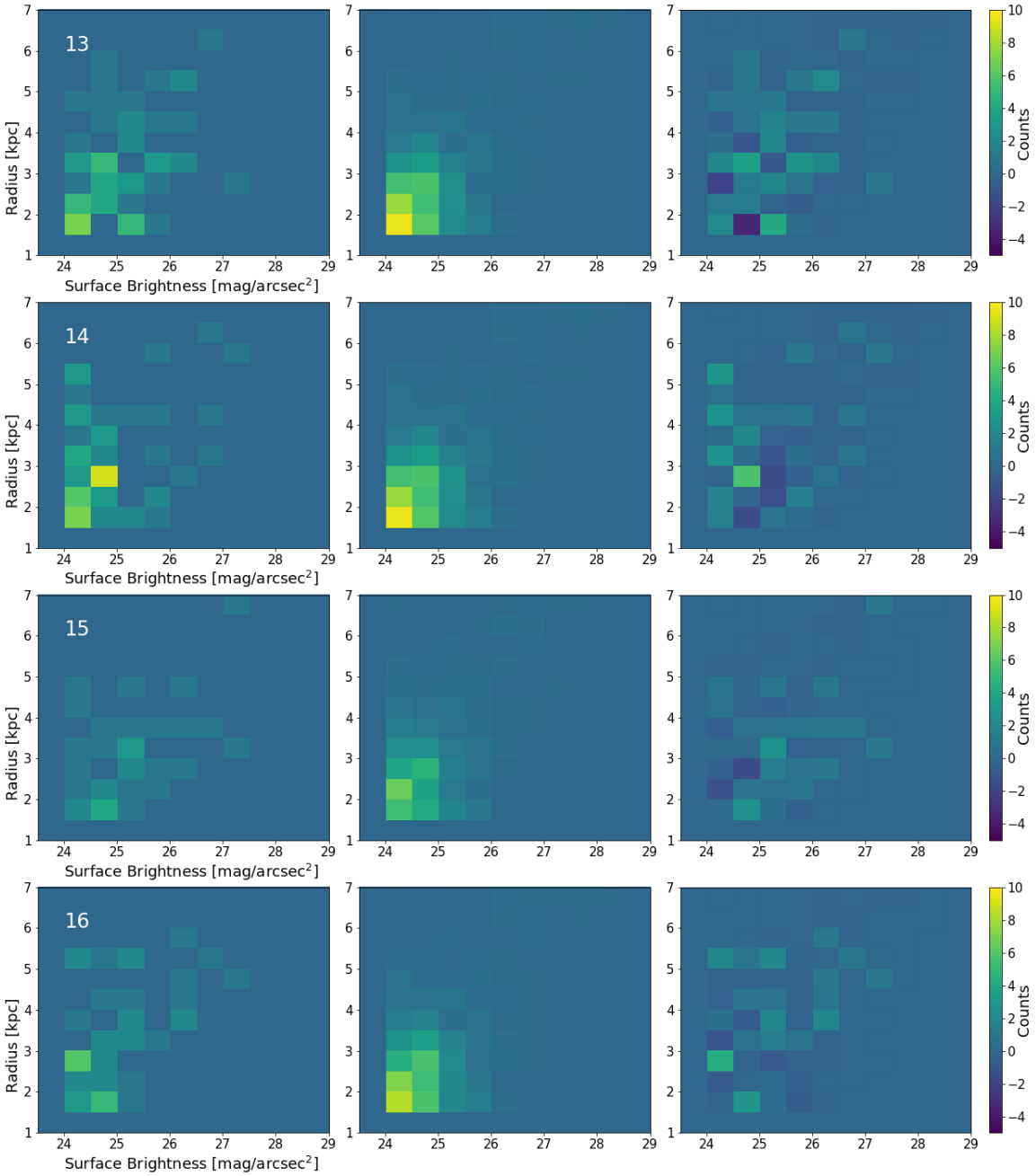

Figure 5.53: (Continued) Two dimensional binned distributions of radius and surface brightness in clusters 13-16.